Universidade de São Paulo
Instituto de Física

# Métodos estatísticos e numéricos para cosmologia de precisão

Francisco Germano Maion

Orientador(a): Prof. Dr. Luis Raul Weber Abramo

Dissertação de mestrado apresentada ao Instituto de Física da Universidade de São Paulo, como requisito parcial para a obtenção do título de Mestre em Ciências.

Banca Examinadora:
Prof. Dr. Luis Raul Weber Abramo (USP)
Prof. Dr. Rogério Rosenfeld (Unesp)
Prof. Dr. Carlos Hernandez-Monteagudo (IAC - Espanha)

São Paulo
2021

**FICHA CATALOGRÁFICA**
**Preparada pelo Serviço de Biblioteca e Informação**
**do Instituto de Física da Universidade de São Paulo**

Maion, Francisco Germano

Métodos estatísticos e numéricos para cosmologia de precisão. São Paulo, 2021.

Dissertação (Mestrado) – Universidade de São Paulo. Instituto de Física. Depto. de Física Matemática

Orientador: Prof. Dr. Luís Raul Weber Abramo
Área de Concentração: Física

Unitermos: 1. Cosmologia; 2. Estrutura do universo; 3. Física; 4. Galáxias

USP/IF/SBI-056/2021

University of São Paulo
Physics Institute

# Statistical and Numerical Methods for Precision Cosmology

Francisco Germano Maion

Supervisor: Prof. Dr. Luis Raul Weber Abramo

Dissertation submitted to the Physics Institute of the University of São Paulo in partial fulfillment of the requirements for the degree of Master of Science.

Examining Committee:
Prof. Dr. Luis Raul Weber Abramo (USP)
Prof. Dr. Rogério Rosenfeld (Unesp)
Prof. Dr. Carlos Hernandez-Monteagudo (IAC - Spain)

São Paulo
2021

# Abstract

The current cosmological model tells us that the Universe began very homogeneous, and matter slowly started clumping to make up stars, galaxies, clusters of galaxies, and the large scale structure that we see. The rate with which these structures were formed is very dependent on the theory that describes gravity. Measuring the multipoles of the power spectrum in redshift space we can probe this growth-rate, and thus constrain alternative models of gravity. In this work we review techniques to accurately measure the multipoles of the power spectrum, and to maximize the amount of information contained in these quantities. We also do a careful treatment of systematical effects, reviewing techniques to forward model these effects into the theoretical model for the power-spectrum multipoles. Combining these techniques, we were able to develop a pipeline capable of taking raw galaxy positions and turning them into unbiased cosmological parameters; furthermore, we have extensively tested it, and applied it to obtain constraints with data from the VIPERS survey. We have also done complementary work on understanding the noise in numerical simulations of the large scale structure. In particular, we have studied techniques to reduce the noise in statistics derived from numerical simulations, and were the first to give a detailed explanation of the process through which the fixing and pairing technique works to reduce the variance in $n$-point functions.

**Keywords:** Redshift-Space Distortions, Large-Scale Structure, Power Spectrum Multipoles, Statistical Cosmology, Perturbation Theory, Bias Expansion, Cosmological Simulations

# Resumo

O modelo cosmológico atual diz que o universo teria começado numa distribuição extremamente homogênea de matéria, que lentamente iria se aglomerando e formando as estrelas, galáxias, aglomerados de galáxias, e a estrutura em larga escala que vemos. A taxa com a qual estas estruturas crescem está intimamente ligada à teoria que rege a gravidade. Através de medições dos multipolos do espectro de potências, é possível medir esta taxa de crescimento, e com isso excluir possíveis modelos de gravitação. Neste trabalho, revisamos técnicas para medir o espectro de potências de forma acurada, e para maximizar a informação contida nestas medições. Ademais, damos um tratamento cuidadoso aos erros sistemáticos, revisando técnicas pelas quais podemos incorporar os efeitos destes erros no modelo teórico do espectro de potências, de forma a reproduzir as observações reais. Combinando estes conhecimentos, foi possível desenvolver um programa computacional capaz de tomar medições das posições de galáxias no céu, e transformá-las em vínculos nos parâmetros cosmológicos; ademais, este programa foi extensivamente testado, e utilizado para vincular parâmetros usando dados reais do levantamento de galáxias VIPERS. Além disso, este trabalho também versa sobre uma área altamente complementar, na qual buscamos compreender o ruído presente em simulações cosmológicas da estrutura em larga escala. Em particular, estudamos técnicas pelas quais é possível reduzir este ruído, e fomos os primeiros a dar uma descrição detalhada do processo pelo qual a técnica *fixing and pairing* reduz a variância em funções de $n$-pontos.

**Palavras Chave:** Distorções do Espaço de Redshifts, Estrutura em Larga Escala, Multipolos do Espectro de Potências, Cosmologia Estatística, Teoria de Perturbações, Expansão de Bias, Simulações Cosmológicas

# Agradecimentos

Gostaria de começar agradecendo meus pais e meu irmão pelo ambiente familiar tranquilo e saudável em que pude crescer, por todas as oportunidades que recebi, e também por todo o fundamental apoio que me deram desde que decidi me aventurar pela carreira em física. Agradeço também aos meus amigos com quem convivi em São Carlos, especialmente a Marina e Guto, pelas inúmeras conversas regadas a cerveja e chorinho (quase sempre o estilo musical). Aos amigos que fiz em São Paulo também tenho muito a agradecer, especialmente Luighi, Canela, Massoni, Rodrigo, Breno, e muitos outros.

Agradeço também àqueles que me ensinaram muito a respeito de cosmologia, especialmente a Raul Abramo, Marcos Lima e Raúl Angulo, e também aos meus colegas Renan Boschetti, Rodrigo Voivodic, Caroline Guandalin, Thiago Mergulhão e Beatriz Tucci pelas discussões sobre ciência e pelos momentos de descontração. Um especial agradecimento fica para Michael J. Wilson e Stefano Rota que decisivamente me ajudaram a completar este trabalho.

Finalmente, agradeço à minha namorada, Natalie, pelo apoio, compreensão e carinho que me dedica, e que foram fundamentais para que eu chegasse até aqui.

Agradeço à FAPESP pelo financiamento durante a realização deste trabalho, através do processo de número 2019/01631-0. As opiniões, hipóteses e conclusões ou recomendações expressas neste material são de responsabilidade do(s) autor(es) e não necessariamente refletem a visão da FAPESP. O presente trabalho foi realizado com apoio do CNPq, Conselho Nacional de Desenvolvimento Científico e Tecnológico - Brasil.

*"Este pensador observó que todos los libros, por diversos que sean, constan de elementos iguales: el espacio, el punto, la coma, las veintidós letras del alfabeto. También alegó un hecho que todos los viajeros han confirmado: No hay en la vasta Biblioteca, dos libros idénticos. De esas premisas incontrovertibles dedujo que la Biblioteca es total y que sus anaqueles registran todas las posibles combinaciones de los veintitantos símbolos ortográficos (número, aunque vastísimo, no infinito) o sea todo lo que es dable expresar: en todos los idiomas."*

---

Jorge Luis Borges

La Biblioteca de Babel

# Contents


**1 Introduction** **1**

**2 Measuring the Growth of Structures** **5**

2.1 Redshift-Space Distortions . . . . . 7

2.2 Modelling RSDs . . . . . 13

2.3 Alcock-Paczyński Effect . . . . . 15

**3 Power Spectrum Estimation** **18**

3.1 Interpolating onto Regular Grid . . . . . 19

3.2 FFT-based Estimation . . . . . 22

3.2.1 Interlacing . . . . . 25

3.2.2 Shot-Noise . . . . . 27

3.3 Estimating Power-Spectrum Multipoles . . . . . 28

3.4 Power-Spectrum Estimators . . . . . 32

3.4.1 Cramér-Rao Lower Bound . . . . . 34

3.4.2 Quadratic Estimators . . . . . 34

3.4.3 FKP . . . . . 38

3.4.4 MTOE . . . . . 42

3.5 Numerical Implementation . . . . . 42

3.5.1 FKP . . . . . 42

3.5.2 Resolution Effects . . . . . 45

3.5.3 Binning effects . . . . . 45

**4 Systematic Effects** **47**

4.1 Window Function . . . . . 47
4.1.1 Pair Counting Approach . . . . . 52
4.2 Incompleteness Effects . . . . . 53
4.3 Integral Constraint . . . . . 57

**5 VIPERS Analysis** **59**
5.1 The VIPERS Survey . . . . . 59
5.2 Pipeline Overview . . . . . 60
5.3 Galaxy Mocks . . . . . 64
5.4 Testing Pipeline for Biases . . . . . 64
5.5 Priors . . . . . 67
5.6 Analysis of the Data . . . . . 68

**6 Fixed and Paired Simulations** **73**
6.1 Fixed and Paired Fields . . . . . 76
6.2 Simulations . . . . . 77
6.3 Bias and Variance Reduction . . . . . 79
6.4 Theoretical Predictions . . . . . 83
6.5 $P_{11}, P_{1\delta}, P_{\delta\delta}$ . . . . . 85
6.6 $P_{1\delta^2}, P_{1s^2}, P_{\delta\delta^2}, P_{\delta s^2}$ . . . . . 87
6.7 $P_{\delta^2\delta^2}, P_{s^2s^2}$ . . . . . 87
6.8 $P_{1\nabla^2\delta}, P_{\delta\nabla^2\delta}, P_{\delta^2\nabla^2\delta}, P_{s^2\nabla^2\delta}, P_{\nabla^2\delta\nabla^2\delta}$ . . . . . 88
6.9 Testing Predictions . . . . . 89

**7 Conclusions and Final Remarks** **92**

**Bibliography** **100**

**APPENDICES** **100**

**A Additional Results of VIPERS Analysis** **101**
A.1 $z_2$ . . . . . 101
A.2 $z_3$ . . . . . 103

**B Lagrangian Perturbation Theory** **105**

B.1 Linear Solution . . . . . 107

B.2 Recurrence Relations . . . . . 108

**C Advected Basis Fields and Spectra** **109**

C.1 Advected Basis Fields . . . . . 109

C.1.1 $\delta_1$ . . . . . 109

C.1.2 $\delta_\delta$ . . . . . 111

C.1.3 $\delta_{\delta^2}$ . . . . . 112

C.1.4 $\delta_{s^2}$ . . . . . 113

C.1.5 $\delta_{\nabla^2\delta}$ . . . . . 114

**D Detailed Variance Calculations** **116**

D.1 $P_{11}$ . . . . . 116

D.2 $P_{1\delta^2}$ . . . . . 120

D.3 $P_{\delta^2\delta^2}$ . . . . . 123

# Chapter 1

# Introduction

The current standard model of cosmology has been extremely successful up to now, being able to accurately describe probes of the early universe such as the Cosmic Microwave Background (hereafter CMB) (Planck Collaboration, 2018), and also probes of the late universe such as the large scale structure (hereafter LSS) in the distribution of galaxies (Alam et al., 2017). Nevertheless, there is still much improvement to be made. Two of the main ingredients of this model, dark matter and dark energy, are still poorly understood. The presence of dark matter has become firmly established (Rubin and Ford, 1970; Trimble, 1987) , though its composition and fundamental interaction properties are yet unknown. Dark energy too is essential (Riess et al., 1998; Perlmutter et al., 1999), and yet, we are currently unable to explain it from the point of view of particle physics, or distinguish it from modified theories of gravity. Other issues are posed by the recent tensions between measurements of the Hubble constant $H_0$ in early and late universe probes (Riess, 2019), and all of these point to the same message: we need more observations to inform us on the nature of the universe.

Upcoming surveys such as Euclid[1], Dark Energy Spectroscopic Instrument (DESI)[2], Javalambre Physics of the Accelerating Universe Astrophysical Survey (J-PAS)[3], Prime

[1] https://www.euclid-ec.org
[2] https://www.desi.lbl.gov/
[3] http://www.j-pas.org/

Focus Spectrograph survey (PFS)[4], or Legacy Survey of Space and Time (LSST)[5] will provide an unprecedented amount of data on the large scale structure of the universe, mapping galaxies and quasars over large fractions of the sky and up to high redshifts. Analyzing this data will not be an easy job: the mere task of processing it will be challenging, pushing for the development of more efficient analysis algorithms; current theoretical models are not accurate enough for the analysis of this data, especially at the smallest scales (Nishimichi et al., 2020), and finally, it is also very important to improve on statistical methods to extract as much information as possible from the measurements.

One way to extract more information from observations, and increase their constraining power, is to divide the galaxies into different populations which trace the dark-matter density field in distinct ways. In a seminal work, (McDonald and Seljak, 2009) showed how one can employ this method to measure redshift-space distortions (hereafter RSDs) with much better precision than using one single tracer. Improving upon this, (Abramo and Leonard, 2013; Abramo, Secco, and Loureiro, 2015) developed an optimal estimator for the power spectrum in the presence of multiple tracers, the Multi-Tracer Optimal Estimator (MTOE); by optimal we mean that this method is guaranteed to weight the galaxies in such a way that the resulting power spectrum will carry the maximum amount of information possible. Measurements of power spectra from simulations (Abramo, Secco, and Loureiro, 2015), and of covariance matrices from galaxy mocks (Montero-Dorta et al., 2020) have confirmed that the noise level is lower in spectra estimated with MTOE. However, constraints on cosmological parameters have never been obtained with this method, and the present work dedicates itself to building an analysis pipeline with which we could fill this gap by measuring the matter growth-rate from RSDs using public data from the VIPERS survey (Guzzo et al., 2014).

The preceding paragraph focused on attacking the issue of how to improve our statistical tools to extract more information from observations. Another very important question to be approached is that of how to develop theoretical tools which are valid into the non-linear regime. The number of available Fourier modes grows with $k$, and therefore, non-linear scales contain, in principle, a vast amount of information. Predictions of the

[4] https://pfs.ipmu.jp/
[5] https://www.lsst.org/

power spectrum using Standard Perturbation Theory (hereafter SPT) quickly break down as we leave the linear regime, at around $k \approx 0.1h/\text{Mpc}$ (Bernardeau et al., 2002), and even with the great effort of developing an Effective Field Theory of Large Scale Structure, the theoretical predictions still reach only modest scales $k \approx 0.2h/\text{Mpc}$ (Carrasco, Hertzberg, and Senatore, 2012; Nishimichi et al., 2020). Recent works have been taking another route, using different computational methods (e.g.: neural networks, gaussian processes, polynomial chaos expansions) to emulate dark matter statistics from sets of N-Body simulations; this allows one to obtain spectra which are accurate up to $k \approx 1h/\text{Mpc}$ at a negligible computational cost (Heitmann et al., 2013; Kobayashi et al., 2020; Euclid Collaboration et al., 2020; Angulo et al., 2020; Zennaro et al., 2021).

N-Body simulations are unmatched in their accuracy, especially at the small scales. However, since they must be run in finite volumes, they will have some degree of variance, which will be considerable at the largest scales; of course, at the largest scales one can substitute their predictions by those of perturbation theory, since they are close to exact in this regime, but an issue still persists at the transition between linear and non-linear scales. In this regime, N-Body simulations still contain some level of noise, and PT begins to fail (Desjacques, Jeong, and Schmidt, 2018); therefore, one must define some transition scale $k^*$ between these predictions to get the best out of them (Zennaro et al., 2021; Hadzhiyska et al., 2021). This makes it clear that it would be very interesting to have a way to reduce the variance in N-Body simulations, in order to be able to use it down to smaller values of $k$, thus avoiding model error introduced by PT predictions.

One way to do this is by using the fixing and pairing technique, proposed by Angulo and Pontzen, 2016; this has been shown to reduce the variance in the matter power spectrum by many orders of magnitude. There is one important shortcoming in these simulations: there is no theoretical model for their variance; this is a problem because we would like to compare their variance to the model error from PT, and it is not an option to run multiple N-Body simulations to estimate their variances, due to their prohibitive cost. Furthermore, galaxy mocks created from these kinds of simulations will inherit the noise in the subjacent dark matter density field, and it is essential to know the value of this variance, to make proper use of their clustering statistics. A second focus of this work

is precisely to develop a theoretical model for the variance of clustering statistics derived from fixed and paired simulations.

This dissertation will take the following format: in chapter 1 we discuss how one can measure the growth of structures using RSDs; in chapter 2 we discuss techniques to estimate power-spectrum multipoles from cosmological data, including detailed discussions of FFT based estimation, aliasing effects and optimal weighting; in chapter 3 we discuss the systematic effects which one should model to correctly interpret observations, and describe how we modeled them in our measurements; in chapter 4 we show the results of our RSD analysis of the VIPERS survey, showing that the developed pipeline is capable of producing unbiased constraints on $f\sigma_8(z)$; in chapter 5 we discuss the fixing and pairing technique for the reduction of variance in cosmological simulations, and present our findings on the behavior of different dark-matter statistics in this kind of simulation. Most notably, we present for the first time expressions for the variance of statistical quantities obtained from fixed and paired simulations.

# Chapter 2

# Measuring the Growth of Structures

Viewed from great distances, galaxies are but small points of light, and it is hopeless to try and measure their distances using parallax. The expansion of the universe comes to our aid in this: photons emitted from these galaxies will lose energy in their path towards us due to the expansion of the universe, and therefore, their frequencies will be shifted towards smaller values, or in other words, the photons will be redshifted. The amount of energy they lose will depend on the traveled distance, and therefore, if we can measure their redshift, it is possible to infer their distance from us. Galaxies have very distinctive absorption and emission lines due to the presence of certain atoms or molecules in stellar atmospheres or interstellar cold gas (Kennicutt, 1992); by observing galaxies and determining their spectrum precisely, one can then measure the displacement of these spectral lines from their expected frequencies, thus determining the galaxy's redshift, and consequently, its distance. In recent years this technique has been used to obtain the spectra of hundreds of thousands of galaxies, mapping the universe to an unprecedented level of precision (Davis and Peebles, 1983; York et al., 2000; Jones et al., 2004; Newman et al., 2013; Garilli, B. et al., 2014; Liske et al., 2015).

The redshifting of the photons due to the expansion of the universe can also be viewed roughly as a Doppler shift, if one defines a recession velocity for the galaxy $\boldsymbol{v}_r = \boldsymbol{r}H(z)$; $\boldsymbol{v}_r$ can be seen as the velocity at which this galaxy was moving away from the observer at the time it emitted the photon. It is not too hard to see that if this galaxy has

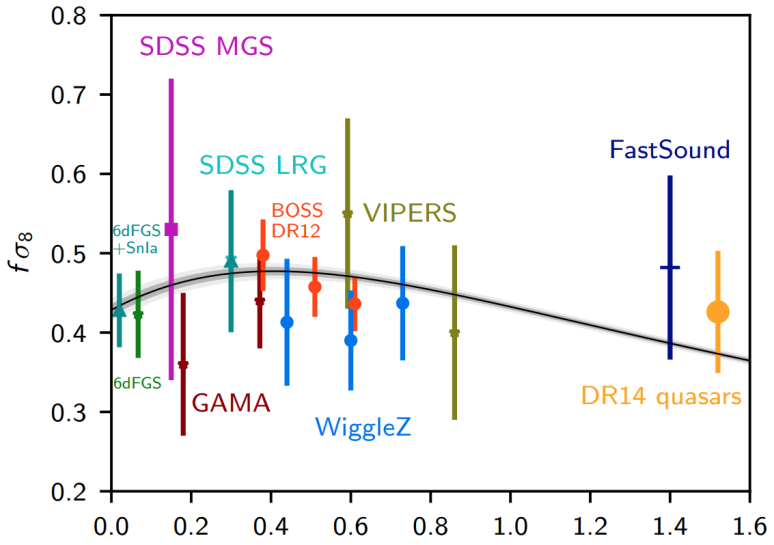


**Figure 2.1:** Collection of constraints on $f\sigma_8$ from RSDs using data obtained from many experiments at different redshifts. The solid black line represents the prediction for General Relativity computed with the cosmology obtained from Planck TT,TE,EE+lowE+lensing data, and gray bands represent 68% and 95% confidence intervals. Extracted from Aghanim et al., 2020

some peculiar velocity $\boldsymbol{u}$ due to the gravitational pull of inhomogeneities, we will naively infer its recession velocity to be $\boldsymbol{v}_r' = \boldsymbol{v}_r + \boldsymbol{u}$, and deduce from it an incorrect redshift; this effect is what one usually calls redshift-space distortion. For baryon acoustic oscillation measurements this is an important contaminant which should be dealt with (Padmanabhan et al., 2012), but cosmological information can be extracted from this effect on its own. Kaiser, 1987 pointed out that, on large scales, these velocities will coherently respond to inhomogeneities, distorting the positions of galaxies to make under-dense regions seem larger, and over-dense regions seem smaller, with the net effect of an increase in the amplitude of clustering statistics. Moreover, this increase will depend on the linear matter growth rate, $f = \Omega_m^\gamma$, in which $\gamma = 0.5454$ if gravity is given by general relativity, but differs from this value for alternative theories (Gong, 2008). This opens a clear path for the measurement of $f$ and consequently for obtaining constraints on modified theories of gravity (Song and Percival, 2009). Pursuing this objective, many groups have dedicated efforts to the measurement of $f\sigma_8$ from RSDs – see figure (2.1) – and this has become a standard analysis performed in all galaxy spectroscopic surveys.

In the next sections we will develop the details of RSDs and how one can measure them using galaxy redshift surveys. This will also involve a discussion of the Alcock-

Paczyński effect.

## 2.1 Redshift-Space Distortions

The physical distance to an arbitrary galaxy can be written as $r(t) = a(t)\chi(t)$ in which $\chi(t)$ is the comoving distance to the galaxy, defined as

$$\chi(z) = \int_0^z \frac{cdz'}{H(z')}. \tag{2.1}$$

Taking the derivative of the physical distance with respect to cosmological time, and assuming the galaxy has no proper motion, i.e. $\dot{\chi} = 0$, we obtain

$$v(t) = \dot{r}(t) = \dot{a}(t)\chi(t) = H(t)r(t), \tag{2.2}$$

and the distance can be written as

$$r(t) = \frac{v(t)}{H(t)}. \tag{2.3}$$

Now let us imagine that the galaxy did have some proper motion $u = \dot{\chi}$, then taking the derivative of the physical distance would result in

$$v_s(t) = \dot{r}(t) = \dot{a}(t)\chi(t) + a(t)\dot{\chi}(t) = H(t)r(t) + a(t)u_{\parallel}(t). \tag{2.4}$$

Notice that $u$ is the derivative of the comoving distance, and therefore, it does not capture any peculiar motions perpendicular to the line of sight connecting observer and galaxy. If one would naively assume that this velocity is only due to the Hubble flow, the inferred comoving distance would be given by

$$\chi_s(t) = \frac{v_s(t)}{a(t)H(t)} = \chi(t) + \frac{u_{\parallel}(t)}{H(t)} = \chi(t) + \frac{\boldsymbol{u}(t)\cdot\hat{\boldsymbol{r}}}{H(t)}. \tag{2.5}$$

In the former equations, the subscript $s$ indicates redshift-space quantities, and no subscript indicates real-space quantities. Real-space is an idealization in which one would have perfect access to distances; in reality this is only possible in numerical simulations.

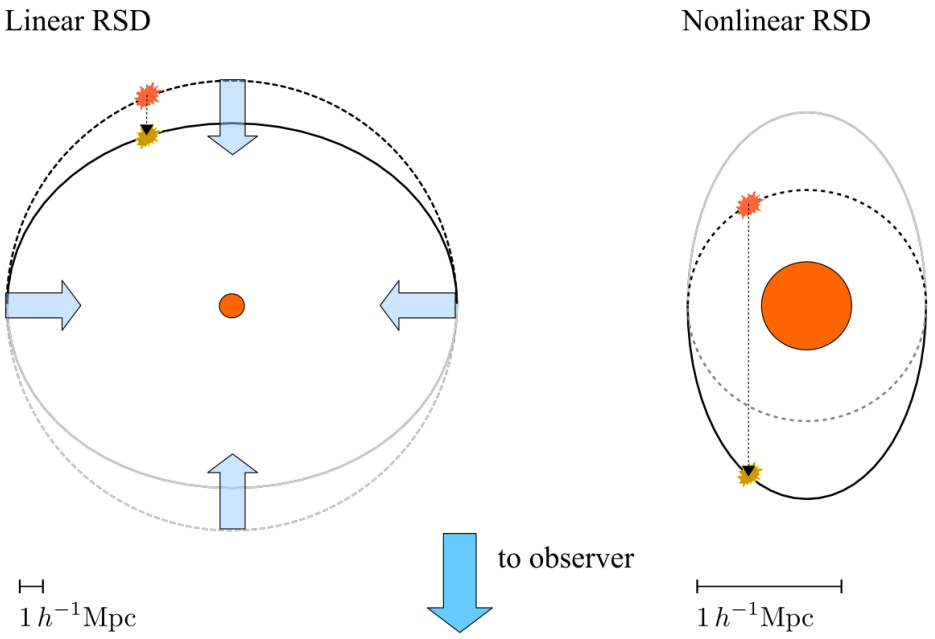


**Figure 2.2:** Galaxy distributions will be seen in a distorted manner in redshift space. Left panel shows the case of linear RSD, in which galaxies are moving slowly and coherently, so the observer sees structures slightly compressed along the line of sight. The right-hand panel shows the case of non-linear RSD, in which galaxies move with large, incoherent velocities; the distortions are so large that galaxies exchange places: the farthest seem to be the closest, and vice-versa. Extracted from (Dodelson and Schmidt, 2021)

Redshift-space, on the other hand, is the map of galaxies whose distances have been measured through their redshifts; this implies that our inference of their distance is biased by their peculiar motions, as illustrated above. It is easy to see from equation (2.5) that, in redshift-space, if the galaxy is moving towards us ($u < 0$), we would infer a smaller distance, and if the galaxy is moving away from us ($u > 0$), we would infer a larger distance.

Peculiar motions will be sourced by inhomogeneities exerting a gravitational pull over nearby galaxies. Looking at these motions locally, one sees an incoherent randomized picture, in which galaxies' velocities are independent of their position. However, (Kaiser, 1987) showed that if one zooms out to look at scales of the order $r \approx 10\text{Mpc}/h$, the velocities of the galaxies are coherently distributed, pointing out of density minima, and into density maxima. This is consistent with models of structure formation: at large scales, structures are evolving linearly, falling into potential wells in comoving shells of matter; as we go to smaller scales, however, we enter the non-linear regime, in which

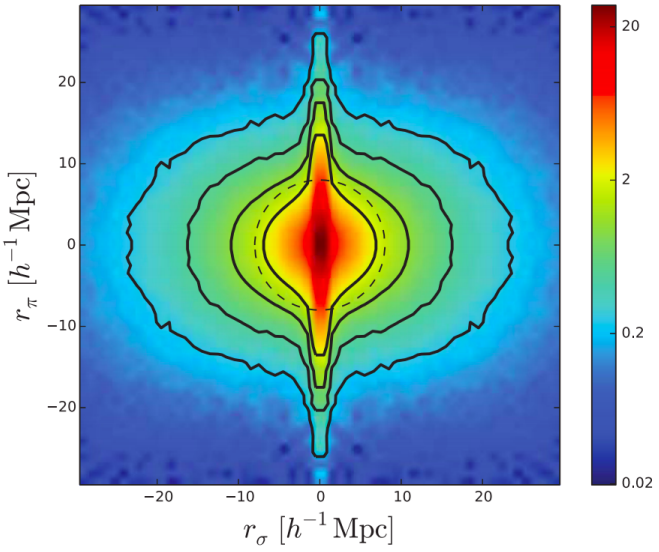


**Figure 2.3:** Two dimensional correlation function $\xi(r_\pi, r_\sigma)$ of SDSS-III CMASS galaxies. The coherent velocity field at linear scales generates the compression of the correlation function along $r_\pi$, and the large incoherent velocities at small scales generate the thin long features along $r_\pi$, known as Fingers of God. Extracted from (Reid et al., 2014).

shell-crossing and virialization take place, and velocities grow, becoming incoherent and randomized. Observations of galaxies on large scales will thus become compressed in the direction of the line-of-sight, and on small scales their positions will become highly distorted, generating long features along the line-of-sight, usually called Fingers of God (FOGs); one can see a representation of these effects in figure (2.2), and a measurement of the correlation function of galaxies in figure (2.3), in which both the Kaiser and FOG distortions can be easily identified. It is not hard to see that the effect of these distortions on clustering statistics will be that of increasing their amplitude at the large scales, and introducing a severe damping as we transition to the non-linear scales.

We can now formalize these arguments, following the treatment given by (Kaiser, 1987). Transforming between real and redshift space amounts to moving galaxies around, without creating or destroying any, so that the local number of galaxies should be conserved,

$$n(\boldsymbol{x})d^3x = n_s(\boldsymbol{x}_s)d^3x_s, \tag{2.6}$$

and we can rewrite this equation as

$$n_s(\boldsymbol{x}_s) = n(\boldsymbol{x})J, \tag{2.7}$$

in which $J = \left|\frac{d^3x}{d^3x_s}\right|$ is the Jacobian of the transformation, and $d^3x = x^2 \sin\theta dx d\theta d\phi$ is the volume element. The redshift space distortions will not change the angles, and therefore, from this expression and equation (2.5) we can write

$$J = \frac{x^2 dx}{x_s^2 dr_s} = \left(1 + \frac{u_\parallel}{xH}\right)^{-2} \left(1 + \frac{1}{H}\frac{\partial u_\parallel}{\partial x}\right)^{-1}. \tag{2.8}$$

The first term is of the order $\sim u/Hx$, and the second one is of the order $\sim ku/H$, because in Fourier space the derivative will drop a factor of $k$; we can see that the ratio of the second to the first is a factor of $kx$, in which $k$ is a certain wave-vector we wish to determine, and $x$ is the distance of the observer to the galaxy. The wave-vectors one is capable of observing will be limited by the size of the survey, $k_{max} \sim L^{-1}$, which is in general much smaller than the distance of the observer to the galaxies. Therefore, one is in general interested in the regime $kx \gg 1$, making the second term much more important than the first, and we can thus write

$$J = \left(1 - \frac{1}{H}\frac{\partial u_\parallel}{\partial x}\right) + \mathcal{O}(2), \tag{2.9}$$

allowing us to relate the overdensities in real and redshift space through

$$1 + \delta_s = [1 + \delta]\left(1 - \frac{1}{H}\frac{\partial u_\parallel}{\partial x}\right), \tag{2.10}$$

resulting in

$$\delta_s(\boldsymbol{x}) = \delta(\boldsymbol{x}) - \frac{1}{H}\frac{\partial u_\parallel}{\partial x} \tag{2.11}$$

Looking more closely at the velocity term, $u_\parallel = \boldsymbol{u} \cdot \hat{\boldsymbol{x}}$, in which $\boldsymbol{u}$ is the peculiar velocity of the galaxy, and $\hat{\boldsymbol{x}}$ is the line-of-sight vector, one can see that this depends on the particular position of the galaxy in order to define $\boldsymbol{x}$, i.e. the direction along which we will project $\boldsymbol{u}$ to obtain its relevant component changes with the position of each galaxy. To avoid having to deal with this issue, we introduce the distant-observer approximation, in which we fix $\hat{\boldsymbol{x}}$ to be one of the Cartesian axes, e.g.: $\hat{\boldsymbol{x}} = \hat{\boldsymbol{z}}$. Intuitively, if galaxies are very far away, and do not span a wide angular region, then the vector connecting observer and galaxy changes very little, and we can choose to fix one of the coordinate

axes along this approximate direction. This approximation will be very important in the next paragraph, allowing us to write the result of the Fourier transform in equation (2.14) analytically.

Using the continuity equation for matter, we can relate $\delta$ and $\boldsymbol{u}$ through the equation

$$\delta' + i\boldsymbol{k} \cdot \boldsymbol{u} = 0, \tag{2.12}$$

and using that the time dependence of $\delta$ is given by the growth factor $D_+(t)$, we can solve for the velocity in terms of the density

$$\boldsymbol{u}(\boldsymbol{k}) = ifH\frac{\boldsymbol{k}}{k^2}\delta(\boldsymbol{k}), \tag{2.13}$$

in which $f = \frac{d\ln D_+}{d\ln a}$ is the linear growth-rate[1]. Taking the Fourier transform of equation (2.10) we obtain

$$\begin{aligned}
\delta_s(\boldsymbol{k}) &= \int d^3\boldsymbol{x} e^{-i\boldsymbol{k}\cdot\boldsymbol{x}} \left[\delta(\boldsymbol{x}) - \frac{1}{H}\frac{\partial u_\parallel}{\partial x}\right] \\
&= \delta(\boldsymbol{k}) - if\int d^3\boldsymbol{x} e^{-i\boldsymbol{k}\cdot\boldsymbol{x}}\frac{\partial}{\partial x}\int \frac{d^3\boldsymbol{k}'}{(2\pi)^3} e^{i\boldsymbol{k}'\cdot\boldsymbol{x}}\frac{k'_z}{k'^2}\delta(\boldsymbol{k}') \\
&= \delta(\boldsymbol{k}) + f\int \frac{d^3\boldsymbol{k}'}{(2\pi)^3}\delta(\boldsymbol{k}')\mu^2 \underbrace{\int d^3\boldsymbol{x} e^{-i(\boldsymbol{k}-\boldsymbol{k}')\cdot\boldsymbol{x}}}_{(2\pi)^3\delta_D(\boldsymbol{k}-\boldsymbol{k}')} \\
&= \delta(\boldsymbol{k})\left(1 + f\mu^2\right),
\end{aligned} \tag{2.14}$$

in which $\mu = k_z/k$ is the cosine of the line-of-sight direction with the wavevector $\hat{\boldsymbol{k}}$, in the distant-observer approximation. This allows us to compute the redshift-space power spectrum, given by

$$P_s(\boldsymbol{k}) = \left(1 + f\mu^2\right)^2 P(\boldsymbol{k}). \tag{2.15}$$

The extra term appearing will increase power at the large scales, amplifying the clustering of structures; this is known as the Kaiser effect.

[1]Here, we have also used the fact that linear perturbation-theory predicts that the rotational of $\boldsymbol{u}$ will decay rapidly, and one can safely assume $\boldsymbol{w}(\boldsymbol{k}) = \boldsymbol{k} \times \boldsymbol{u} = 0$. This is what allows us to say that, in Fourier space, $\boldsymbol{u}$ will always be parallel to $\boldsymbol{k}$, as any component perpendicular to it would mean a non-zero rotational term.

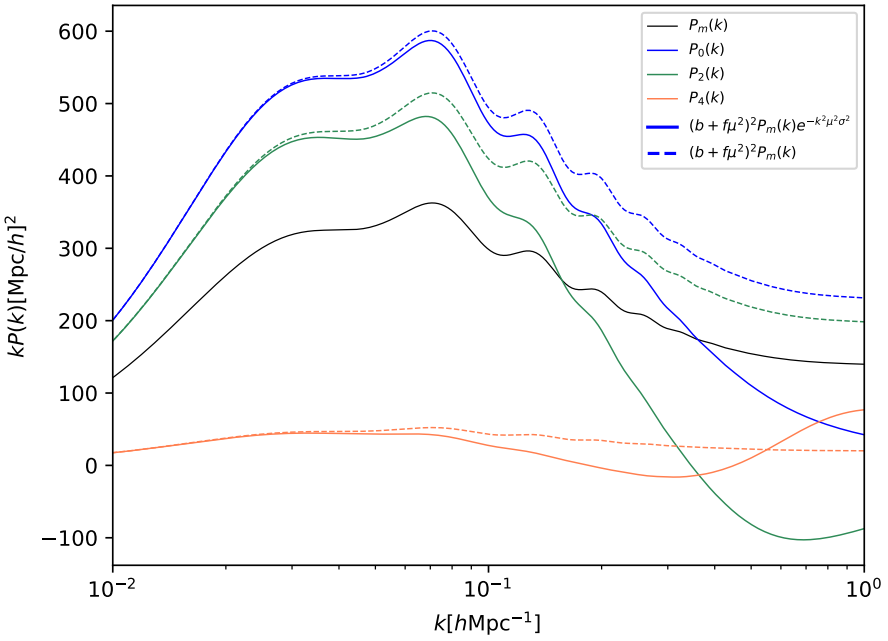


**Figure 2.4:** Power spectrum multipoles obtained from RSD model combining the Kaiser effect with an exponential velocity dispersion term. Notice the large amplitude increase of the monopole on large scales, and the severe damping of all multipoles at the transition from the linear to non-linear regime at $k \approx 0.1[h/\mathrm{Mpc}]$.

The effect of RSDs clearly destroys the isotropy of the power spectrum, even at the linear scales. Taking a density field $\delta_g(\boldsymbol{k})$ in redshift-space and computing[2]

$$\frac{1}{L^3}\int_{k_i}\frac{d^3\boldsymbol{k}}{V_s(k_i)}\langle\delta_g(\boldsymbol{k})\delta_g(-\boldsymbol{k})\rangle, \tag{2.16}$$

does not result in the power spectrum, but in the monopole of a Legendre polynomial expansion of the actual power spectrum. In the case of a Gaussian density field[3], the power spectrum suffices to perfectly characterize it, extracting all of the information contained in it. The monopole of the power spectrum however, does not possess this nice statistical property. Therefore, it is clear that part of the information has leaked to higher order multipoles, and one must compute them as well. Of course, an also valid way to attack this problem is to use $P(k,\mu)$ directly as the quantity to be measured and modeled; however, this would make visualization harder and would dilute the signal-to-noise ratio in a larger

[2]In this equation, the integral is computed over a spherical shell of radius $k_i$, and $V_s(k_i)$ is the volume of this shell.

[3]We know that this is not the case for the large-scale structure density field, because gravity itself will give rise to higher-order $n$-point functions, even if the primordial fluctuations were perfectly Gaussian

number of bins, making the Legendre polynomial expansion the preferred technique to deal with the angle dependence. This polynomial expansion can be written as

$$P(k,\mu) = \sum_{\ell=0}^{\infty} P_\ell(k)\mathcal{L}_\ell(\mu), \tag{2.17}$$

and the multipoles are given by

$$P_\ell(k) = \frac{2\ell+1}{2}\int d\mu P(k,\mu)\mathcal{L}_\ell(\mu). \tag{2.18}$$

Notice that $\ell$ can, in principle take any integer value, but since the Kaiser factor only contains even powers of $\mu$, all of the odd multipoles will be equal to zero. For increasing values of $\ell$, the multipoles decrease in importance, and most works, the present one included, focus only on the first two $\ell = 0, 2$. In figure (2.4) we show the multipoles of the power spectrum up to $\ell = 4$, and the effect of the exponential velocity dispersion on them.

## 2.2 Modelling RSDs

The Kaiser model is an accurate description of redshift-space distortions in the linear regime, and for observations approximately satisfying the distant observer approximation. However, as we go into the non-linear regime, equation (2.15) breaks down completely, since the linear relations between density and velocity are no longer valid, and neither is the assumption that the vorticity of this velocity field will remain to be null; the non-linear velocity field will introduce a large damping to the power spectrum at the small scales, which has been found to be well approximated by including a term

$$D_{FOG}(k) = \begin{cases} e^{-k^2\sigma^2\mu^2} & \text{Exponential} \\ \frac{1}{1+k^2\mu^2\sigma^2} & \text{Lorentzian} \end{cases} \tag{2.19}$$

into the expression for the anisotropic power spectrum (Peacock and Dodds, 1994). Although these functional forms are well motivated (Sheth, 1996), they are usually used as a completely phenomenological factor; in general, no information is obtained from the

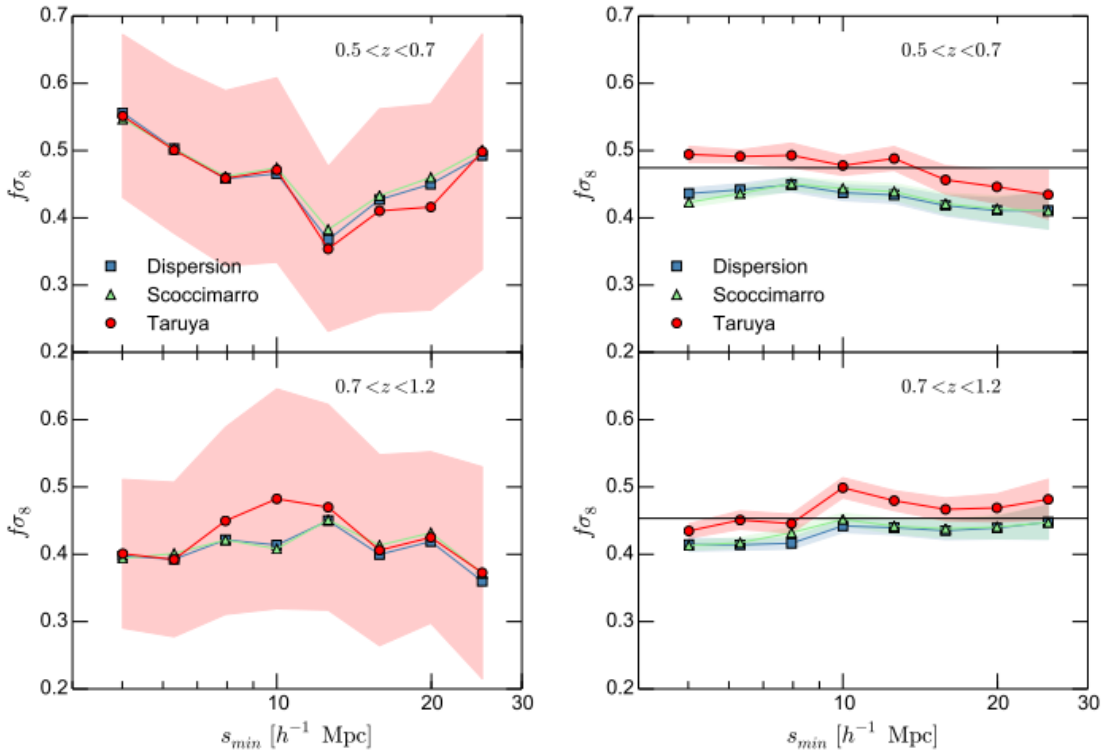


**Figure 2.5:** Constraints on $f\sigma_8$ obtained with correlation-function analysis of VIPERS data. The left panel shows the constraints obtained using VIPERS observations as a function of $s_{min}$, the minimum scale used in the analysis. The right panel shows a similar plot, but the constraints are now obtained from the mean of VIPERS like mocks. Shaded regions show the $1-sigma$ confidence interval. Extracted from (Pezzotta et al., 2017).

fitted value of $\sigma$, and one simply marginalizes over it as a nuisance parameter. In our work we will employ the exponential form; although the work of (Pezzotta et al., 2017) has found that the Lorentzian model is capable of better describing the simulated data, when using it to analyze real data from the VIPERS survey, it performs just as well as the exponential, due to the large statistical noise present in these measurements. Therefore, in the context of the analysis for the VIPERS survey, choosing between these models is virtually irrelevant.

Combining the linear and non-linear redshift-space distortion terms, the model for the redshift-space matter power spectrum can be written as

$$P_s(\boldsymbol{k}) = (1 + f\mu^2)^2 D_{FOG}(k) P(\boldsymbol{k}). \tag{2.20}$$

Notice that to constrain observations, one must have a model the power spectrum of galax-

ies, not matter. Unfortunately, the relation between these two is not at all simple (see Desjacques, Jeong, and Schmidt, 2018 for a comprehensive review). In the linear regime, however, they are related by a linear bias

$$\delta_g(\boldsymbol{k}) = b_1 \delta_m(\boldsymbol{k}), \tag{2.21}$$

and the value of $b_1$ will be highly sensitive to the properties of the galaxy population being modeled. Therefore, one can build a simple model for the clustering of galaxies as[4]

$$P_{gg}(\boldsymbol{k}) = b_1^2 (1 + \beta\mu^2)^2 D_{FOG}(k) P_{mm}(\boldsymbol{k}), \tag{2.22}$$

in which $\beta = f/b_1$ and $P_{mm}(k)$ is the non-linear matter power spectrum. Such a simplistic model should be tested, attempting to fit simulations, checking whether the recovered values for the parameters are biased due to inaccuracies of the model. Figure (2.5) shows the constraints obtained for $f\sigma_8$ from VIPERS mocks (right panel) and data (left panel) by (Pezzotta et al., 2017); blue dots labeled "Dispersion" show the performance of the referred model; the other two models are more complex and potentially more accurate, and are given in (Scoccimarro, 2004; Taruya, Nishimichi, and Saito, 2010). In the right panel one can see that the dispersion model introduces a bias as we decrease $s_{min}$; nevertheless, the left panel shows that for the level of precision of VIPERS data, all models perform equally well up to $s_{min} = 5\text{Mpc}/h$. This implies that one can safely extend a power-spectrum analysis of VIPERS data into the mildly non-linear regime of $k_{max} \approx 0.2h/\text{Mpc}$ with a simple model of RSDs and a linear bias relation (Pezzotta et al., 2017; de la Torre and Guzzo, 2012).

## 2.3 Alcock-Paczyński Effect

Through the preceding paragraphs we have discussed the distortions introduced in our measurements of the positions of galaxies due to their peculiar velocities and our necessity of inferring distances from redshifts. From basic cosmology, we know that the

[4]This expression makes it clear that there is a degeneracy between the value of $f$, $b_1$, and the amplitude of $P_{mm}(\boldsymbol{k})$, represented by $\sigma_8$; this explains why constraints are usually on the combination $f\sigma_8$ and $b_1\sigma_8$, instead of the single parameters.

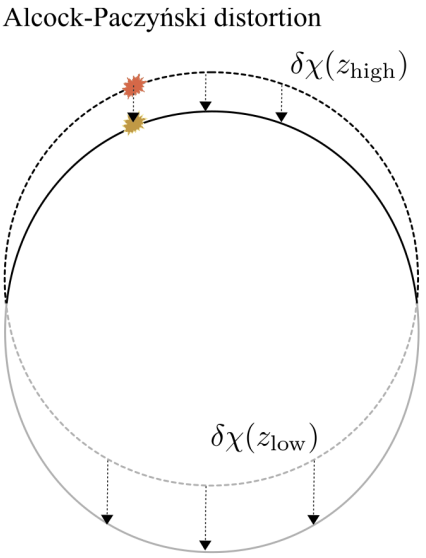


**Figure 2.6:** Effect of assuming the wrong fiducial cosmology in the determination of galaxy positions from redshfits. The relation between distance and redshift changes with $z$, and therefore, a circular distribution of tracers will look elliptical in the wrong cosmology. Extracted from (Dodelson and Schmidt, 2021)

comoving distance is defined as

$$\chi(z) = \int_0^z \frac{c\,dz'}{H(z')}, \tag{2.23}$$

in which the Hubble function is given by

$$H(z) = H_0\sqrt{\Omega_m(1+z)^{-3} + \Omega_\Lambda(1+z)^{1+w} + \Omega_r(1+z)^{-4} + \Omega_k(1+z)^{-2}}, \tag{2.24}$$

and the natural question which arises is: which parameters should we use to compute equation (2.23)? The answer is that one must initially choose a set of fiducial cosmological parameters $\boldsymbol{\theta}_{fid}$; unless we somehow know the answer beforehand, we will be slightly wrong in our initial guess, and this will provoke distortions in the determination of $\chi$– this is known as the Alcock-Paczyński effect (Alcock and Paczyński, 1979). The fiducial comoving distance will be different from the real one by $\delta\chi(z) = \chi(z) - \chi_{fid}(z)$, which might be positive or negative; notice that this difference also evolves with redshift, and therefore, the galaxies will not be simply translated through space preserving their distribution, but there will also be a distortion to the shape of their organization in space, as illustrated in figure (2.6). Although this is an important effect in general, (de la Torre

et al., 2013; Pezzotta et al., 2017) have shown that this has a very small effect on the recovered value of the matter growth-rate from VIPERS data, and therefore, we do not include it in our analysis as well. Instead, we will keep the parameters fixed to the fiducial cosmology, and vary only $f$, $\sigma$ and $b$.

# Chapter 3

# Power Spectrum Estimation

In this chapter, we will discuss how to compute power spectra in a way that is accurate, precise and computationally feasible. Since the power spectrum is a quantity defined in Fourier space, we will take advantage of the highly optimized Fast Fourier-Transform (hereafter FFT) algorithms to speed up the calculations. One limitation arising from this is that, to use these algorithms, one must first interpolate the density field onto a regular grid in position space; this interpolation will be done by assuming some density profile for the particles, and computing the total density at the grid positions. These density profiles are completely unphysical, and are simply destined to improve the accuracy of the interpolation, and thus, one must deconvolve them from the final density estimation to obtain an unbiased result – see (Jing, 2005). Moremover, FFT algorithms implicitly assume that the input data is periodic, which is never the case for real observations; this wrong assumption will introduce systematic errors in the Fourier transforms which cannot be easily corrected; one possible way to correct for this effect was introduced by Sefusatti et al., 2016 and we will follow their approach closely.

The preceding paragraph dealt with the question of how to *accurately* determine power spectra; another question to be addressed is that of how to improve the *precision* with which one determines the power spectrum from a certain dataset. The seminal work of (Feldman, Kaiser, and Peacock, 1994) (hereafter FKP) provided a way to assign weights to different regions of the galaxy density field such that the power spectrum esti-

mated from this weighted field is the one with the smallest possible errors. This work had the limitation of considering all galaxies to have equal biases, and several ideas were proposed in the following years to improve upon this, allowing for the existence of multiple types of tracers of the density field with different biases (Percival, Verde, and Peacock, 2004; Abramo and Leonard, 2013; Abramo, Secco, and Loureiro, 2015). In what follows we will focus on describing the FKP estimator and the Multi-Tracer Optimal Estimator (MTOE), proposed by (Abramo, Secco, and Loureiro, 2015), to illustrate the procedures used in finding the optimal estimators of statistical quantities, and also because these estimators will be used further ahead to compute spectra from simulations and real data.

## 3.1 Interpolating onto Regular Grid

As we have already noted, in order to estimate $n$-point functions in Fourier space using FFTs, our data must be distributed in a regular grid. To obtain a regular grid of densities from a general particle distribution we must then perform some kind of interpolation. The traditional way of doing this is to imagine that the particles are not point-like, but have some density distribution. One can then compute the density inside a certain cell by summing the contributions of different particles, arising from the overlapping of their density profiles with the cell region.

Let us imagine we have $N$ particles located at $\boldsymbol{x}_i$, and assume they have a point-spreading function given by $S(\boldsymbol{x} - \boldsymbol{x}_i)$. Then it is not hard to see that the contribution of all particles to the number density of cell $j$ is given by

$$n^G(\boldsymbol{x}_j) = \sum_{i=1}^{N} \frac{1}{H^3} \int T\left(\frac{\boldsymbol{x} - \boldsymbol{x}_j}{H}\right) S(\boldsymbol{x} - \boldsymbol{x}_i) d^3\boldsymbol{x}, \tag{3.1}$$

in which $H$ is the side of the cubic cell, and $T(\boldsymbol{x})$ is a separable top-hat function, meaning $T(\boldsymbol{x}) = T(x)T(y)T(z)$, each of the 1-dimensional components being given by

$$T(x) = \begin{cases} 1 & \text{if } |x| < 1/2 \\ 0 & \text{if } |x| > 1/2. \end{cases} \tag{3.2}$$

Putting the summation inside the integral, we can write

$$\begin{aligned} n^G(\boldsymbol{x}_j) &= \int d^3\boldsymbol{x}' n(\boldsymbol{x}') \underbrace{\frac{1}{H^3} \int d^3\boldsymbol{x} T\left(\frac{\boldsymbol{x}-\boldsymbol{x}_j}{H}\right) S(\boldsymbol{x}-\boldsymbol{x}')}_{W(\boldsymbol{x}'-\boldsymbol{x}_j)} \\ &= \int d^3\boldsymbol{x}' n(\boldsymbol{x}') W(\boldsymbol{x}'-\boldsymbol{x}_j) \end{aligned} \tag{3.3}$$

and $W$ is usually called the window function of the particle assignment scheme.

From this last expression, one can see then that the interpolated particle number density is the convolution of $n(\boldsymbol{x})$ with the window function. Let us remind ourselves that one can compute the density contrast as

$$\delta(\boldsymbol{x}) = \frac{n(\boldsymbol{x})}{\bar{n}} - 1, \tag{3.4}$$

and therefore, using the convolution theorem, one can see that, in Fourier space, the interpolated density contrast becomes

$$\delta^G(\boldsymbol{k}_j) = \delta(\boldsymbol{k}_j)\tilde{W}(\boldsymbol{k}_j). \tag{3.5}$$

After interpolating onto a regular grid, one must then divide the resulting densities by the window function evaluated at the same grid positions, to recover the real density field.

In the following paragraphs we summarize the most commonly utilized point spreading functions. All of these have the property of being separable, that is, $S(\boldsymbol{x}) = S(x)S(y)S(z)$, since that makes computations much simpler. Due to this property, we will define them by giving the expression of their one-dimensional components.

**NGP** We begin with the simplest one, the nearest grid-point assignment, defined by its one dimensional point-spread function, given simply by a Dirac delta

$$S(x) = \delta_D(x), \tag{3.6}$$

and therefore, its window function is given by a top-hat,

$$W(x) = \frac{1}{H}\int_{x-H/2}^{x+H/2} \delta(x'-x)dx' = \begin{cases} 1/H & \text{if } |x| \leq H/2 \\ 0 & \text{if } |x| > H/2. \end{cases} \tag{3.7}$$

As we can see, this is an extremely simplified interpolation scheme, in which one assigns the particle contribution to the cell in which it lies. It is also interesting to obtain the window function's Fourier transform, given by

$$\begin{aligned} \tilde{W}_{NGP}(k) = &\int dx e^{-ikx} W(x) = \frac{1}{-ikH}\left(e^{-ikH/2} - e^{ikH/2}\right) \\ =&\frac{\sin(kH/2)}{(kH/2)}, \end{aligned} \tag{3.8}$$

implying that the three-dimensional case is given by

$$\tilde{W}(\boldsymbol{k}) = \frac{\sin(k_x H/2)}{(k_x H/2)}\frac{\sin(k_y H/2)}{(k_y H/2)}\frac{\sin(k_z H/2)}{(k_z H/2)}, \tag{3.9}$$

**CIC** The cloud-in-cell assignment can be defined by its one dimensional point spread function, given by a top-hat distribution

$$S_{CIC}(x) = \frac{1}{H}\begin{cases} 1 & \text{if } |x| < H/2 \\ 0 & \text{if } |x| > H/2 \end{cases} \tag{3.10}$$

and therefore, its window function will be given by

$$W_{CIC}(x) = \frac{1}{H}\begin{cases} 1 - |x|/H & \text{if } |x| \leq H \\ 0 & \text{if } |x| > H. \end{cases} \tag{3.11}$$

From equation 3.3 one can see that this window function will be the convolution of two top-hat functions. We already derived the Fourier transform of a top-hat function above, and using the convolution theorem one can write

$$W_{CIC}(k) = \left[\frac{\sin(kH/2)}{kH/2}\right]^2, \tag{3.12}$$

so that its tridimensional version will be given by

$$\tilde{W}_{CIC}(\boldsymbol{k}) = \left[\frac{\sin(k_x H/2)}{(k_x H/2)}\frac{\sin(k_y H/2)}{(k_y H/2)}\frac{\sin(k_z H/2)}{(k_z H/2)}\right]^2, \tag{3.13}$$

**TSC** As a final example we have the triangular-shaped cloud interpolation method, which can be defined by its point-spreading function

$$S_{TSC}(x) = \frac{1}{H}\begin{cases} 1 - |x|/H & \text{if } |x| \leq H \\ 0 & \text{if } |x| > H. \end{cases} \tag{3.14}$$

Notice that this is precisely the same expression as the window function in the CIC case. Therefore, its window function will be given by

$$W_{TSC}(x) = \frac{1}{H}\begin{cases} \frac{3}{4} - \left(\frac{x}{H}\right)^2 & \text{if } |x| \leq \frac{H}{2} \\ \frac{1}{2}\left(\frac{3}{2} - \frac{|x|}{H}\right)^2 & \text{if } \frac{H}{2} \leq |x| \leq \frac{3H}{2} \\ 0 & \text{otherwise} \end{cases} \tag{3.15}$$

which is simply the convolution of three top-hat functions, and therefore, due to the convolution theorem, its Fourier transform can be obtained immediately

$$\tilde{W}_{TSC}(k) = \left[\frac{\sin(kH/2)}{kH/2}\right]^3, \tag{3.16}$$

and its tridimensional version will be given by

$$\tilde{W}_{TSC}(\boldsymbol{k}) = \left[\frac{\sin(k_x H/2)}{(k_x H/2)}\frac{\sin(k_y H/2)}{(k_y H/2)}\frac{\sin(k_z H/2)}{(k_z H/2)}\right]^3, \tag{3.17}$$

## 3.2 FFT-based Estimation

As stated earlier, to make use of FFT algorithms, one must have a field evaluated at a regularly spaced grid of positions, and the algorithm implicitly assumes that the input data is periodic. To understand what are the effects of this on the Fourier transform of the density field, we will begin by representing the discrete overdensity field with the help of

a sampling function[1],

$$\Pi(\boldsymbol{x}) = \sum_{\boldsymbol{n}} \delta^D(\boldsymbol{x} - \boldsymbol{n}), \tag{3.18}$$

in which $\boldsymbol{n}$ is an integer triplet, and the sampled field in real space can be written as

$$\delta^G(\boldsymbol{x}) = \delta(\boldsymbol{x})\Pi(\boldsymbol{x}/H). \tag{3.19}$$

One can then use the convolution theorem to obtain an expression for the Fourier transform of this field

$$\tilde{\delta}^G(\boldsymbol{k}) = \int d^3\boldsymbol{k}'\tilde{\Pi}(\boldsymbol{k}')\tilde{\delta}(\boldsymbol{k} - \boldsymbol{k}'). \tag{3.20}$$

Let us then compute the Fourier transform of the sampling function; in what follows we'll compute this for the one-dimensional sampling function, and the three-dimensional case can be done analogously,

$$\begin{aligned}
\tilde{\Pi}(k) =& \int dx e^{-ikx} \sum_{n=-\infty}^{\infty} \delta^D(x - n) \\
=& \sum_{n=-\infty}^{\infty} e^{-ikn} \\
=& \frac{1 - e^{ik(N+1)}}{1 - e^{ik}} + \frac{1 - e^{-ik(N+1)}}{1 - e^{-ik}} - 1 \\
=& \frac{1 - e^{ik(N+1)} - e^{ik} + e^{-ikN}}{1 - e^{ik}} - 1 \\
=& \frac{e^{-ikN} - e^{ik(N+1)}}{1 - e^{ik}} = (2N+1)\frac{\text{sinc}\left((2N+1)k/2\right)}{\text{sinc}\left(k/2\right)}.
\end{aligned} \tag{3.21}$$

It is easy to see that as $k \to 2m\pi$, with $m$ integer, this function goes to $(2N + 1)$, at which it attains its maximum value; moreover, the width of the peak around $k = 2m\pi$ will be of approximately $1/(2N + 1)$, allowing us to say that when $N \to \infty$ this can be approximated by

$$\tilde{\Pi}(k) = 2\pi \sum_{m=-\infty}^{\infty} \delta^D(k - 2m\pi). \tag{3.22}$$

[1]In reality, this sampling function would be finite in $\boldsymbol{n}$, but we maintain the summation up to infinite values of $\boldsymbol{n}$ because that's essentially what the FFT does, it assumes that the data is periodic, and thus has a value for all $\boldsymbol{n}$.

The sampling function is separable and therefore one can generalize this easily to three dimensions, obtaining

$$\tilde{\Pi}(\boldsymbol{k}) = (2\pi)^3 \sum_{\boldsymbol{m}} \delta^D(\boldsymbol{k} - 2\boldsymbol{m}\pi), \tag{3.23}$$

and using the result from equation 3.20 we obtain the Fourier transform of the sampled density

$$\begin{aligned} \delta_1^G(\boldsymbol{k}) &= (2\pi)^3 \int \frac{d^3\boldsymbol{k}'}{(2\pi)^3} \delta(\boldsymbol{k} - \boldsymbol{k}') \sum_{\boldsymbol{m}} \delta^D(\boldsymbol{k}' - 2\boldsymbol{m}\pi/H) \\ &= \sum_{\boldsymbol{m}} \delta\left(\boldsymbol{k} - \frac{2\boldsymbol{m}\pi}{H}\right). \end{aligned} \tag{3.24}$$

Then it becomes clear that the Fourier transform of this quantity is given by the sum over many images of this same function displaced by multiples of $2\pi/H$; this phenomenon is known as aliasing. For low $k$ values, subtracting a multiple of $2\pi/H$ will make this argument be negative, with an absolute value much larger than the Nyquist frequency, $k_N = \pi/H$, and therefore these contributions will come from regions which are not even supported by the grid, and therefore will be highly suppressed. For $k$ values which are around the Nyquist frequency, however, when one subtracts $2\pi/H$, the argument will have an absolute value comparable to $k_N$ and therefore these contributions will come from regions where the amplitude of $\delta(\boldsymbol{k} - 2\pi/H)$ is comparable to that of $\delta(\boldsymbol{k})$, thus biasing it greatly.

Notice also that these FFTs are being performed, in general, over density fields which have been obtained through one of the interpolation schemes described above, and therefore, their densities relate to the real ones through equation (3.5), and we can write an expression for $\delta_1^G$ combining both effects

$$\delta_1^G(\boldsymbol{k}) = \sum_{\boldsymbol{m}} \delta(\boldsymbol{k} - 2\boldsymbol{m}k_N) W(\boldsymbol{k} - 2\boldsymbol{m}k_N), \tag{3.25}$$

in which $k_N = \pi/H$ is the Nyquist frequency. This implies that when computing the

power spectrum one will obtain

$$\widehat{P}(\boldsymbol{k}) = \sum_{\boldsymbol{m}} P(\boldsymbol{k} - 2\boldsymbol{m}k_N)|W(\boldsymbol{k} - 2\boldsymbol{m}k_N)|^2 + \frac{1}{\bar{n}} \sum_{\boldsymbol{m}} |W(\boldsymbol{k} - 2\boldsymbol{m}k_N)|^2. \tag{3.26}$$

This expression was first derived by (Jing, 2005), and shows how the shot-noise is also modified by the mass-assignment scheme (hereafter MAS) window and aliasing effect, and subtracting the naive expectation $\frac{1}{\bar{n}}$ can lead to relevant differences.

### 3.2.1 Interlacing

A method to partially correct for the effect of aliasing was proposed by (Sefusatti et al., 2016), and we shall follow their treatment in this section. Let us look at the result of interpolating this same density field onto a grid displaced by half cell-size; this can be written as

$$\delta_2^G(\boldsymbol{k}) = \int d^3\boldsymbol{x} \Pi \left( \frac{\boldsymbol{x}}{H} + \frac{1}{2} \right) \delta(\boldsymbol{x}) e^{-i\boldsymbol{k}\cdot\boldsymbol{x}}. \tag{3.27}$$

The shift theorem for discrete Fourier-transforms (hereafter DFTs) implies that

$$\boxed{f(x - \Delta) \leftrightarrow e^{-i\Delta k} \tilde{f}(k)} \tag{3.28}$$

and we can apply this to our expression above, to see that

$$\begin{aligned} \delta_2^G(\boldsymbol{k}) &= \sum_{\boldsymbol{k'}} e^{i(k'_x + k'_y + k'_z)H/2} \delta(\boldsymbol{k} - \boldsymbol{k'}) \Pi(\boldsymbol{k'}) \\ &= \sum_{\boldsymbol{m}} e^{i\pi(m_x + m_y + m_z)} \delta \left( \boldsymbol{k} - \frac{2\boldsymbol{m}\pi}{H} \right) \\ &= \sum_{\boldsymbol{m}} (-1)^{(m_x + m_y + m_z)} \delta \left( \boldsymbol{k} - \frac{2\boldsymbol{m}\pi}{H} \right). \end{aligned} \tag{3.29}$$

Looking at equation (3.24) one can immediately see that by taking the average of $\delta_1^G$ and $\delta_2^G$, one obtains

$$\begin{aligned} \delta^G(\boldsymbol{k}) =& \frac{1}{2} \sum_{\boldsymbol{m}} (1 + (-1)^{m_x + m_y + m_z}) \delta \left( \boldsymbol{k} - \frac{2\boldsymbol{m}\pi}{H} \right) \\ =& \frac{1}{2} \sum_{\boldsymbol{m}} \theta_{\boldsymbol{m}} \delta \left( \boldsymbol{k} - \frac{2\boldsymbol{m}\pi}{H} \right), \end{aligned} \tag{3.30}$$

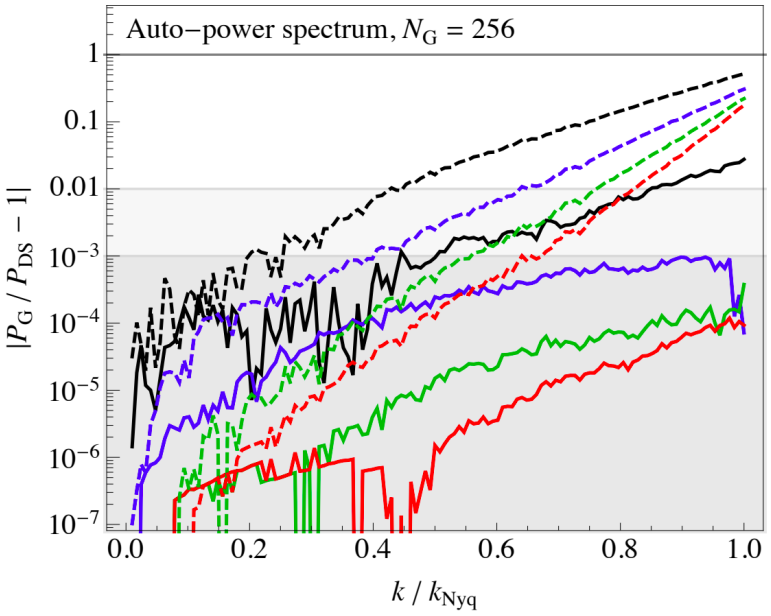


**Figure 3.1:** Fractional difference of spectra computed with FFT and spectra computed by performing the Fourier transform exactly; dashed lines show the comparison with FFT spectra before applying interlacing, and solid lines show the comparison with interlaced spectra. Blue, green and red curves represent, respectively, spectra computed from density fields interpolated using NGP, CIC and TSC MASs. The $x-$axis shows the ratio of the wave-vector to the Nyquist frequency, $k_{\rm Nyq} = \pi/H$. Extracted from (Sefusatti et al., 2016).

in which we have

$$\theta_{\boldsymbol{m}} = \begin{cases} 1 & \text{if } m_x + m_y + m_z \text{ is even;} \\ 0 & \text{if } m_x + m_y + m_z \text{ is odd.} \end{cases} \tag{3.31}$$

It is not hard to see that all the odd aliasing contributions are removed, most notably the ones which have $\boldsymbol{m} = 1$, which are the largest ones. In figure (3.1) one can see the fractional difference between power spectra computed using FFT and power spectra computed doing the Fourier transform exactly; there is a remarkable reduction in the biases, and using CIC and interlacing one can already reduce these errors to less than $0.1\%$, enough for the analysis of current and upcoming cosmological data.

### 3.2.2 Shot-Noise

Equation (3.26) tells us that if the shot-noise term is well described by a constant, the effects of the MAS window and FFT aliasing will change its value, multiplying it by

$$\sum_{\boldsymbol{m}} |W(\boldsymbol{k} - 2\boldsymbol{m}k_N)|^2. \tag{3.32}$$

For the case of the interpolation schemes described above, it is possible to compute this summation analytically,

$$\sum_{\boldsymbol{m}} |W(\boldsymbol{k} - 2\boldsymbol{m}k_N)|^2 = \begin{cases} 1 & \text{NGP} \\ \Pi_{i=1}^{3}\left[1 - \frac{2}{3}\sin^2\left(\frac{\pi k_i}{2k_N}\right)\right] & \text{CIC} \\ \Pi_{i=1}^{3}\left[1 - \sin^2\left(\frac{\pi k_i}{2k_N}\right) + \frac{2}{15}\sin^4\left(\frac{\pi k_i}{2k_N}\right)\right] & \text{TSC.} \end{cases} \tag{3.33}$$

Therefore, one possible way of correctly subtracting shot-noise from the estimated spectra is to:

- Compute $\widehat{P}'(\boldsymbol{k}) = \frac{1}{L^3}\langle\delta^G(\boldsymbol{k})\delta^G(-\boldsymbol{k})\rangle$ from interpolated grid, using FFTs;
- Use equations above to correctly subtract shot noise,

$$\widehat{P}' \to \widehat{P}' - \frac{1}{\bar{n}}\sum_{\boldsymbol{m}} |W(\boldsymbol{k} - 2\boldsymbol{m}k_N)|^2;$$

- Do approximate deconvolution of the MAS window function, resulting in a power spectrum estimator,

$$\begin{aligned} \widehat{P}(\boldsymbol{k}) &= \frac{1}{|W(\boldsymbol{k})|^2}\left[\frac{1}{L^3}\langle\delta^G(\boldsymbol{k})\delta^G(-\boldsymbol{k})\rangle - \frac{1}{\bar{n}}\sum_{\boldsymbol{m}} |W(\boldsymbol{k} - 2\boldsymbol{m}k_N)|^2\right] \\ \widehat{P}(k_i) &= \left[\widehat{P}(\boldsymbol{k})\right]_{\Theta(k_i)}, \end{aligned} \tag{3.34}$$

  in which $\Theta(k_i)$ symbolizes the operation of averaging over spherical shells of radius $k_i$ in Fourier space.

Another possibility is to use interlacing and deconvolve the window function before sub-

tracting shot-noise:

- Compute interlaced grids $\delta_1^G$ and $\delta_2^G$, and from them, a grid with reduced aliasing effects,
$$\delta_{12}^G(\boldsymbol{k}) = \frac{1}{2}\left(\delta_1^G(\boldsymbol{k}) + \delta_2^G(\boldsymbol{k})\right) \tag{3.35}$$
- Compute from this the power spectrum estimator $\widehat{P}'(\boldsymbol{k}) = \frac{1}{L^3}\langle\delta_{12}^G(\boldsymbol{k})\delta_{12}^G(-\boldsymbol{k})\rangle$
- Approximately deconvolve the window function from this estimator, and then directly subtract the usual shot noise, obtaining the estimator
$$\begin{aligned}\widehat{P}(\boldsymbol{k}) &= \frac{1}{L^3|W(\boldsymbol{k})|^2}\langle\delta_{12}^G(\boldsymbol{k})\delta_{12}^G(-\boldsymbol{k})\rangle - \frac{1}{\bar{n}} \\ \widehat{P}(k_i) &= \left[\widehat{P}(\boldsymbol{k})\right]_{\Theta(k_i)}\end{aligned} \tag{3.36}$$

In our estimations of the power spectrum, we will choose to employ the second approach. This scheme will have to be slightly modified in order to apply the aliasing method to the computation of the multipoles of the power spectrum, and we describe the updated version of the scheme in the end of the next section.

## 3.3 Estimating Power-Spectrum Multipoles

Redshift-space distortions (RSDs) have become one of the most powerful tools to constrain cosmological parameters, in particular those controlling the amplitude and growth of the matter perturbations, i.e. $\sigma_8$ and $f$. This effect will break the isotropy of the galaxy distribution, since the distortions in their redshifts due to local peculiar motions will depend on the angle of their velocities with the line of sight of the observer (see Chapter 2). This implies that the three-dimensional power spectrum will have some angular dependency, and therefore, if we expand it into a Legendre polynomial basis, there will be signal in multipoles of $\ell > 0$; one could then measure these multipoles, determining the strength of these distortions, which can be used to constrain the combination $f\sigma_8$.

However, estimating these multipoles from a population of galaxies presents its own difficulties. RSDs will compromise the statistical homogeneity of power-spectrum esti-

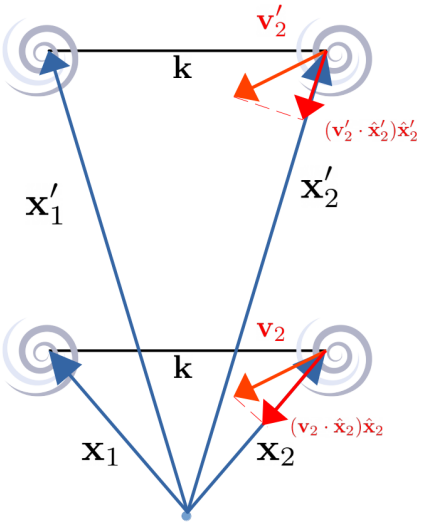


**Figure 3.2:** In this figure we suppose $\boldsymbol{v}_2 = \boldsymbol{v}_2'$, and we can see that because $\boldsymbol{x}_2 \neq \boldsymbol{x}_2'$, the projection of this velocity along the line of sight will be different for the two galaxies. The distortions provoked by peculiar motions depend precisely on this projection, and therefore, on the position of the galaxy.

mators, as can be seen from figure (3.2): both pairs of galaxies contribute to the same $\boldsymbol{k}$, but their contributions will depend on the distortions generated from peculiar motions, which in turn will depend on the positions of the galaxies, even if they have the same peculiar velocities. Usually the approach has been to neglect this issue, employing the plane-parallel approximation, i.e. fixing the line of sight to be one of the coordinate axes, $\hat{\boldsymbol{r}} = \hat{\boldsymbol{z}}$. This approximation is valid for observations within a small angular patch, but breaks down for wide-angle surveys.

Given that we lost spatial homogeneity, a natural generalization is to define a local estimator of the power spectrum,

$$\widehat{P}_{\text{local}}\left(\mathbf{k}, \mathbf{x}\right) \equiv \int \frac{d^3 x_{12}}{(2\pi)^3} \delta_s\left(\mathbf{x} + \mathbf{w}_1\right) \delta_s\left(\mathbf{x} + \mathbf{w}_2\right) \mathrm{e}^{-i\mathbf{k}\cdot\mathbf{x}_{12}}, \tag{3.37}$$

in which $\mathbf{x}_{12} = \mathbf{w}_1 - \mathbf{w}_2$. This makes it simple to write a completely general expression for the power-spectrum multipoles, by integrating the former expression multiplied by a Legendre polynomial evaluated at the relevant angle $\mu = \hat{\boldsymbol{k}} \cdot \hat{\boldsymbol{x}}$

$$\widehat{P}_\ell(k) = (2\ell + 1) \int d^3\boldsymbol{x} \int \frac{d\Omega_k}{4\pi} \widehat{P}_{\text{local}}(\boldsymbol{k}, \boldsymbol{x}) \mathcal{L}_\ell(\hat{\boldsymbol{k}} \cdot \hat{\boldsymbol{x}}). \tag{3.38}$$

Using the definition for $\widehat{P}_{\rm local}$, this can be rewritten as

$$\widehat{P}_\ell(k) = (2\ell+1)\int \frac{d\Omega_k}{4\pi}\int d^3\boldsymbol{x}_1 d^3\boldsymbol{x}_2 e^{-i\boldsymbol{k}\cdot\boldsymbol{x}_{12}}\mathcal{L}_\ell(\hat{\boldsymbol{k}}\cdot\hat{\boldsymbol{x}})\delta_s\left(\boldsymbol{x}_1\right)\delta_s\left(\boldsymbol{x}_2\right) \tag{3.39}$$

in which $\boldsymbol{x}_{12} = \boldsymbol{x}_1 - \boldsymbol{x}_2$. This expression, for the specific case of $\ell = 2$ was first presented in Yamamoto et al., 2006, and is known as the Yamamoto estimator. Equation (3.39) takes an important step in formalizing power-spectrum multipole measurements beyond the plane-parallel approximation. However, closer inspection reveals that one single evaluation would require two volume integrals and one more integral over $k$ angular coordinates; moreover, the fact that the integrals in $\boldsymbol{x}_1$ and $\boldsymbol{x}_2$ cannot be separated prevents us from implementing them as FFTs, and it becomes clear that computing this would be prohibitively slow.

To circumvent this issue, (Blake et al., 2011; Beutler et al., 2014; Scoccimarro, 2015; Bianchi et al., 2015) proposed that one could substitute $\boldsymbol{x} \to \boldsymbol{x}_1$ in equation (3.39); this allows for the two integrals in this expression to be separated, resulting in

$$\widehat{P}_\ell(k) = (2\ell+1)\int \frac{d\Omega_k}{4\pi}\int d^3\boldsymbol{x}_1 e^{-i\boldsymbol{k}\cdot\boldsymbol{x}_1}\mathcal{L}_\ell(\hat{\boldsymbol{k}}\cdot\hat{\boldsymbol{x}}_1)\delta_s\left(\boldsymbol{x}_1\right)\int d^3\boldsymbol{x}_2\delta_s\left(\boldsymbol{x}_2\right)e^{i\boldsymbol{k}\boldsymbol{x}_2}, \tag{3.40}$$

which motivates the definition of a local multipole overdensity

$$\delta_\ell(\boldsymbol{k}) = \int d^3\boldsymbol{x} e^{-i\boldsymbol{k}\cdot\boldsymbol{x}}\mathcal{L}_\ell(\hat{\boldsymbol{k}}\cdot\hat{\boldsymbol{x}})\delta_s(\boldsymbol{x}), \tag{3.41}$$

and the power spectrum multipole can be rewritten as the cross-correlation between the local multipole and monopole overdensities,

$$\widehat{P}_\ell(k) = (2\ell+1)\int \frac{d\Omega_k}{4\pi}\delta_\ell(\boldsymbol{k})\delta_0(-\boldsymbol{k}). \tag{3.42}$$

This expression can be efficiently evaluated, since the $\delta_\ell$ can now be written as a sum over

several FFTs; let us look at the specific case $\ell = 2$ to see why this happens:

$$\begin{aligned}\delta_2(\boldsymbol{k}) =& \int d^3\boldsymbol{x} e^{-i\boldsymbol{k}\cdot\boldsymbol{x}} \mathcal{L}_2(\hat{\boldsymbol{k}}\cdot\hat{\boldsymbol{x}})\delta_s(\boldsymbol{x}) \\ =& \frac{3}{2}\hat{k}_i\hat{k}_j \int d^3\boldsymbol{x}\delta_s(\boldsymbol{x})\hat{x}_i\hat{x}_j e^{-i\boldsymbol{k}\cdot\boldsymbol{x}} - \frac{1}{2}\int d^3\boldsymbol{x}\delta_s(\boldsymbol{x})e^{-i\boldsymbol{k}\cdot\boldsymbol{x}} \\ =& \frac{3}{2}\hat{k}_i\hat{k}_j Q_{ij}(\boldsymbol{k}) - \frac{1}{2}\delta_0(\boldsymbol{k}),\end{aligned} \tag{3.43}$$

in which we have substituted the expression for the second order Legendre polynomial, $\mathcal{L}_2(\mu) = \frac{1}{2}[3\mu^2 - 1]$, and repeated indices encode an implicit summation. Computing $Q_{ij}$ requires 6 FFTs, and $\delta_0$ requires 1, so that the computation of the quadrupole requires a total of 7 FFTs; a similar structure is maintained for the higher $\ell$, albeit with the number of required FFTs increasing substantially.

The main motivation for the derivation which led to the preceding equations was that of being able to compute them using FFTs. It is easy to see that these quantities will therefore be subject to aliasing, and one must correct for this effect. In section (3.2.1) we saw that by interpolating the particles onto two grids of densities, one displaced by half a cell size from the other to obtain $\delta_1^G$ and $\delta_2^G$ one could then obtain a density field with reduced effects of aliasing in Fourier space

$$\delta^G(\boldsymbol{k}) = \frac{1}{2}\left(\delta_1^G(\boldsymbol{k}) + \delta_2^G(\boldsymbol{k})\right). \tag{3.44}$$

An apparent difficulty is that this quantity is in Fourier space, and we need it in real space to use equation (3.43) and compute the multipoles; the solution to this is very simple in fact: one simply takes the inverse Fourier transform of $\delta^G(\boldsymbol{k})$ to obtain $\delta^G(\boldsymbol{x})$. This guarantees that when we do take the Fourier transform to obtain the $Q_{ij}(\boldsymbol{k})$ this will be the convolution of a number of functions with the aliasing reduced density in Fourier space, therefore preserving its desired property.

The substitution $\boldsymbol{x} \to \boldsymbol{x}_1$ can also be viewed as choosing the position of one of the galaxies in a pair as the line of sight connecting it to the observer, known as the end-point line of sight. Figure (3.3) illustrates other possible definitions of the line of sight such as the mean or angular bisector; these have the advantage of being unchanged by exchanging

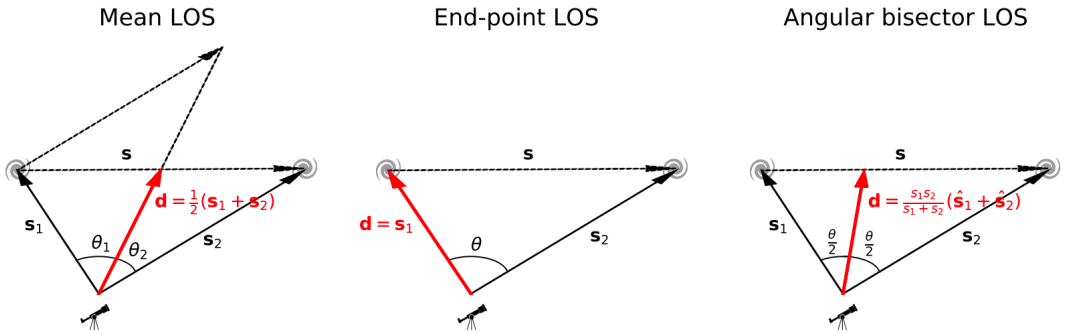


**Figure 3.3:** The computation of power spectrum multipoles requires the definition of a line-of-sight vector connecting the observer to the pairs of tracers. Three possible definitions are shown in this figure; the mean and angular bisector LOS have the advantage of being symmetric with respect to the exchange $1 \leftrightarrow 2$. Extracted from (Beutler, Castorina, and Zhang, 2019).

$s_1 \leftrightarrow s_2$. The end-point LOS represents an improvement over the plane-parallel approximation, but still introduces systematic effects when computing correlations of objects separated by very wide angles, which are further mitigated by the two other definitions, at the cost of increased computational requirements.

## 3.4 Power-Spectrum Estimators

In the previous sections of this chapter, we have dealt with the issues of measuring unbiased spectra from a certain dataset. Here, we wish to focus on another, equally important, aspect of power spectrum estimation: optimizing the amount of information extracted from a certain dataset. The main intuition behind this is that certain parts of an observed region will be more densely populated than others, and will thus dominate a naive estimation of the power spectrum, which weighs all galaxies equally; this may not be optimal because the error on large scales will be dominated by the few large scale modes available to average over, and giving excess weight to dense regions is similar to restricting the effective volume probed by the survey. One could benefit greatly, simply from giving weights to these galaxies which are inversely proportional to the number density at that region, so that all regions, regardless of being more or less populated, would give essentially the same contribution, thus maximizing the effective volume of the survey.

To understand what is an optimal estimator of a quantity we must introduce the

concept of the Fisher Matrix. In the field of Bayesian Statistics, the likelihood function plays a very important role. Let us remind ourselves that Bayes' theorem says that

$$P(D|\mathbf{\Theta})P(\mathbf{\Theta}) = P(\mathbf{\Theta}|D)P(D) \tag{3.45}$$

and that $P(D|\mathbf{\Theta})$ is the likelihood, $P(D)$ is the evidence, $P(\mathbf{\Theta})$ is the prior, and $P(\mathbf{\Theta}|D)$ is the posterior. It is clear why one would be most interested in the posterior: it is precisely the probability that a model is correct, given we measured some dataset $D$. However, when performing theoretical analyses, one generally ignores the prior and the evidence, so that the posterior has essentially the same meaning as the likelihood.

Say we have a dataset $\{x_n\}$ and a theory capable of predicting expected values for these measurements, given a set of parameters $\mathbf{\Theta}$. The values of $\mathbf{\Theta}$ which will best describe this dataset are those which maximize the likelihood function, and we can define confidence levels as regions internal to hypersurfaces of constant likelihood, allowing us to define the errors in the estimates of the parameters. In practical cases of cosmology, $\{x_n\}$ will be a tremendously large amount of data and $\mathbf{\Theta}$ will be a vector with dozens of parameters, so that the simple problem of evaluating the likelihood in a grid of points becomes extremely computationally expensive. The route which is usually taken then is to run a Markov-Chain Monte-Carlo (MCMC) algorithm in order to explore this parameter space in an optimized fashion. However, it is also useful to discuss an approximation capable of reducing the complexity of this problem, since it has some very useful theoretical applications.

The approximation which we will make is nothing but a Taylor expansion of the logarithm of the likelihood function around the maximum-likelihood point $\hat{\mathbf{\Theta}}$

$$\begin{aligned}\ln(\mathcal{L}) = \ln\mathcal{L}(\hat{\Theta}) + \cancelto{0}{\left.\frac{\partial \ln\mathcal{L}}{\partial\Theta_i}\right|_{\Theta=\hat{\Theta}}}(\Theta_i - \hat{\Theta}_i) \\ + \left.\frac{\partial^2 \ln\mathcal{L}}{\partial\Theta_i\partial\Theta_j}\right|_{\mathbf{\Theta}=\hat{\mathbf{\Theta}}}(\Theta_i - \hat{\Theta}_i)(\Theta_j - \hat{\Theta}_j)\end{aligned} \tag{3.46}$$

then we can take the exponential on both sides, obtaining

$$\mathcal{L} \propto N \exp\left[-\frac{1}{2}(\Theta_i - \hat{\Theta}_i)F_{ij}(\Theta_j - \hat{\Theta}_j)\right] \tag{3.47}$$

and $F_{ij}$ is precisely the Fisher Matrix

$$F_{ij} = -\left\langle \frac{\partial^2 \ln \mathcal{L}}{\partial\Theta_i \partial\Theta_j} \right\rangle \Bigg|_{\boldsymbol{\Theta}=\hat{\boldsymbol{\Theta}}}. \tag{3.48}$$

Sometimes this is called the Fisher Information Matrix, since it gives us a measure of the amount of information we are able to obtain regarding the parameters $\Theta_i$ and $\Theta_j$. Indeed, it is given by the second derivative of the log-Likelihood, which tells us what is the value of the curvature of this function at the maximum likelihood point: if the curvature is large then the likelihood function falls quickly when distancing from $\hat{\Theta}$ meaning we have a stringent constraint on the parameters; if the curvature is small then the likelihood falls more slowly, meaning we have weaker constraints on the parameters.

### 3.4.1 Cramér-Rao Lower Bound

Now that we have introduced the Fisher Matrix we can enunciate a statistical theorem which has great importance in cosmology, the Cramér-Rao Inequality. This result tells us that the variance of an unbiased estimator can never be smaller than $(F^{-1})_{ii}$. In a certain way, $\boldsymbol{F}^{-1}$ is the optimal covariance matrix that an experiment can produce.

We shall use this result to characterize optimal estimators. Let us say we obtain, through some method, estimates $q_i$ of the spectrum in bins of $k$, then this method will be optimal if it saturates the Crámer-Rao inequality, that is

$$\mathrm{Cov}(q_i, q_j) = F_{ij}^{-1}. \tag{3.49}$$

### 3.4.2 Quadratic Estimators

Now we face ourselves with the problem of constructing estimators which satisfy this condition. Fortunately, Tegmark et al., 1998 devised a method to systematically find

such estimators, which we shall describe below.

Let us suppose we have a data set $d_i$ and for simplicity we assume that $\langle d_i \rangle = 0$. We would like to extract from it estimates $p_i$ of the power spectrum in each band of $k$. Then we begin the procedure of building the estimators of the spectrum by creating the quadratic form:

$$\hat{q}_\mu \equiv E_\mu^{ij} d_i d_j - \Delta_\mu \tag{3.50}$$

in which

$$\begin{cases} E_\mu^{ij} & = C_{il}^{-1} C_{lm,\mu} C_{mj}^{-1} \\ C_{ij} & = \langle d_i d_j \rangle \\ C_{ij,\mu} & = \frac{\partial C_{ij}}{\partial P(\mathbf{k}_\mu)} \end{cases} \tag{3.51}$$

and $\Delta_\mu$ is a term to subtract any possible bias, so to result an unbiased estimator. This is an educated guess, made by Tegmark et al., 1998; as we will demonstrate, this is indeed an optimal estimator, and further ahead we will give some intuition as to why this is the correct answer, in the more specific context of the FKP estimator. For now, we will focus on demonstrating that this indeed satisfies the Cramér-Rao lower bound.

It can be readily seen that:

$$\begin{aligned} \langle \hat{q}_\mu \rangle &= \langle E_\mu^{ij} d_i d_j \rangle - \langle \Delta_\mu \rangle \\ &= \frac{1}{2} \langle d_i d_j \rangle C_{il}^{-1} C_{lm,\mu} C_{mj}^{-1} - \langle \Delta_\mu \rangle \\ &= \frac{1}{2} \underbrace{C_{ij} C_{il}^{-1}}_{\delta_{jl}} C_{lm,\mu} C_{mj}^{-1} - \langle \Delta_\mu \rangle \\ &= \frac{1}{2} \operatorname{Tr} \left[ \boldsymbol{C}_{,\mu} \boldsymbol{C}^{-1} \right] - \langle \Delta_\mu \rangle \end{aligned} \tag{3.52}$$

and this can be used to calculate the covariance matrix

$$\begin{aligned} Cov(\hat{q}_\mu, \hat{q}_\nu) &= \langle \left( E_\mu^{ij} d_i d_j - \Delta_\mu \right) \left( E_\nu^{lm} d_l d_m - \Delta_\nu \right) \rangle - \langle \left( E_\mu^{ij} d_i d_j - \Delta_\mu \right) \rangle \langle \left( E_\nu^{lm} d_l d_m - \Delta_\nu \right) \rangle \\ &= \text{Term}_1 + \text{Term}_2. \end{aligned} \tag{3.53}$$

Take the first term on the RHS of equation (3.53)

$$\text{Term}_1 = E^{ij}_{\mu} E^{lm}_{\nu} \langle d_i d_j d_l d_m \rangle - E^{ij}_{\mu} \Delta_{\nu} \langle d_i d_j \rangle - E^{lm}_{\nu} \Delta_{\mu} \langle d_l d_m \rangle + \Delta_{\mu} \Delta_{\nu}, \tag{3.54}$$

now assuming that the data are distributed according to a Gaussian we obtain

$$\langle d_i d_j d_l d_m \rangle = C_{ij} C_{lm} + C_{il} C_{jm} + C_{im} C_{jl}, \tag{3.55}$$

then substituting this into equation (3.54) we obtain

$$\begin{aligned} \text{Term}_1 = & \frac{1}{4} C^{-1}_{ia} C_{ab,\mu} C^{-1}_{bj} C^{-1}_{lc} C_{cd,\nu} C^{-1}_{dm} \times (C_{ij} C_{lm} + C_{il} C_{jm} + C_{im} C_{jl}) \\ & - \frac{1}{2} \operatorname{Tr}\left[ \boldsymbol{C}_{,\mu} \boldsymbol{C}^{-1} \right] \Delta_{\nu} - \frac{1}{2} \operatorname{Tr}\left[ \boldsymbol{C}_{,\nu} \boldsymbol{C}^{-1} \right] \Delta_{\mu} + \Delta_{\mu} \Delta_{\nu}, \end{aligned} \tag{3.56}$$

which simplifies into

$$\begin{aligned} \text{Term}_1 = & \frac{1}{4} \operatorname{Tr}\left[ \boldsymbol{C}_{,\mu} \boldsymbol{C}^{-1} \right] \operatorname{Tr}\left[ \boldsymbol{C}_{,\nu} \boldsymbol{C}^{-1} \right] + \frac{1}{2} \operatorname{Tr}\left[ \boldsymbol{C}^{-1} \boldsymbol{C}_{,\mu} \boldsymbol{C}^{-1} \boldsymbol{C}_{,\nu} \right] \\ & - \frac{1}{2} \operatorname{Tr}\left[ \boldsymbol{C}_{,\mu} \boldsymbol{C}^{-1} \right] \Delta_{\nu} - \frac{1}{2} \operatorname{Tr}\left[ \boldsymbol{C}_{,\nu} \boldsymbol{C}^{-1} \right] \Delta_{\mu} + \Delta_{\mu} \Delta_{\nu}. \end{aligned} \tag{3.57}$$

Term 2 on the other hand gives us

$$\text{Term}_2 = -\frac{1}{4} \operatorname{Tr}\left[ \boldsymbol{C}_{,\mu} \boldsymbol{C}^{-1} \right] \operatorname{Tr}\left[ \boldsymbol{C}_{,\nu} \boldsymbol{C}^{-1} \right] + \frac{1}{2} \operatorname{Tr}\left[ \boldsymbol{C}_{,\mu} \boldsymbol{C}^{-1} \right] \Delta_{\nu} + \frac{1}{2} \operatorname{Tr}\left[ \boldsymbol{C}_{,\nu} \boldsymbol{C}^{-1} \right] \Delta_{\mu} - \Delta_{\mu} \Delta_{\nu} \tag{3.58}$$

so that by inspection many terms cancel, and the covariance gives

$$\text{Cov}(\hat{q}_{\mu}, \hat{q}_{\nu}) = \frac{1}{2} \operatorname{Tr}\left[ \boldsymbol{C}^{-1} \boldsymbol{C}_{,\mu} \boldsymbol{C}^{-1} \boldsymbol{C}_{,\nu} \right]. \tag{3.59}$$

Now that we have the covariance matrix, we must find an expression for the Fisher matrix, in order to compare them. Let us suppose that the likelihood function for our data

is given by a multivariate Gaussian

$$\begin{aligned}\mathcal{L} =& \frac{1}{\sqrt{(2\pi)^n \det\{\boldsymbol{C}\}}} \\ & \exp\left\{-\frac{1}{2}(d_i - \langle d_i \rangle) C_{ij}^{-1} (d_j - \langle d_j \rangle)\right\},\end{aligned} \tag{3.60}$$

then using the identity $\ln[\det(\boldsymbol{C})] = \mathrm{Tr}[\ln(\boldsymbol{C})]$ and defining the data matrix $D_{ij} \equiv (d_i - \langle d_i \rangle)(d_j - \langle d_j \rangle)$ we can write

$$\ln \mathcal{L} = -\frac{n}{2}\ln(2\pi) - \frac{1}{2}\,\mathrm{Tr}\big\{\ln(\boldsymbol{C}) + \boldsymbol{C}^{-1}\boldsymbol{D}\big\} \tag{3.61}$$

and taking derivatives with respect to $p_\mu$ and $p_\nu$ we obtain

$$\frac{\partial \ln \mathcal{L}}{\partial p_\mu} = -\frac{1}{2}\,\mathrm{Tr}\big\{\boldsymbol{C}^{-1}\boldsymbol{C}_{,\mu} + \boldsymbol{C}^{-1}\boldsymbol{D}_{,\mu} - \boldsymbol{C}^{-1}\boldsymbol{C}_{,\mu}\boldsymbol{C}^{-1}\boldsymbol{D}\big\} \tag{3.62}$$

$$\begin{aligned}\frac{\partial^2 \ln \mathcal{L}}{\partial p_\mu \partial p_\nu} =& -\frac{1}{2}\,\mathrm{Tr}\Big[ - \boldsymbol{C}^{-1}\boldsymbol{C}_{,\nu}\boldsymbol{C}^{-1}\boldsymbol{C}_{,\mu} + \boldsymbol{C}^{-1}\boldsymbol{C}_{,\mu\nu} + \boldsymbol{C}^{-1}\big(\boldsymbol{C}_{,\nu}\boldsymbol{C}^{-1}\boldsymbol{C}_{,\mu} + \boldsymbol{C}_{,\mu}\boldsymbol{C}^{-1}\boldsymbol{C}_{,\nu}\big)\boldsymbol{C}^{-1}\boldsymbol{D} \\ & - \boldsymbol{C}^{-1}\big(\boldsymbol{C}_{,\nu}\boldsymbol{C}^{-1}\boldsymbol{D}_{,\mu} + \boldsymbol{C}_{,\mu}\boldsymbol{C}^{-1}\boldsymbol{D}_{,\nu}\big) + \boldsymbol{C}^{-1}\boldsymbol{D}_{\mu\nu} - \boldsymbol{C}^{-1}\boldsymbol{C}_{,\mu\nu}\boldsymbol{C}^{-1}\boldsymbol{D}\Big],\end{aligned} \tag{3.63}$$

then taking the expected value of this expression, and using that[2]

$$\begin{cases} \big\langle \boldsymbol{D} \big\rangle & = \boldsymbol{C} \\ \big\langle \boldsymbol{D}_{,\mu} \big\rangle & = 0 \\ \big\langle \boldsymbol{D}_{,\mu\nu} \big\rangle & = 0 \end{cases} \tag{3.64}$$

we obtain the desired expression

$$\left\langle \frac{\partial^2 \ln \mathcal{L}}{\partial p_\mu \partial p_\nu} \right\rangle = \frac{1}{2}\,\mathrm{Tr}\left[\boldsymbol{C}^{-1}\boldsymbol{C}_{,\mu}\boldsymbol{C}^{-1}\boldsymbol{C}_{,\nu}\right] \tag{3.65}$$

[2]This can be demonstrated by using the definition for $D$, and the fact that the derivatives of the data vectors themselves will be null $d_{i,j} = 0$.

clearly implying that

$$\boldsymbol{F}_{\mu\nu} = -\frac{1}{2}\,\mathrm{Tr}\{\boldsymbol{C}^{-1}\boldsymbol{C}_{,\mu}\boldsymbol{C}^{-1}\boldsymbol{C}_{,\nu}\}. \tag{3.66}$$

Comparing equations (3.53) and (3.66) makes it clear that

$$\mathrm{Cov}(\hat{q}_\mu, \hat{q}_\nu) = F_{\mu\nu}. \tag{3.67}$$

As a last step of this construction we will define $\hat{p}_\mu \equiv F^{-1}_{\mu\nu}\hat{q}_\nu$ and it is easy to see it will satisfy

$$\mathrm{Cov}(\hat{p}_\mu, \hat{p}_\nu) = F^{-1}_{\mu\nu}. \tag{3.68}$$

Finally with the definition

$$\Delta_\mu = \frac{1}{2}\,\mathrm{Tr}\left[\boldsymbol{C}^{-1}\boldsymbol{C}_{,\mu}\right] - F_{\mu\nu}\bar{p}_\nu \tag{3.69}$$

we see that the expected value of $\hat{p}_\mu$ becomes

$$\begin{aligned}\langle\hat{p}_\mu\rangle &= \frac{1}{2}F^{-1}_{\mu\nu}\,\mathrm{Tr}\left[\boldsymbol{C}_{,\nu}\boldsymbol{C}^{-1}\right] - \frac{1}{2}F^{-1}_{\mu\nu}\,\mathrm{Tr}\left[\boldsymbol{C}_{,\nu}\boldsymbol{C}^{-1}\right] + F^{-1}_{\mu\nu}F_{\nu\alpha}\bar{p}_\alpha \\ &= \bar{p}_\mu.\end{aligned} \tag{3.70}$$

Therefore, we have demonstrated one way to build an unbiased and optimal estimator.

### 3.4.3 FKP

The result obtained by (Feldman, Kaiser, and Peacock, 1994) can be obtained in a simpler form simply by applying the quadratic method and performing a couple of approximations, which is what we will do next, following closely what was done in (Tegmark et al., 1998). Rewriting equation (3.50) in the limit of the continuous gives

$$\hat{q}_\mu = \int d^3x \int d^3x'\delta(\boldsymbol{x})E_\mu(\boldsymbol{x},\boldsymbol{x}')\delta(\boldsymbol{x}') - \Delta_\mu \tag{3.71}$$

in which $\Delta_\mu$ is given by

$$\Delta_\mu = \frac{1}{2}\int d^3x \int d^3y C^{-1}(\boldsymbol{x},\boldsymbol{y})\frac{\partial C(\boldsymbol{x},\boldsymbol{y})}{\partial p_\mu} - F_{\mu\nu}p_\nu \tag{3.72}$$

and the weighting function is given by

$$E_\mu(\boldsymbol{x},\boldsymbol{x}') = \frac{1}{2}\int d^3y \int d^3y' C^{-1}(\boldsymbol{x},\boldsymbol{y})\frac{\partial C(\boldsymbol{y},\boldsymbol{y}')}{\partial p_\mu}C^{-1}(\boldsymbol{y}',\boldsymbol{x}'). \tag{3.73}$$

It is clear then that this calculation cannot proceed while we do not know how to calculate terms such as $C^{-1}(\boldsymbol{x},\boldsymbol{x}')$ and $C_{,\mu}(\boldsymbol{x},\boldsymbol{x}')$. We can begin by remembering that

$$\begin{aligned} C(\boldsymbol{x},\boldsymbol{x}') &= \mathrm{Cov}(\delta(\boldsymbol{x}),\delta(\boldsymbol{x}')) \\ &= b^2\xi_m(\boldsymbol{x}-\boldsymbol{x}') + \frac{\delta^D(\boldsymbol{x}-\boldsymbol{x}')}{\bar{n}} \\ &= \int \frac{d^3k}{(2\pi)^3} e^{-i\boldsymbol{k}.(\boldsymbol{x}-\boldsymbol{x}')}\left[b^2P_m(\boldsymbol{k}) + \frac{1}{\bar{n}}\right]. \end{aligned} \tag{3.74}$$

Therefore, using that $\delta P(\boldsymbol{k})/\delta P(\boldsymbol{k}_\mu) = (2\pi)^3\delta^D(\boldsymbol{k}-\boldsymbol{k}_\mu)$ one obtains

$$\begin{aligned} C_{,\mu} &= \int \frac{d^3k}{(2\pi)^3} e^{-i\boldsymbol{k}.(\boldsymbol{x}-\boldsymbol{x}')}(2\pi)^3\delta^D(\boldsymbol{k}-\boldsymbol{k}_\mu) \\ &= e^{-i\boldsymbol{k}_\mu.(\boldsymbol{x}-\boldsymbol{x}')} \end{aligned} \tag{3.75}$$

and analyzing equation (3.74) in more detail we can see that in the limit where $|\boldsymbol{x}-\boldsymbol{x}'|$ is much larger than $L$, a typical scale over which the spectrum changes considerably, the exponential term oscillates very rapidly while the spectrum remains practically unchanged, so the latter can be considered constant and taken out of the integral

$$C(\boldsymbol{x},\boldsymbol{x}') = \left[b^2P_m + \frac{1}{\bar{n}}\right]\delta^D(\boldsymbol{x}-\boldsymbol{x}'), \tag{3.76}$$

and the inverse of this is given by

$$C^{-1}(\boldsymbol{x},\boldsymbol{x}') = \left[\frac{\bar{n}}{1+\bar{n}b^2P_m}\right]\delta^D(\boldsymbol{x}-\boldsymbol{x}'). \tag{3.77}$$

At last, substituting (3.77) and (3.75) into (3.73) gives

$$E_\mu = \frac{1}{2}\int d^3y \int d^3y' \left[\frac{\bar{n}}{1+\bar{n}b^2P_m}\right]\delta^D(\boldsymbol{x}-\boldsymbol{y})e^{-i\boldsymbol{k}_\mu.(\boldsymbol{y}-\boldsymbol{y}')}\left[\frac{\bar{n}}{1+\bar{n}b^2P_m}\right]\delta^D(\boldsymbol{y}'-\boldsymbol{x}') \tag{3.78}$$

and substituting this into (3.71) we get

$$\begin{aligned}\hat{q}_\mu &= \frac{1}{2}\left[\int d^3y\left(\frac{\delta(\boldsymbol{y})\bar{n}(\boldsymbol{y})}{1+\bar{n}b^2P_m}\right)e^{-i\boldsymbol{k}_\mu\cdot\boldsymbol{y}}\right]\left[\int d^3y'\left(\frac{\delta(\boldsymbol{y}')\bar{n}(\boldsymbol{y}')}{1+\bar{n}b^2P_m}\right)e^{i\boldsymbol{k}_\mu\cdot\boldsymbol{y}'}\right] \\ &= \frac{1}{2}F(\boldsymbol{k}_\mu)F^*(\boldsymbol{k}_\mu),\end{aligned} \tag{3.79}$$

in which $F(\boldsymbol{k}_\mu)$ is defined by

$$\begin{aligned}F(\boldsymbol{k}_\mu) =& \int d^3y w_{\text{FKP}}(\boldsymbol{y})\bar{n}(\boldsymbol{y})\delta(\boldsymbol{y})e^{-i\boldsymbol{k}_\mu\boldsymbol{y}} \\ w_{\text{FKP}}(\boldsymbol{y}) =& \frac{1}{1+\bar{n}b^2P_m}\end{aligned} \tag{3.80}$$

precisely the FKP prescription, except for a factor of $1/2$, which has no importance, affecting only the normalisation. Here we have neglected the term $\Delta_\mu$ since the presence of this term would complicate significantly the math without providing any insight.

Now let us substitute our results for $\boldsymbol{C}^{-1}$ and $\boldsymbol{C}_{,\mu}$ into equation (3.59), resulting in

$$\text{Cov}(\hat{q}_\mu,\hat{q}_\nu) = \frac{1}{2}\int d^3x\int d^3y\left[\frac{\bar{n}(\boldsymbol{x})}{1+\bar{n}b^2P_m}\right]\left[\frac{\bar{n}(\boldsymbol{y})}{1+\bar{n}b^2P_m}\right]e^{i(\boldsymbol{k}_\mu-\boldsymbol{k}_\nu)\cdot(\boldsymbol{x}-\boldsymbol{y})}. \tag{3.81}$$

Now averaging this over a shell in $\boldsymbol{k}$-space

$$(\Delta q_i)^2 = \frac{1}{2V_s^2}\int\frac{d^3k_\mu}{(2\pi)^3}\int\frac{d^3k_\nu}{(2\pi)^3}\int d^3x\int d^3y\left[\frac{\bar{n}(\boldsymbol{x})}{1+\bar{n}b^2P_m}\right]\left[\frac{\bar{n}(\boldsymbol{y})}{1+\bar{n}b^2P_m}\right]e^{i(\boldsymbol{k}_\mu-\boldsymbol{k}_\nu)\cdot(\boldsymbol{x}-\boldsymbol{y})}. \tag{3.82}$$

then applying the stationary phase approximation $e^{i(\boldsymbol{k}_\mu-\boldsymbol{k}_\nu)\cdot(\boldsymbol{x}-\boldsymbol{y})}\to(2\pi)^3\delta^D(\boldsymbol{k}_\mu-\boldsymbol{k}_\nu)\delta^D(\boldsymbol{x}-\boldsymbol{y})$ gives the following expression for the variance of the band-power estimate

$$(\Delta q_i)^2 = \frac{1}{2V_s}\int\left[\frac{\bar{n}(\boldsymbol{x})}{1+\bar{n}b^2P_m}\right]^2 d^3x. \tag{3.83}$$

Now introducing the notation $\phi(\boldsymbol{x}) = \bar{n}(\boldsymbol{x})/(1+\bar{n}b^2P_m)$ we can write

$$\begin{aligned}\langle q_\mu \rangle =& \left\langle \frac{1}{2}\int d^3y d^3y' \delta(\boldsymbol{y})\phi(\boldsymbol{y})\delta(\boldsymbol{y'})\phi(\boldsymbol{y'})e^{-i\boldsymbol{k}_\mu(\boldsymbol{y'}-\boldsymbol{y})} \right\rangle \\ &= \frac{1}{2}\int \frac{d^3k_\nu}{(2\pi)^3}\int d^3y d^3y' \phi(\boldsymbol{y})\phi(\boldsymbol{y'})e^{i(\boldsymbol{k}_\nu-\boldsymbol{k}_\mu)\cdot(\boldsymbol{y'}-\boldsymbol{y})}P(\boldsymbol{k}_\nu) \\ &\approx \frac{1}{2}\int d^3y \phi(\boldsymbol{y})^2 b^2 P_m(\boldsymbol{k}_\mu)\end{aligned} \tag{3.84}$$

and averaging this over a shell in $\boldsymbol{k}$-space

$$\langle q_i \rangle = \frac{1}{2}b^2P_m(k_i)\int d^3y \phi^2(\boldsymbol{y}) \tag{3.85}$$

and therefore, the relative variance is given by

$$\begin{aligned}\left(\frac{\Delta q_i}{\langle q_i \rangle}\right)^2 &= \left(\frac{4\int d^3x\phi^2(\boldsymbol{x})}{2V_s b^4 P_m^2 \left(\int d^3x \phi^2(\boldsymbol{x})\right)^2}\right) \\ &= \frac{2}{V_s V_{eff}}\end{aligned} \tag{3.86}$$

in which

$$V_{eff} = \int d^3x \left[\frac{\bar{n}(\boldsymbol{x})b^2P_m}{1+\bar{n}b^2P_m}\right]^2 \tag{3.87}$$

as stated in the FKP paper. This shows that FKP is indeed in this limit an optimal estimator of the spectrum. We did not demonstrate here that it is also unbiased, but in the implementation we do subtract the shot noise bias, ensuring it is.

Notice how the FKP estimator agrees with the intuition we mentioned at the beginning of this section, regarding why one would need weighting schemes to optimally extract information. Indeed, for regions with a great number of galaxies, this weight will asymptotically go to $\frac{1}{\bar{n}}$, thus giving equal weights to volumes which are equally dense, in order to maximize the effective volume probed by the survey; on the other hand, when we have a very small number of objects, the weights will go to 1, weighting all galaxies equally, since in these regions it is the shot-noise which dominates the error, and to reduce it we must have the largest possible number of objects.

### 3.4.4 MTOE

The derivation of the Multi-Tracer Optimal Estimator is quite similar to the one presented in the previous section, but more involved, due to the presence of multiple tracers of the density field. We refer the interested reader to the following series of papers, which explain this method in great detail: (Abramo, 2012; Abramo and Leonard, 2013; Abramo, Secco, and Loureiro, 2015).

## 3.5 Numerical Implementation

In this section we give an overview of how these estimators are effectively implemented in our codes to compute the monopole and quadrupole of the power spectra.

### 3.5.1 FKP

We begin by defining several quantities which will be necessary in the following explanations.

- $n_g^{(1)}, n_g^{(2)} \rightarrow$ Density grids of objects for which one wants to estimate the spectrum. The two grids are for the same set of objects but for one of them we displace the objects by half a cell size, to combine them in the interlacing procedure;
- $n_r^{(1)}, n_r^{(2)} \rightarrow$ Density grids of randoms. They must have the same radial distribution as $n_g$, and be subject to the same mask;
- $\alpha \rightarrow \sum_i n_g / \sum_i n_r$;
- $P_0 \rightarrow$ Typical power spectrum value;
- $b \rightarrow$ Guess of bias value;

From these quantities we begin by defining

$$w_{\text{FKP}}^{(n)}(\boldsymbol{r}) = \frac{b^2 P_0}{1 + \alpha n_r^{(n)} b^2 P_0} \tag{3.88}$$

$$F^{(n)}(\boldsymbol{r}) = \frac{w_{\text{FKP}}^{(n)}(\boldsymbol{r})}{N^{(n)}} \left[ n_g^{(n)}(\boldsymbol{r}) - \alpha n_r^{(n)}(\boldsymbol{r}) \right] \tag{3.89}$$

in which $N^{(n)} = \sqrt{\sum_i \left[\alpha n_r^{(n)}(\boldsymbol{r}_i)\right]^2 \left[w_{\rm FKP}^{(n)}(\boldsymbol{r}_i)\right]^2}$ and from this, taking their Fourier transforms, we obtain

$$F^{(n)}(\boldsymbol{k}) = \text{ FFT}\left[F^{(n)}(\boldsymbol{r})\right]. \tag{3.90}$$

We combine these two Fourier transforms, averaging them to reduce the aliasing effects, and divide them by the MAS window function,

$$F(\boldsymbol{k}) = \frac{1}{2}\left(F^{(1)}(\boldsymbol{k}) + F^{(2)}(\boldsymbol{k})\right)/|W(\boldsymbol{k})|^2 \tag{3.91}$$

and then take the inverse Fourier transform, to obtain the corrected $F(\boldsymbol{r})$

$$F(\boldsymbol{r}) = \text{ FFT}^{-1}\left[F(\boldsymbol{k})\right]. \tag{3.92}$$

In general we will have several tracers of the underlying dark-matter density field, and will want to compute not only their individual auto power-spectra, but also the cross spectra between distinct tracers. Therefore, we perform the procedure described above for each of the tracers, $\mu$, and from now on we index the quantities with this marker as well; it should be noted as well, that, whenever $N_\mu$, or $w_{\text{FKP},\mu}$ appear again we will use the value of the $^{(1)}$ grid, but will omit this index,

$$\begin{aligned}
F_{0,\mu}(\boldsymbol{k}) &= \text{FFT}\left[F_\mu(\boldsymbol{r})\right] \\
F_{ij,\mu}(\boldsymbol{k}) &= \text{FFT}\left[\hat{\boldsymbol{r}}_i\hat{\boldsymbol{r}}_j F_\mu(\boldsymbol{r})\right] \\
F_{2,\mu}(\boldsymbol{k}) &= 3\hat{\boldsymbol{k}}_i\hat{\boldsymbol{k}}_j F_{ij,\mu}(\boldsymbol{k}) - F_{0,\mu}(\boldsymbol{k}) \\
P_{SN,\mu}(k) &= \frac{1+\alpha_\mu}{N_\mu^2}\sum_i \frac{w_{\text{FKP},\mu}^2(\boldsymbol{r}_i)}{b_\mu^2},
\end{aligned} \tag{3.93}$$

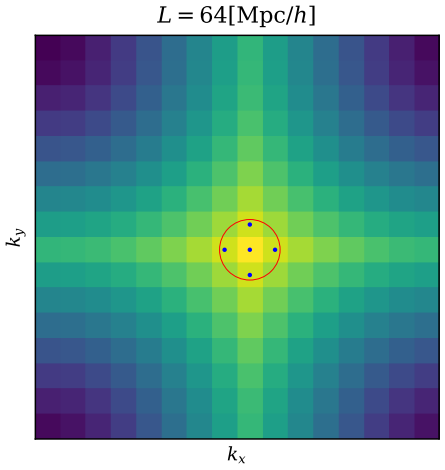


**Figure 3.4:** Grid in Fourier space, obtained from a box with side $L = 64[\text{Mpc}/h]$ and cell size $H = 4[\text{Mpc}/h]$. The red line represents a circle of radius $r = 0.12[h/\text{Mpc}]$. One can see how very few modes are available for averaging.

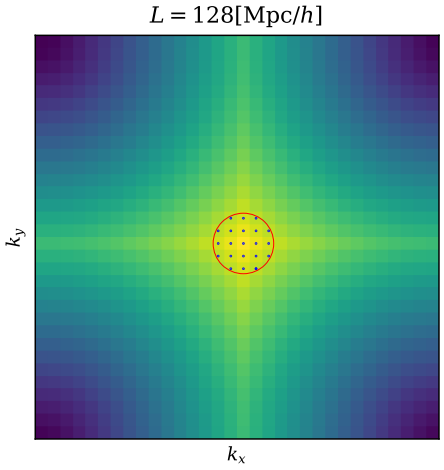


**Figure 3.5:** Grid in Fourier space, obtained from a box with side $L = 128[\text{Mpc}/h]$ and cell size $H = 4[\text{Mpc}/h]$. The red circle has radius $r = 0.12[h/\text{Mpc}]$. It is not hard to see that by increasing $L$ we have increased the precision of the calculations.

and from these definitions we can thus write the estimators for the monopole and quadrupole, namely

$$\begin{aligned} P_{0,\mu}(k_i) =& H^3 \left[ \frac{1}{N_{k_i}} \sum_{\boldsymbol{k} \in V_s(k_i)} F_{0,\mu}(\boldsymbol{k}) F^*_{0,\mu}(\boldsymbol{k}) - P_{SN,\mu} \right] \\ P_{2,\mu}(k_i) =& H^3 \, \text{Re} \left[ \frac{1}{N_{k_i}} \sum_{\boldsymbol{k} \in V_s(k_i)} F_{0,\mu}(\boldsymbol{k}) F^*_{2,\mu}(\boldsymbol{k}) \right] \end{aligned} \tag{3.94}$$

$$\begin{aligned} P_{0,\mu\nu}(k_i) =& H^3 \, \text{Re} \left[ \frac{1}{N_{k_i}} \sum_{\boldsymbol{k} \in V_s(k_i)} F_{0,\mu}(\boldsymbol{k}) F^*_{0,\nu}(\boldsymbol{k}) \right] \\ P_{2,\mu\nu}(k_i) =& \frac{H^3}{2} \, \text{Re} \left[ \frac{1}{N_{k_i}} \sum_{\boldsymbol{k} \in V_s(k_i)} \left( F^*_{0,\mu}(\boldsymbol{k}) F_{2,\nu}(\boldsymbol{k}) + F^*_{2,\mu}(\boldsymbol{k}) F_{0,\nu}(\boldsymbol{k}) \right) \right], \end{aligned} \tag{3.95}$$

in which $V_s(k_i)$ is a spherical shell of radius $k_i$, and $N_{k_i}$ is the number of modes which fall inside it.

### 3.5.2 Resolution Effects

Here we comment on a numerical effect which does not seem obvious at first, but can have extreme effects, mainly for the computation of higher order multipoles. Since the power spectra are computed in Fourier spectra, the cell size in real space controls the maximum wave-number to which we have access, i.e. the Nyquist frequency $k_{\rm Nyq} = \pi/H$, and the size of the box containing the data is what controls the smallest wave-number which we can access, $k_{\rm Min} = 2\pi/L$. The estimation of power-spectrum multipoles involves integrations over angular coordinates, and therefore, if one uses a small box size – regardless of the volume of the observed data – this integration may be plagued by errors due to lack of numerical resolution in Fourier space. This is illustrated in figures (3.4, 3.5); in the left panel we see the Fourier transform of a density field contained in a cubic box of size $L = 64{\rm Mpc}/h$, and in the right panel we see the Fourier transform of the same density field, with the same cell size, but contained in a cubic box of size $L = 128{\rm Mpc}/h$. It is not hard to see that the Fourier grid created from the larger box has a much finer resolutions, which would allow for much more precise calculations.

### 3.5.3 Binning effects

In the estimation of power spectra, one of the final steps is to take the power spectrum computed over a Fourier grid, $P(\boldsymbol{k})$, and average its values for the wavemodes that fall inside a spherical shell of radius $k_i$, to obtain an estimate of $P(k_i)$, i.e.

$$P(k_i) = \frac{1}{N_{k_i}} \sum_{\boldsymbol{k} \in V_s(k_i)} P(\boldsymbol{k}). \tag{3.96}$$

If these spherical shells are too thick, we will be averaging over power spectra at many different values of $k$; this is an issue because the number of modes contributing at a certain $k$ will decrease as $k$ becomes smaller, and therefore, this average will privilege higher values of $k$, introducing small distortions in the value of the bin-averaged spectra. In the case of the matter power spectrum for scales $k > 10^{-2}$ it has a negative derivative, and therefore, its value will be systematically below what is expected, due to this effect, as can be seen in figure (3.6).

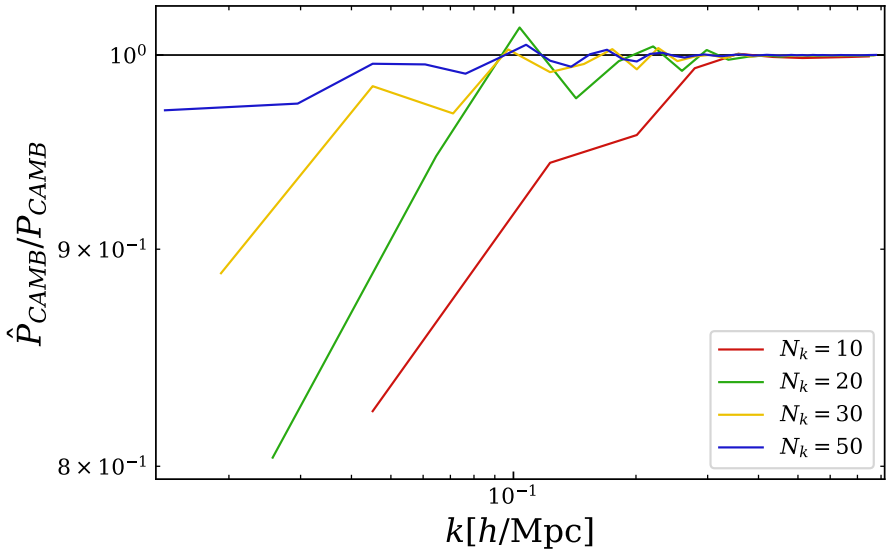


**Figure 3.6:** Comparison of the power spectra estimated from a Fourier grid, to its actual value. The label indicates the number of $k$ bins over which we average this spectrum. One can see that the distortions are most severe at low $k$, and that they decrease substantially if one increases the number of points at which we wish to evaluate this spectrum.

Fortunately, it is very easy to correct for this kind of effect; we suppose that the damping of the spectrum due to the binning process does not depend strongly on cosmology, so that one can choose a certain fiducial cosmology $\boldsymbol{\Theta}_{\text{fid}}$ and estimate the distortion by evaluating the CAMB power spectrum for this cosmology in a regular grid in Fourier space, computing its power spectrum by averaging over spherical shells, and then comparing this result to the standard spectrum outputted by CAMB. One can then multiply the estimated spectra from a certain dataset by this factor to recover the correct amplitude.

# Chapter 4

# Systematic Effects

When analyzing data from real observations, several other difficulties present themselves. These come in the form of systematical errors, contaminants which distort our measurements and must be taken into account, to prevent severely biasing the cosmological results. In the following sections we will discuss the main systematic effects contaminating measurements of galaxy power spectra from the VIPERS survey (Guzzo et al., 2014).

## 4.1 Window Function

Arguably, the main effect of this type in spectroscopic surveys such as VIPERS is that of the window function. The window function defines the regions of the sky which were effectively measured by the telescope. Naively one might think that every region to which the telescope points will be observed entirely. Reality is much more complex, and there will be several reasons due to which vast regions will remain unobserved, despite the telescope having pointed at them. One main such reason is the shape of the CCD plates themselves, that is, the instruments that will collect the photons. In general one cannot join the CCDs perfectly, and there remain small spaces between them which, when pointed at the sky, will collect no light at all from certain regions of space. Another issue is that of stars or galaxies in the local universe. These objects will be extremely bright, and therefore their light will saturate the CCD, and regions around them must be excluded. In

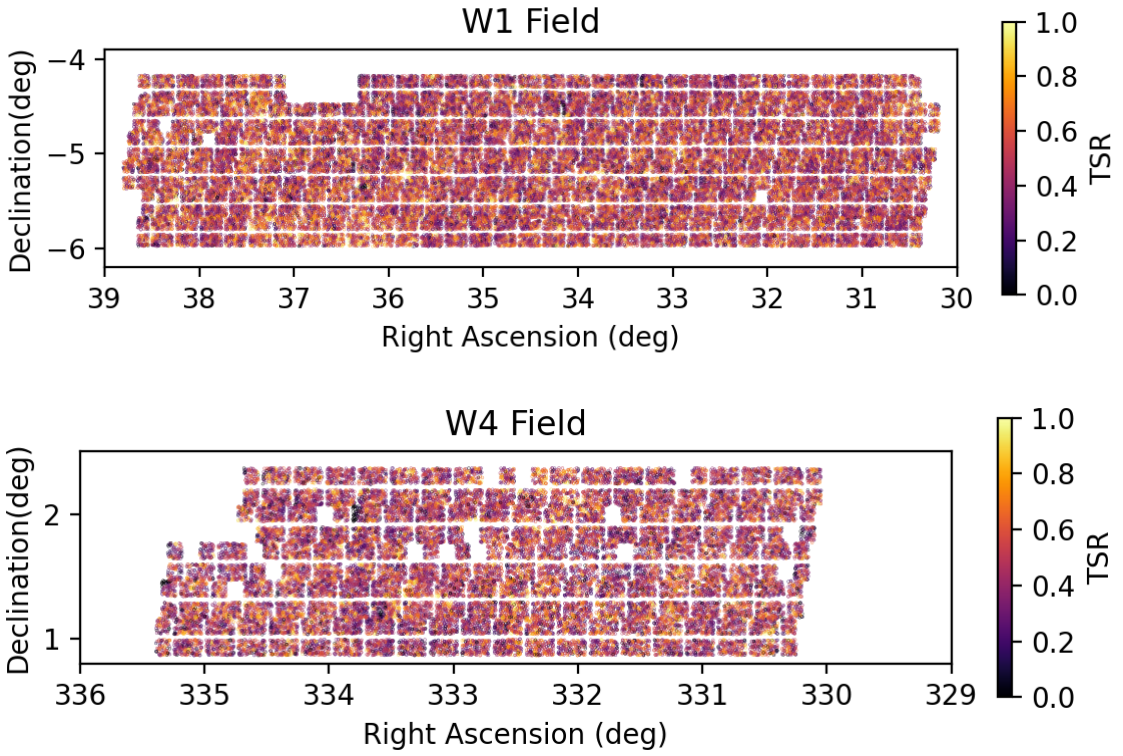


**Figure 4.1:** Observation mask of the VIPERS survey. The thin unobserved regions are present due to small spaces between the CCD plates, which will capture no light. In both fields we also see small square regions which have remained unobserved due to the failure of one of the CCD plates at the time of observation. Each point in this figure represents one observed galaxy, and the color coding encodes its Target-Selection Rate (TSR) value.

figure (4.1) we see a representation of the VIPERS mask for the two fields, W1 and W4. As a result the power spectrum will display a reduction in power at the typical scales of the mask's features.

Let us represent the effects of the mask through a function $W(\boldsymbol{x})$, then the observed galaxy density will relate to the real one as

$$\hat{\delta}(\boldsymbol{x}) = W(\boldsymbol{x})\delta(\boldsymbol{x}), \tag{4.1}$$

and in Fourier space this becomes a convolution

$$\hat{\delta}(\boldsymbol{k}) = \int \frac{d^3\boldsymbol{k}'}{(2\pi)^3} W(\boldsymbol{k}-\boldsymbol{k}')\delta(\boldsymbol{k}'). \tag{4.2}$$

Combining $\delta(\boldsymbol{k})$ with its complex conjugate we can obtain an expression for the observed

power spectrum

$$\widehat{P}(\boldsymbol{k}) = \int \frac{d^3\boldsymbol{k}'}{(2\pi)^3} |W(\boldsymbol{k} - \boldsymbol{k}')|^2 P(\boldsymbol{k}'). \tag{4.3}$$

The quantity of interest here, $P(\boldsymbol{k})$ is not what we have direct access to, and there are essentially two proposals of how one could circumvent this issue: deconvolving the measured power spectrum to remove the effects of the window function, or forward modelling the window function effects into the theoretical model.

The first of these techniques involves computing the power spectrum as usual, then taking its inverse Fourier transform to obtain a correlation function – in real space the window function is much simpler, just a multiplication, and therefore, we simply divide by the squared window function, and take the Fourier transform of this correlation function to obtain the deconvolved power spectrum. This process has the advantage that the result of the analysis of a certain dataset can be directly compared to the theoretical model; however, it has a number of disadvantages, namely:

- This is a slow process, since it involves estimating the power spectrum, then taking two additional Fourier transforms. If we are working with a very small cell size, this could take a very substantial amount of time, making the process hard to test;
- Furthermore, the precision of this deconvolution will be limited to the resolution in $k$-space of the grid;
- Finally, the weighting scheme used to estimate these spectra (FKP or MTOE) is optimal for the observed density field, and there is no guarantee that the deconvolved spectra will maintain this nice property.

On the other hand, we can list several advantages of the process of estimating the window function separately and then convolving it with the theoretical power spectrum, namely:

- The slow part of this process is the one of doing a pair counting on a large catalog of randoms which follows the same mask as the data, but it must be done only once in the analysis of a certain survey;
- The process of actually convolving the window function with the theoretical spectrum is extremely fast since it can be done using the FFTLog algorithm of Hamilton,

2000;

- Moreover, this is an extremely precise calculation, and does not depend on making the cell size of the grid smaller.

Due to the disadvantages of the first, and the advantages of the second, we choose to apply the latter to our analysis.

It is conceptually simple, although numerically complex, to see how one could implement equation (4.3) once in possession of estimates for the theoretical power spectrum and the survey window function. It is not that clear how to do this for the power-spectrum multipoles, and therefore, we must derive the relations through which we can obtain their convolution with the survey window function. Following Beutler et al., 2014; Wilson et al., 2016, we begin by defining the observed multipoles

$$\begin{aligned}\widehat{P}_\ell(k) &= (2\ell+1)\int \frac{d\Omega_k}{4\pi}\widehat{P}(\boldsymbol{k})\mathcal{L}_\ell(\hat{\boldsymbol{k}}\cdot\hat{\boldsymbol{\eta}}) \\ &= (2\ell+1)\int \frac{d\Omega_k}{4\pi}\mathcal{L}_\ell(\hat{\boldsymbol{k}}\cdot\hat{\boldsymbol{\eta}})\underbrace{\int \frac{d^3\boldsymbol{q}}{(2\pi)^3}P(\boldsymbol{q})|W(\boldsymbol{k}-\boldsymbol{q})|^2}_{=\int d^3\boldsymbol{r}e^{-i\boldsymbol{k}\cdot\boldsymbol{r}}\xi(\boldsymbol{r})Q(\boldsymbol{r})} \\ &= (2\ell+1)\int \frac{d\Omega_k}{4\pi}\mathcal{L}_\ell(\hat{\boldsymbol{k}}\cdot\hat{\boldsymbol{\eta}})\int d^3\boldsymbol{r}e^{-i\boldsymbol{k}\cdot\boldsymbol{r}}\xi(\boldsymbol{r})Q(\boldsymbol{r}),\end{aligned} \tag{4.4}$$

in which we have used the convolution theorem, and defined

$$Q(\boldsymbol{r}) = \int \frac{d^3\boldsymbol{k}}{(2\pi)^3}e^{i\boldsymbol{k}\cdot\boldsymbol{r}}|W(\boldsymbol{k})|^2. \tag{4.5}$$

Notice also that, whenever necessary, we have defined $\mu = \hat{\boldsymbol{k}}\cdot\hat{\boldsymbol{\eta}}$, also known as the plane-sky approximation; this approximation will be used many times throughout this derivation. Expanding the exponential in equation (4.4) into Legendre polynomials we

obtain

$$\begin{aligned}\widehat{P}_\ell(k) =& \sum_{p=0}^{\infty}(2\ell+1)(-i)^p \int d^3\boldsymbol{r}\xi(\boldsymbol{r})Q(\boldsymbol{r})j_p(kr) \underbrace{\frac{(2p+1)}{2}\int d(\hat{\boldsymbol{k}}\cdot\hat{\boldsymbol{\eta}})\int \frac{d\phi_k}{2\pi}\mathcal{L}_\ell(\hat{\boldsymbol{k}}\cdot\hat{\boldsymbol{\eta}})\mathcal{L}_p(\hat{\boldsymbol{k}}\cdot\hat{\boldsymbol{r}})}_{\delta^K_{\ell p}\mathcal{L}_\ell(\hat{\boldsymbol{r}}\cdot\hat{\boldsymbol{\eta}})} \\ =&(2\ell+1)(-i)^\ell \int d^3\boldsymbol{r}\xi(\boldsymbol{r})Q(\boldsymbol{r})j_\ell(kr)\mathcal{L}_\ell(\hat{\boldsymbol{r}}\cdot\hat{\boldsymbol{\eta}}) \\ =&(2\ell+1)(-i)^\ell \sum_{\ell'=0}^{\infty}\int d^3\boldsymbol{r}\xi_{\ell'}(r)Q(\boldsymbol{r})j_\ell(kr)\mathcal{L}_\ell(\hat{\boldsymbol{r}}\cdot\hat{\boldsymbol{\eta}})\mathcal{L}_{\ell'}(\hat{\boldsymbol{r}}\cdot\hat{\boldsymbol{\eta}})\end{aligned} \tag{4.6}$$

and we can use that

$$\mathcal{L}_\ell(\hat{\boldsymbol{r}}\cdot\hat{\boldsymbol{\eta}})\mathcal{L}_{\ell'}(\hat{\boldsymbol{r}}\cdot\hat{\boldsymbol{\eta}}) = \sum_{q=0}^{\min(\ell,\ell')} A^q_{\ell,\ell'}\mathcal{L}_{\ell+\ell'-2q}(\hat{\boldsymbol{r}}\cdot\hat{\boldsymbol{\eta}}). \tag{4.7}$$

Substituting this into the expression for $\widehat{P}_\ell(k)$ we obtain,

$$\begin{aligned}\widehat{P}_\ell(k) =&(2\ell+1)(-i)^\ell \sum_{\ell',m=0}^{\infty}\sum_{q=0}^{\min(\ell,\ell')} A^q_{\ell,\ell'}\int r^2 dr\xi_{\ell'}(r)Q_m(r)j_\ell(kr) \\ &\times \underbrace{\iint d(\hat{\boldsymbol{r}}\cdot\hat{\boldsymbol{\eta}})d\phi_r\mathcal{L}_{\ell+\ell'-2q}(\hat{\boldsymbol{r}}\cdot\hat{\boldsymbol{\eta}})\mathcal{L}_m(\hat{\boldsymbol{r}}\cdot\hat{\boldsymbol{\eta}})}_{\frac{4\pi}{2q+1}\delta^K_{\ell+\ell'-2q,m}} \\ =&4\pi(-i)^\ell \sum_{\ell'=0}^{\infty}\sum_{q=0}^{\min(\ell,\ell')} A^q_{\ell,\ell'}\left(\frac{2\ell+1}{2(\ell+\ell'-2q)+1}\right)\int r^2\xi_{\ell'}(r)Q_{\ell+\ell'-2q}(r)j_\ell(kr)dr.\end{aligned} \tag{4.8}$$

Let us look at the case $\ell = 0$ to illustrate how this will be used in practice; the expression for $\widehat{P}_0$ will be given by

$$\widehat{P}_0(k) = 4\pi\sum_{\ell'}^{\infty}\left(\frac{1}{2\ell'+1}\right)A^0_{\ell',0}\int r^2\xi_{\ell'}(r)Q_{\ell'}(r)j_0(kr). \tag{4.9}$$

The coefficients $A^q_{\ell,\ell'}$ are given by

$$\begin{aligned} A^q_{\ell,\ell'} =& \frac{G_{\ell-q}G_qG_{\ell'-q}}{G_{\ell+\ell'-q}}\left(\frac{2\ell+2\ell'-4q+1}{2\ell+2\ell'-2q+1}\right) \\ G_q =& \frac{1\cdot 3\cdot 5\cdots(2q-1)}{q!} = \frac{2^q\left(\frac{1}{2}\right)_q}{q!} \end{aligned} \tag{4.10}$$

so that the relevant coefficient in this case is given by $A^0_{\ell',0} = 1$, as can be clearly seen from the former expressions. Therefore, one can rewrite equation (4.9) as

$$\widehat{P}_0(k) = 4\pi \int r^2 \left(\sum_{\ell'=0}^{\infty} \frac{1}{2\ell'+1}\xi_{\ell'}(r)Q_{\ell'}(r)\right) j_0(kr). \tag{4.11}$$

The term inside parenthesis is usually called the convolved correlation function and denoted by the symbol $\xi'_0(r)$; truncating this expression up to $\ell' = 6$ we have

$$\xi'_0(r) = \xi_0 Q_0 + \frac{1}{5}\xi_2 Q_2 + \frac{1}{9}\xi_4 Q_4 + \frac{1}{13}\xi_6 Q_6. \tag{4.12}$$

Performing a similar computation for the $\ell = 2$ term, one finds

$$\begin{aligned} \xi'_2(r) =& \xi_0 Q_2 + \xi_2\left(Q_0 + \frac{2}{7}Q_2 + \frac{2}{7}Q_4\right) + \xi_4\left(\frac{2}{7}Q_2 + \frac{100}{693}Q_4 + \frac{25}{143}Q_6\right) \\ &+ \xi_6\left(\frac{25}{143}Q_4 + \frac{14}{143}Q_6 + \frac{28}{221}Q_8\right). \end{aligned} \tag{4.13}$$

Although a bit cumbersome, this calculation is very efficient when implemented numerically, allowing it to be incorporated into a Markov Chain Monte-Carlo exploration of the posterior distribution. Equation (4.8) can be evaluated through a series of Hankel transforms, which in turn can be computed using 1D FFTs by means of the FFTLog algorithm (Hamilton, 2000). To perform the Hankel transforms we have used the code `mcfit`, publicly available at https://github.com/eelregit/mcfit.

### 4.1.1 Pair Counting Approach

We have the expressions to compute the convolved power spectra, and we can use FFTLog to compute the Hankel transforms efficiently, but a fundamental ingredient is still

lacking, the $Q_\ell$.

From equation (4.5) we see that $Q(\boldsymbol{r})$ is nothing more than the correlation function of the window function $W(\boldsymbol{x})$, and therefore, one can compute it by doing a simple pair counting, as is done to compute the correlation function of galaxies. Let us suppose we have a catalogue of objects randomly distributed with a constant number density $\bar{n}_s$, and we impose over it the VIPERS mask $W(\boldsymbol{x})$. The number of available pairs is given by

$$RR(\boldsymbol{x}_1, \boldsymbol{x}_2) = \frac{\bar{n}_s^2}{2} W(\boldsymbol{x}_1) W(\boldsymbol{x}_2) dV_1 dV_2. \tag{4.14}$$

Now substituting $\boldsymbol{x}_2 = \boldsymbol{x}_1 + \boldsymbol{r}$ and then integrating over $\boldsymbol{x}_1$, we obtain

$$RR^{tot}(\boldsymbol{r}) = \frac{\bar{n}_s^2}{2} dV_2 \underbrace{\int d^3\boldsymbol{x}_1 W(\boldsymbol{x}_1) W(\boldsymbol{x}_1 + \boldsymbol{r})}_{Q(\boldsymbol{r})}, \tag{4.15}$$

in which we have used that $\int d^3\boldsymbol{x}_1 W(\boldsymbol{x}_1) W(\boldsymbol{x}_1 + \boldsymbol{r}) = Q(\boldsymbol{r})$; this is simply another way to rewrite equation (4.5) – the right-hand side of that equation is the inverse Fourier transform of a product of two functions, and hence will become, in real space, a convolution between these two functions. Since we are interested in the multipoles of $Q(\boldsymbol{r})$ we can integrate this expression multiplied by $(2\ell+1)\mathcal{L}_\ell(\hat{\boldsymbol{r}} \cdot \hat{\boldsymbol{\eta}})$ over a thin shell of width $d(\ln(r))$, to obtain the Legendre coefficient of order $\ell$,

$$RR_\ell^{tot}(r) = 2\pi r^3 d(\ln r) \frac{\bar{n}_s^2}{2} Q_\ell(r). \tag{4.16}$$

Inverting this relation, we can clearly obtain a numerical result for $Q_\ell$ from the pair counting of the random catalogue. The $Q_\ell$ computed in this fashion for the window function of the $W_1$ observations field of the VIPERS field in the $z_1$ slice can be seen in figure (4.2).

## 4.2 Incompleteness Effects

In order to measure the spectra of galaxies, the VIPERS survey makes use of an instrument called a multi-object spectrograph (hereafter MOS). This consists of optical instruments which will decompose the incoming light of a galaxy into its spectral compo-

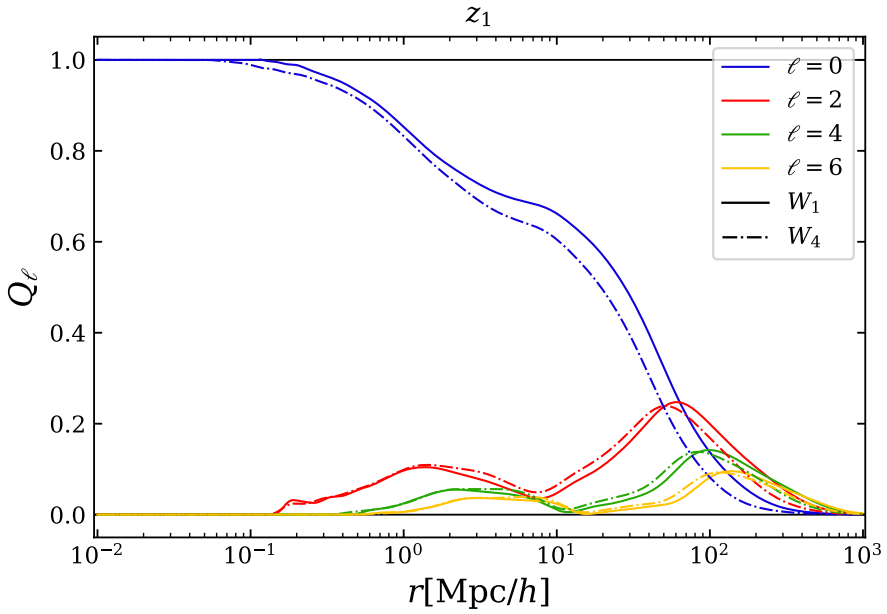


**Figure 4.2:** Calculation of the $Q_\ell(r)$ for the VIPERS survey window-function, restricted to the $z_1$ slice, containing redshifts $z \in [0.55, 0.7]$. It is interesting to notice that as $r \to 0$, $Q_0 \to 1$, and the higher order multipoles go to zero; indeed this is expected, as for very small scales, the mask has no effect, and the power spectrum can be measured without distortions. As $r$ increases, however, we see that the monopole decreases, and there is leakage of power to higher $\ell$; notice that these multipoles have nothing to do with RSDs, they appear because the features of the mask will create artificial anisotropies, and thus increase the power in multipoles of higher $\ell$.

nents and direct it into a CCD plane, which will then collect the photons, thus recording the spectrum of the galaxy. In figure (4.3) one can see an actual image of the MOS used in VIPERS taking spectra of some field of galaxies. It is not hard to see that, if two galaxies are located very near to each other, it will not be possible to observe both their spectra simultaneously, since the slits which must be placed on top of them to direct their light into the CCD have a finite size, and one cannot superimpose two slits.

This effect, usually known as "slit collision" for surveys using this kind of instrument, or "fiber-collision" for surveys using optical fibers to direct the light of the galaxies onto a CCD plate, will be a very important contaminant to the derived clustering statistics. Notice how the dense regions of the galaxy field will be much more affected by this, since objects are closer together, and thus harder to observe. Moreover, the spectra are always projected in the CCD with their larger dimension along the declination direction, and therefore, galaxies will be much more poorly sampled along this direction, since one can fit less spectra onto the CCD, than on the right-ascension direction. The first issue will

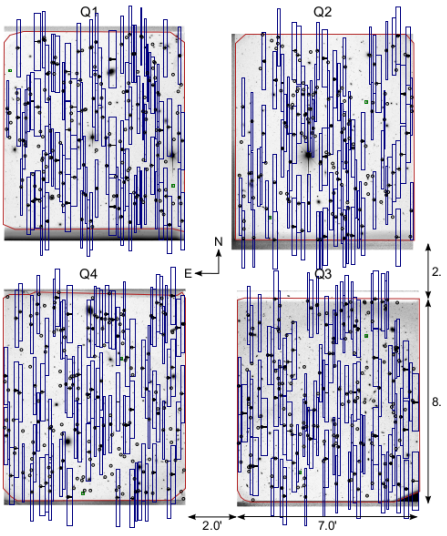


**Figure 4.3:** Observation plate from the VIPERS survey. The large white squares are the CCDs, black dots are galaxies, and the blue squares represent the area of the CCD onto which the spectrum of the galaxy will be diffracted. This makes it clear why galaxies which are very close together cannot be observed simultaneously.

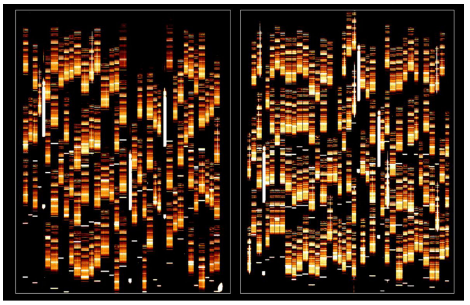

**Figure 4.4:** Actual Galaxy spectra projected onto the CCD plates, obtained with VIMOS in Multi-Object-Spectrograph mode. Extracted from https://www.eso.org/public/brazil/images/eso0209b/?lang

introduce a large damping at the small scales, and the latter will give rise to an artificial anisotropic signal, both of which must be corrected for.

Since only part of the available galaxies in a certain region of space will be observed, one can define a number called the Target Selection Rate (TSR), which measures how many of the available galaxies in the photometric catalog will actually be targeted by the spectrograph. This number can be estimated by interpolating the density of the photometric and spectroscopic catalogues at the angular positions of each of the galaxies and then taking their ratio,

$$\mathrm{TSR}_i = \frac{1+\delta_i^s}{1+\delta_i^p}, \tag{4.17}$$

in which the index $i$ represents a certain galaxy in the observed sample. Another important incompleteness effect is due to eventual failures of spectroscopic measurements, i.e.: a certain galaxy was targeted by the telescope, but its spectra does not have sufficient precision or the observations failed for some reason. These failures will occur mostly due to a galaxy being extremely faint, not allowing for its spectrum to be reliably determined;

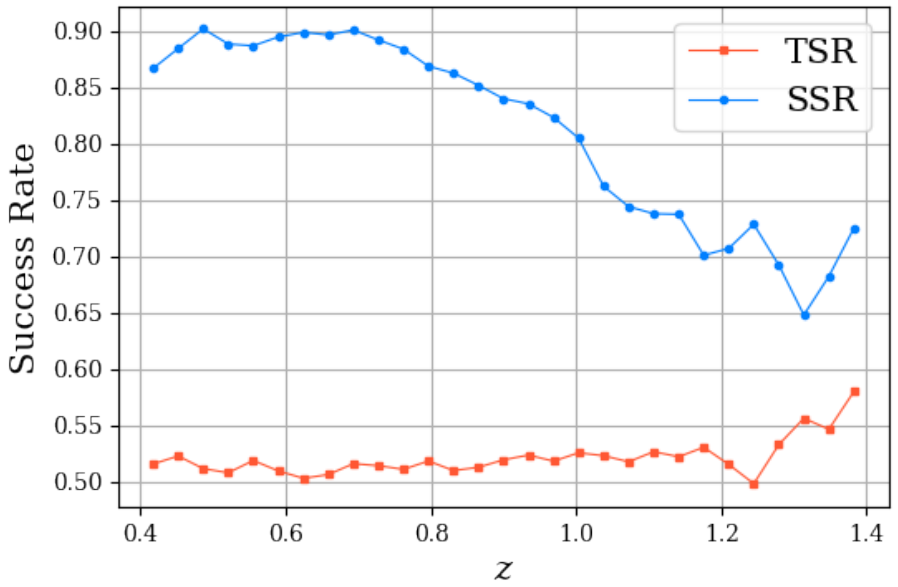


**Figure 4.5:** Target sampling rate (TSR) and spectroscopic success rate (SSR) as a function of redshift. TSR does not present any significant trend with redshift, as it depends mostly on how clustered together the possible targets are; SSR on the other hand clearly decreases with redshift, since galaxies become fainter, and therefore, harder to observe and obtain reliable spectroscopy.

this implies that there is a clear trend of spectroscopic-success rate (SSR) decreasing as $z$ increases, as can be seen in figure (4.5). In a similar fashion to what was done for TSR, one can interpolate the density field of targets and successful targets at the positions of galaxies, and take their ratio to obtain a local measure of the SSR,

$$\mathrm{SSR}_i = \frac{1+\delta_i^{\mathrm{success}}}{1+\delta_i^{\mathrm{target}}}. \tag{4.18}$$

We can then define a set of weights given by

$$w_i = \frac{1}{\mathrm{TSR}_i \times \mathrm{SSR}_i}, \tag{4.19}$$

and use these as artificial masses for the galaxies when constructing the gridded density field from this population. This will allow us to up-weight regions which had been down-weighted by the selection effects, thus correcting the distortions.

## 4.3 Integral Constraint

Let us briefly recall the definition of the FKP field, which we will use to estimate the power spectrum of galaxies:

$$F(\boldsymbol{r}) = \frac{w_{\rm FKP}(\boldsymbol{r})}{N} \left[ n_g(\boldsymbol{r}) - \alpha n_r(\boldsymbol{r}) \right], \tag{4.20}$$

in which $\alpha \to \sum_i n_g / \sum_i n_r$. From these definitions it is not hard to see that the mean of $F(\boldsymbol{r})$ over the survey volume is zero by construction; of course, this causes an issue because we don't know what is the actual mean density of a certain region, and impose an artificial constraint on our spectrum, usually named the integral constraint, for requiring that $F$ satisfy

$$\int d^3\boldsymbol{r} F(\boldsymbol{r}) = 0. \tag{4.21}$$

This means that, if the region being analyzed has a slightly different mean density from the rest of the universe, this will be ignored by the estimator, and there will be a constant offset between the actual overdensity and the one being used to estimate the power spectrum, i.e.

$$F(\boldsymbol{r}) \to F(\boldsymbol{r}) - \int d^3\boldsymbol{r} F(\boldsymbol{r}). \tag{4.22}$$

The original field might have been slightly displaced from zero, which would translate to Fourier space as a spike at $\boldsymbol{k} = 0$; therefore, the new field which has perfectly null mean, will be zero at $\boldsymbol{k} = 0$. These effects will also be present in the power spectrum of these fields, and the original power spectrum would have a spike at $\boldsymbol{k} = 0$, whereas the new spectrum would not. In principle this is not an issue, since the $\boldsymbol{k} = 0$ mode is not observationally accessible; however, because of the irregular survey geometry, the power spectrum will be convolved with a complex window function, which will mix different wavenumbers, and these differences in the $\boldsymbol{k} = 0$ mode will get transported to scales which are of our interest.

Several works, namely (Wilson et al., 2016; Beutler, Castorina, and Zhang, 2019; de Mattia and Ruhlmann-Kleider, 2019) have shown that the correct way to account for the integral constraint in the multipoles of the power spectrum is to correct the theoretical

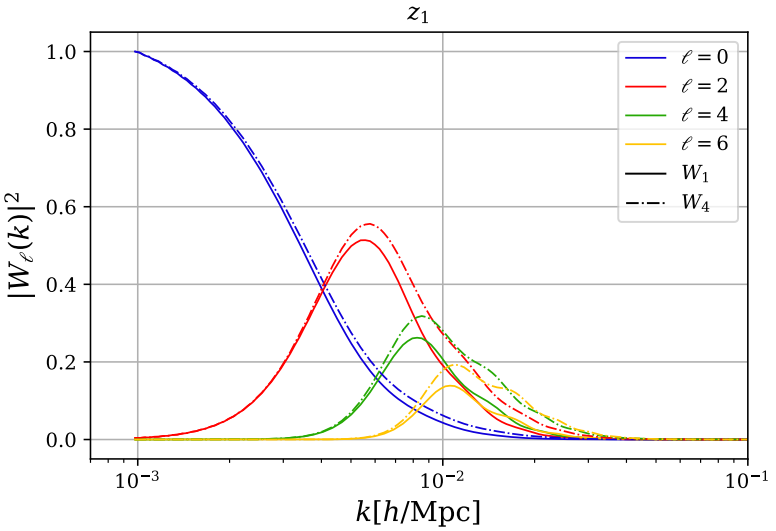


**Figure 4.6:** $W_\ell(\boldsymbol{k})$ for the mask of the W1 field of the VIPERS survey. This is the squared modulus of the Fourier transform of the $Q_\ell(r)$, and will multiply the monopole of the power spectrum in order to give us the integral constraint correction for different multipoles.

model through the expression

$$P'_\ell(k) = P_\ell(k) - P_0(k)|W_\ell(k)|^2, \tag{4.23}$$

in which $W_\ell(k)$ is the Hankel transform of $Q_\ell(\boldsymbol{r})$. From figure (4.6), we can see that $W_\ell(k)$ goes to 1 as $k \to 0$, and therefore, for $P_0$ we obtain the expected behavior, i.e. when $k \to 0$, it will satisfy $P_0(0) = 0$. Due to its small size, the minimum $k$ which VIPERS can probe is $\sim 10^{-2}[h/\mathrm{Mpc}]$, and therefore, we see that the integral constraint is not very relevant to the correction of the spectra, especially because, at these large scales, the variance of the spectra is extremely large.

# Chapter 5

# VIPERS Analysis

All the tools are now available, and we can proceed to the actual analysis of the VIPERS data. We will begin by giving a brief description of the dataset, including both the actually measured data, as well as the mocks developed to approximately reproduce the observed data, which will be used both to compute covariance matrices, and to test the pipeline for possible biases. Following that, we will explain the analysis pipeline as a whole, assembling the different pieces which have been developed in the former chapters. We will also demonstrate, using the VIPERS mocks, that our analysis pipeline is capable of producing unbiased results, to the level of precision that the VIPERS data is capable of reaching. Finally, we will present the results of our analysis of the real data, as well as our constraints on the value of $f\sigma_8(z)$.

## 5.1 The VIPERS Survey

The VIMOS Public Extragalactic Redshift Survey (VIPERS) [1] (Guzzo et al., 2014) is a spectroscopic redshift survey, completed in the year 2016, mapping the angular positions and redshifts of $88,901$ galaxies selected from targets provided by optical photometry from the Canada-France-Hawaii Telescope Legacy Survey-Wide (CFHTLS-Wide)[2]. Although it has a small area, of only $24\text{deg}^2$, the VIPERS survey covers a large red-

[1] http://vipers.inaf.it/

[2] https://www.cfht.hawaii.edu/Science/CFHTLS/

shift range, going from $z = 0.5$ up to high values of $z = 1.2$, and therefore, its volume, $V \approx 5 \times 10^7 [\text{Mpc}/h]^3$, is comparable to previous surveys such as the 2dF Galaxy Redshift Survey (Colless et al., 2001), which had huge angular coverage of around $12,000 \text{deg}^2$, but went only up to redshift $z = 0.3$, yielding a volume of $V \approx 10^8 [\text{Mpc}/h]^3$.

The targets for VIPERS are chosen from CFHTLS using a colour-selection scheme, which is able to separate well the galaxies which are above $z = 0.5$, just using the photometric data; on the high end of the redshift distribution, the survey has a magnitude limit, namely $i_{AB} < 22.5$, explaining the strong suppression at redshifts $z \approx 1.2$ which we can see in figure (5.1). Once the galaxies satisfying this condition are chosen, an algorithm is run, which optimally positions the slits of the MOS, which will decompose the light into spectra and project it onto the CCD (Bottini et al., 2005); as already described above, this algorithm will not be able to target all galaxies available, and even for the galaxies it targets, it may not be able to obtain redshift of sufficient quality, producing a spectroscopic failure. All galaxies for which VIPERS measures redshifts are also assigned a flag, which indicates the confidence level on the measured value; in this work we will only use data with redshift flags $> 2$ since they indicate a $98\%$ level of confidence on the measurement. For the chosen flags, the VIPERS survey measures redshifts with great precision, the typical error being $\sigma_z = 4.7(1 + z)10^{-4}$.

## 5.2 Pipeline Overview

In this section we give a general overview of how we combine the tools described up to now in a pipeline to take cosmological data and turn it into constraints on cosmological parameters. Before entering the pipeline itself, some preliminary steps are necessary. The first is to take the mocks and use them to compute $\bar{n}(r)$; this is then used to generate a catalog of random points which follows the VIPERS mask and this radial distribution; counting pairs of random objects one is capable of measuring the influence of the window function on the two-point clustering statistics, i.e.: the $Q_\ell$. Once we actually get into the pipeline, it is essentially divided into two branches, as can be seen from figure (5.2):

- **Theory Branch:** This part of the code is responsible for taking a set of cosmo-

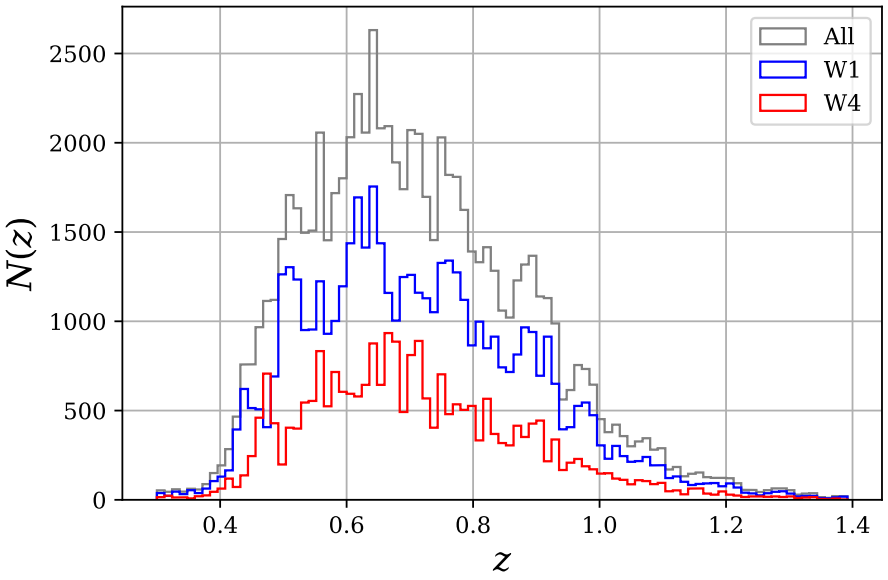


**Figure 5.1:** Distribution of VIPERS galaxies according to redshift. Blue lines indicate galaxies detected in the W1 field, and red lines represent the amount of those detected in the W4 field; gray lines indicate the combination of both.

logical and nuisance parameters, and turning them into a theoretical model for our measurements. We begin by computing the matter power spectrum with CAMB, for the relevant cosmology $\boldsymbol{\Theta}$; we then use the input values for the bias $b_1$, and the velocity dispersion to compute the anisotropic power spectrum

$$P(\boldsymbol{k}) = b_1^2 \left(1 + \beta\mu^2\right)^2 P_m(k) e^{-k^2\sigma^2\mu^2}, \tag{5.1}$$

and from it we compute the power-spectrum multipoles, $P_\ell(k)$. Notice how in the preceding expression, $\sigma$ has units of $[h/\mathrm{Mpc}^{-1}]$; in the next sections a similar quantity will appear, which we name $\sigma_v$. This is related to $\sigma$ by the simple expression

$$\sigma_v = H\sigma, \tag{5.2}$$

in which $H$ is simply the Hubble parameter. We will use $\sigma_v$ occasionally because it can be more easily interpreted as a velocity dispersion, as it has units of km/s. The next step is to convolve these multipoles of the power spectrum with the window-function of the survey; this can be achieved by using equations (4.12, 4.13) to give us the convolved spectra $P'_\ell(k)$, and upon applying to it the integral constraint,

we have a model for the estimates coming from the real data. When running the Markov-Chain Monte-Carlo methods to constrain the parameters, we also allow for an extra shot-noise contribution, which can be either positive or negative, and add it to the monopole of the power spectrum according to the expression

$$P_0(k) = \frac{1}{2}\int_{-1}^{1} d\mu \mathcal{L}_0(\mu) P(k,\mu) + P_{SN}^{\text{extra}}. \tag{5.3}$$

- **Estimation Branch:** This part of the code does the estimation of the spectra, making sure to reduce possible sources of biases. The first step is to take the data, which is provided in sky coordinates, and transform them to cartesian coordinates using a certain fiducial cosmology $\mathbf{\Theta}_{\text{fid}}$; the next step is to use a MAS to interpolate the density field of these galaxies onto a regular grid. In fact, we interpolate this density field onto two grids which are slightly shifted with respect to each other, in such a way that we can combine them in a process called "interlacing", reducing the effects of aliasing; furthermore, we deconvolve the window-function of the MAS. We can then use these density fields to compute the optimally weighted monopole and quadrupole of the power spectrum using FKP or MTOE weights and the Yamamoto estimator, and we finally apply the binning corrections to obtain a reliable estimate of $\widehat{P}_\ell(k)$.

We can then use the mocks to compute the covariance matrix of the monopole, quadrupole, and the cross-covariance between them, namely:

$$\begin{aligned}
C_{00}(k,k') =& \frac{1}{N-1}\sum_{i=1}^{N}\left(P_0^i(k) - \langle P_0(k)\rangle\right)\left(P_0^i(k') - \langle P_0(k')\rangle\right) \\
C_{22}(k,k') =& \frac{1}{N-1}\sum_{i=1}^{N}\left(P_2^i(k) - \langle P_2(k)\rangle\right)\left(P_2^i(k') - \langle P_2(k')\rangle\right) \\
C_{02}(k,k') =& \frac{1}{N-1}\sum_{i=1}^{N}\left(P_0^i(k) - \langle P_0(k)\rangle\right)\left(P_2^i(k') - \langle P_2(k')\rangle\right),
\end{aligned} \tag{5.4}$$

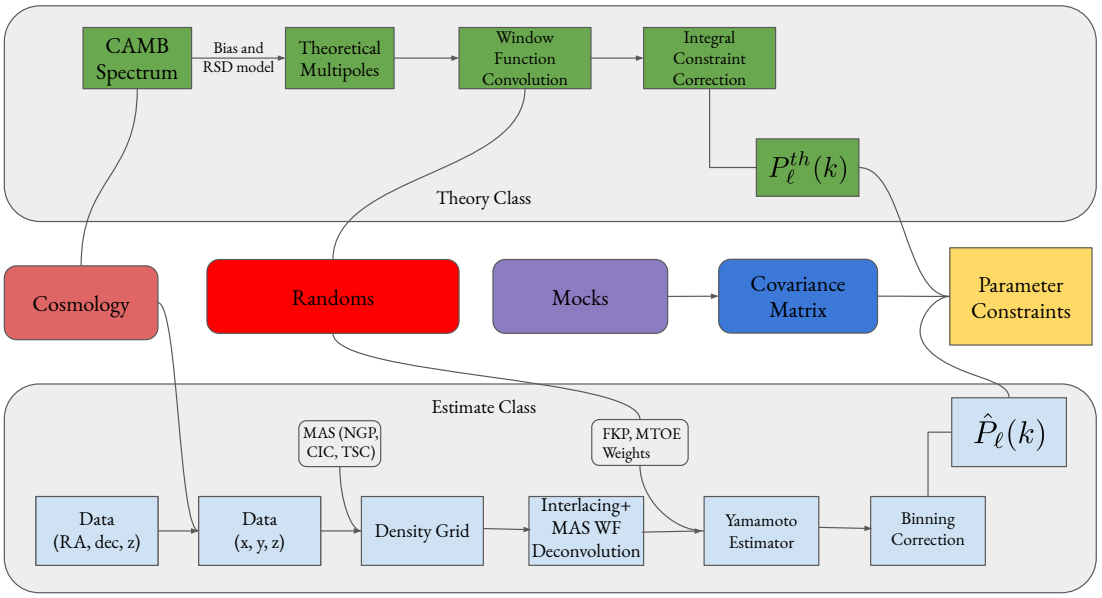


**Figure 5.2:** Flowchart explaining the functioning of the analysis pipeline. On the upper part we have the theory branch, responsible for taking the CAMB spectrum, applying a certain bias and RSD modelling, then forward modelling onto it the effects of the window function, and finally correcting for the integral constraint. The lower part shows the estimation branch, which is responsible for taking the catalogues of the positions of galaxies and estimating their optimal power spectra, using either FKP or MTOE weights.

and combine them into one large covariance matrix for the analysis of the monopole and quadrupole,

$$C = \left(\begin{array}{c|c} C_{00} & C_{02} \\ \hline C_{20} & C_{22} \end{array}\right) . \tag{5.5}$$

Once we have the theoretical model $P_\ell^{th}(k)$ and the estimate from the data, $\widehat{P}_\ell(k)$, we can combine them with the covariance matrix to compute the likelihood of the data given a certain test cosmology $\mathbf{\Theta}$, which will be modelled as a multi-variate Gaussian, and will thus be given by

$$\mathcal{L}(\widehat{P}_\ell|\mathbf{\Theta}) = \frac{1}{\sqrt{(2\pi)^N \det C}} \exp\left[-\frac{1}{2}\sum_{i,j}\left(\widehat{P}_\ell(k_i) - P_\ell^{th}(k_i)\right) C^{-1}(k_i,k_j) \left(\widehat{P}_\ell(k_j) - P_\ell^{th}(k_j)\right)^T\right] . \tag{5.6}$$

Our model for the power spectrum can be quickly computed for different cosmological and nuisance parameters, and therefore, we can run a code which uses the Markov-Chain Monte-Carlo method to explore the parameter space quickly, finding the point of

maximum likelihood and characterizing the width of the distribution which will essentially be the error bars on a certain parameter once we marginalize over all the others. The parameters over which we will vary are $f$, $b_1$, $\sigma_v$ and $\bar{n}P_{SN}^E$, which are, respectively, the matter growth-rate, linear bias parameters, velocity dispersion parameter and normalized extra shot-noise parameter. Notice that only one of these is a cosmological parameter, $f$, the others all being nuisance parameters, i.e.: one has no interest in their value, but it is important to allow them to vary, in order to properly characterize the scatter in $f$. The other cosmological parameters are fixed to the values constrained by Hinshaw et al., 2013; this is justified because the objective of this work is not to produce competitive or independent constraints, but to set up a pipeline for the analysis of real data using MTOE; comparing constraints obtained with FKP and MTOE, even though for a reduced set of parameters, would be enough to shed light on the degree of improvement obtained.

## 5.3 Galaxy Mocks

The mocks used in this work have been developed by de la Torre et al., 2013, populating halos from the Big MultiDark simulation with galaxies using an HOD procedure (Wechsler and Tinker, 2018). As described in de la Torre et al., 2013; Torre et al., 2017, using these procedures they were able to produce 153 independent lightcones for the W1 and W4 regions each. Furthermore, they imposed that the galaxy distribution in these lightcones satisfy both the observational mask and redshift density of the real data. This allows us to characterize the level of scatter in the galaxy distribution of regions analogous to that observed by VIPERS; this knowledge will be encoded in the covariance matrix, and will inform us of how much information our measurements of the power spectrum actually carry.

## 5.4 Testing Pipeline for Biases

An extremely important part in validating an analysis pipeline is to test it for possible biases which are being introduced throughout the process. This can be tested by analyzing the available mocks; for these, one knows what the real values of the parameters are, and

can check whether the analysis pipeline gives constraints which are compatible with them. Unless one has some serious bug in the code, it is expected that, at least in the linear regime, i.e. $k \lesssim [0.1h/\text{Mpc}]$, the model will work properly; therefore, it is customary to analyze the performance of this model as one increases the value of $k_{max}$, the maximum wavenumber used to fit this spectrum. At some scale our simplistic model will no longer be able to reproduce the power spectrum as it enters into the non-linear regime, and the recovered constraints will differ from the fiducial parameters; this is a clear indication that one should conduct the analysis of the real data only up to this wavemode.

Notice that, in this section, we will discuss in depth only the results for the first redshift slice, which we label $z_1$, covering the interval $z \in [0.55, 0.7]$; the results for the other redshift slices, $z_2$ and $z_3$ which cover the ranges $[0.7, 0.9]$ and $[0.9, 1.1]$, respectively, can be seen in the appendices.

It is also very important to analyze the goodness of fit of a certain set of parameters to a given measurement. Otherwise, we risk having our parameters take the correct value, but produce a nonsensical model which clearly does not describe the data. The typical way of quantifying this is through the reduced $\chi^2$, which can be defined as

$$\chi^2_{\text{red}} = \frac{1}{\nu} \sum_{i,j} \left( \widehat{P}_\ell(k_i) - P^{th}_\ell(k_i) \right) C^{-1}(k_i, k_j) \left( \widehat{P}_\ell(k_j) - P^{th}_\ell(k_j) \right)^T , \tag{5.7}$$

in which $\nu$ is the number of degrees of freedom, given by

$$\nu = \text{number of data points} - \text{number of fitted parameters} - 1. \tag{5.8}$$

Under the assumption that the measurements are Gaussian distributed around a fiducial value, and that the errors are the typical widths of these Gaussian distributions, we expect that $\chi^2_{\text{red}} \approx 1$, meaning that the distance of the observations to the fitted model are typically of the same size as the error bars.

Studies of perturbation theory generally place the beginning of the non-linear regime at scales $k \sim 0.1[h/\text{Mpc}]$; for scales smaller than these, perturbation theory schemes generally begin to fail, and great theoretical efforts have been made to extend the accuracy

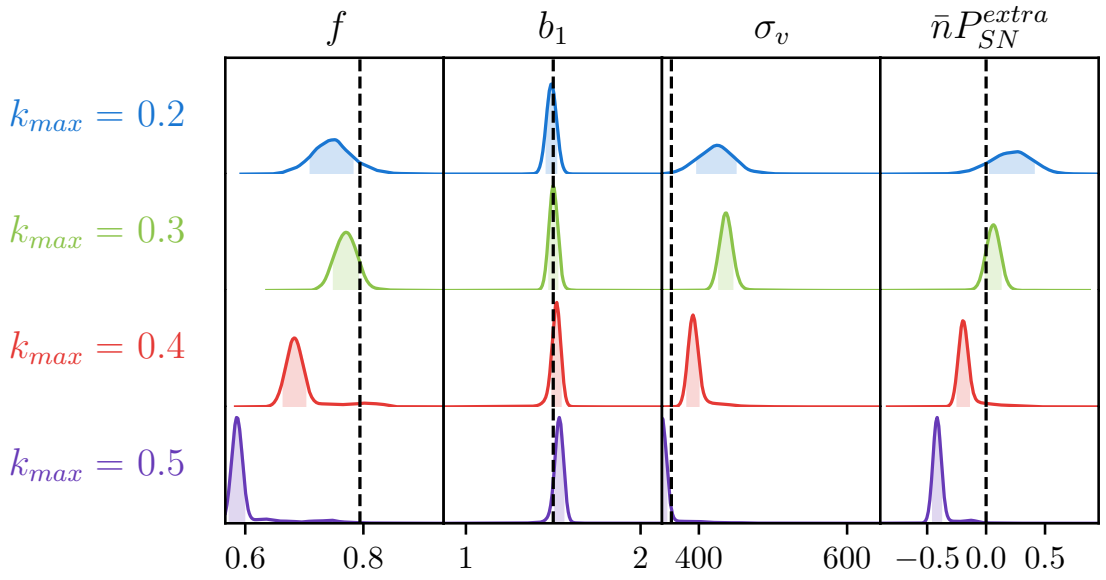


**Figure 5.3:** Posteriors on the constrained parameters varying values of $k_{\rm max}$. This was obtained using the mean of the 153 mocks for the $W_1$ field as data. For the first two values of $k_{\rm max}$ the fiducial value of $f$ is recovered within approximately the 1-$\sigma$ region. As we increase this, however, we can see that the recovered values fall very much below the expected one, indicating the failure of our modelling. The other parameters are not very relevant as we will marginalize over them.

of this modelling up to scales of $0.15 \sim 0.2[h/\text{Mpc}]$. However, previous analyses of the VIPERS survey (de la Torre et al., 2013; Wilson, 2016; Mohammad et al., 2018) have shown that, in this specific case, this limit can be extended well beyond these scales without introducing any biases to the recovered parameters. In this work we see a similar situation, in which we find that one can use wavemodes as large as $k_{\rm max} = 0.3$; we have tested this by using the pipeline to constrain the parameters of interest using the mean of the mock spectra as data. The recovered likelihoods are shown in figure (5.3), for successively increasing values of $k_{\rm max}$; one can see that for $k_{\rm max} = 0.2, 0.3[h/\text{Mpc}]$, $f$ can be recovered to an agreement of approximately 1-$\sigma$ with the fiducial value, and that for scales larger than $0.3[h/\text{Mpc}]$ the constrained values deviate significantly. This shows that, for $k < 0.3[h/\text{Mpc}]$, the systematic errors introduced by our analysis are much smaller than the statistical errors in VIPERS data; for the mean of the 153 mocks, these statistical errors are reduced by a factor $\sqrt{153}$, and even in this case we can still recover the parameters correctly. Figure (5.7) shows the best fit model compared to the data from the mean of the mocks in the $W_1$ observation field, for the $z_1$ slice; it is clear that the model provides a good general agreement with the measured spectra.

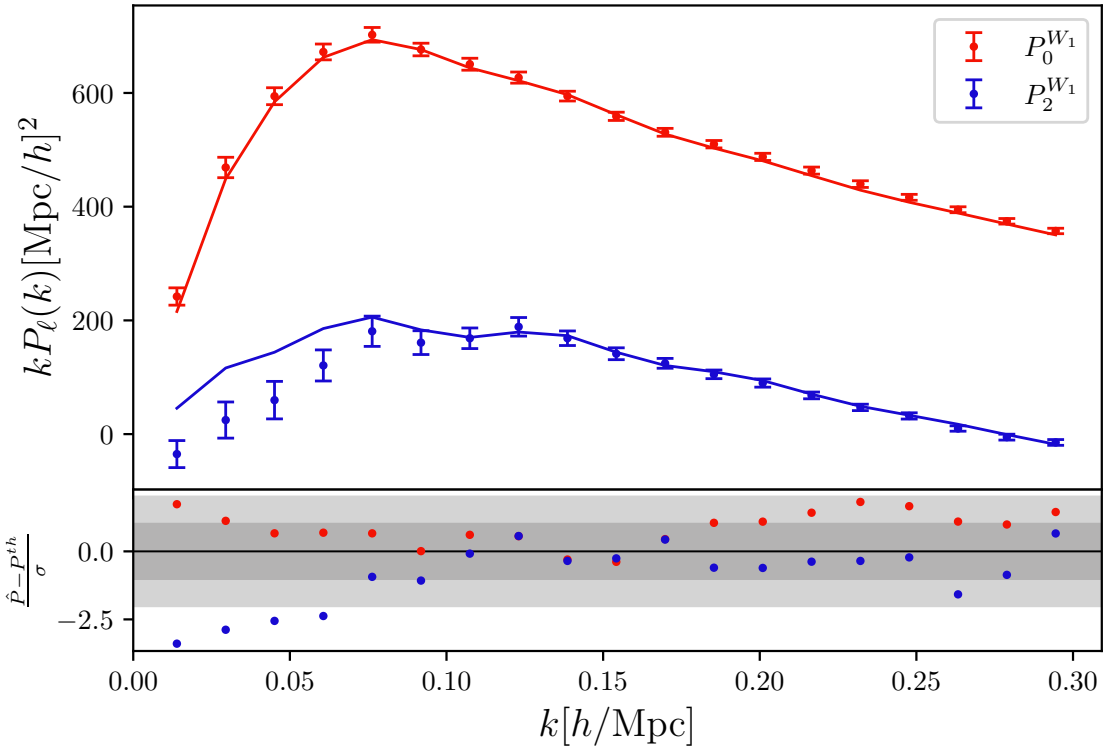


**Figure 5.4:** In the upper panel, he mean of the mock spectra are represented by dots with error bars, and the fits corresponding to the analysis using $k_{\mathrm{max}} = 0.3[h/\mathrm{Mpc}]$ are represented by solid lines. In the lower panel we show the difference between model and measurement, divided by the error at that scale; the darker shade of gray represents the $1-\sigma$ region, and the lighter shade represents the $2-\sigma$ region. The value of the reduced $\chi^2$ for this fit is of $\chi^2_{\mathrm{red}} = 2.12$. which shows a relatively good agreement, which is also shown visually in the plot, allowing for a safe analysis of the real data with this same modelling, and using a similar maximum wavenumber.

## 5.5 Priors

When employing bayesian statistical methods, one must state a certain prior belief regarding the values of the parameters which are being probed. In the specific case of this analysis, everywhere we have used flat priors on the parameters, meaning that we have a uniform belief that the cosmological parameters can take any of the allowed values. To define the allowed values, we have usually taken an interval spanning a $50\%$ deviation from the value constrained in the mock analysis; in case either $f$ or $b$ would saturate this bound, we would then enlarge this interval. In the case of the extra shot-noise term, we have usually allowed it to vary between $-1$ and $1$.

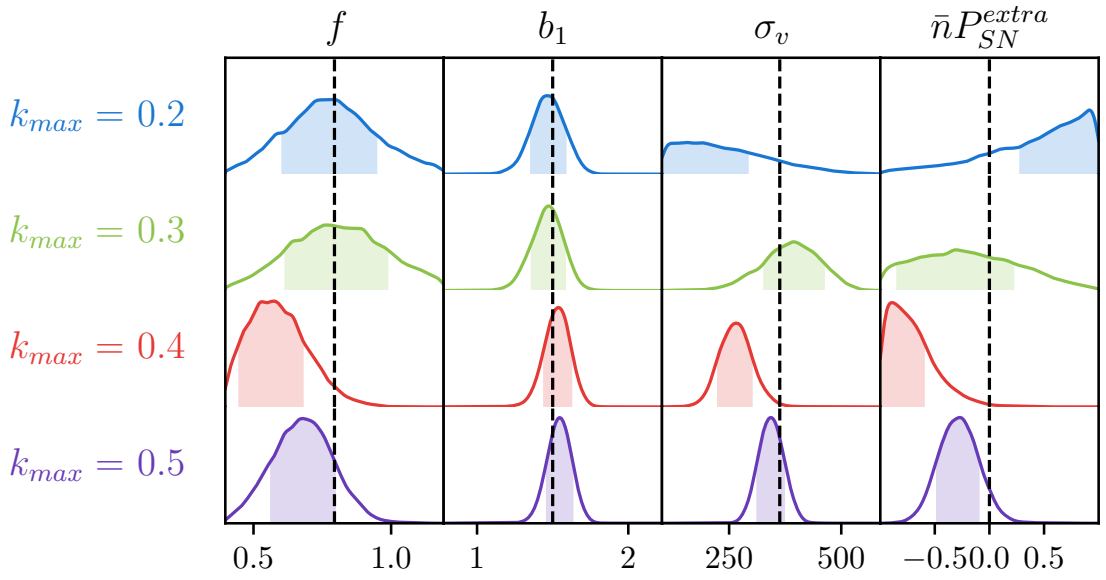


**Figure 5.5:** Posterior on the constrained parameters using the $z_1$ redshift slice of the $W_1$ observation field of the VIPERS survey, and varying the maximum wavenumber up to which we extend the analysis. The dashed lines in this plot represent the $\Lambda$-CDM prediction for $f$, and for the other parameters, they are simply the best-fit parameters for the mocks. One can see that there seem to be no significant tendencies on these posteriors up to $k_{\rm max} = 0.6[h/{\rm Mpc}]$, when one can see an important shift in the bias. In order to take a conservative position, we choose to use values only up to $k_{\rm max} = 0.3[h/{\rm Mpc}]$, as this is already well beyond the usual limit predicted by PT.

## 5.6 Analysis of the Data

We now turn ourselves to presenting the analysis of the VIPERS dataset using the developed pipeline. As a first test to understand whether the results which we found for the mocks are also valid for the data, we repeat this analysis varying $k_{\rm max}$, trying to identify whether there are any tendencies in the recovered parameters which may indicate a deviation due to a failure in the modelling. Figure (5.5) shows the recovered posteriors on these parameters for each of the values of maximum wavenumbers; one can see that the results are very similar, with the posteriors presenting a tendency to drift off for wavenumbers larger than $0.3[h/{\rm Mpc}]$, but well controlled below this value, indicating that the systematical errors are still not relevant enough to introduce a large shift in this parameter. Based on these analyses, we decide to use measurements of the power spectrum up to $k_{\rm max} = 0.3[h/{\rm Mpc}]$. In this section, as in the previous one, we will show in detail only the results for the $z_1$ redshift slice of the $W_1$ field, and the figures for the other redshift slices can be seen in the appendices.

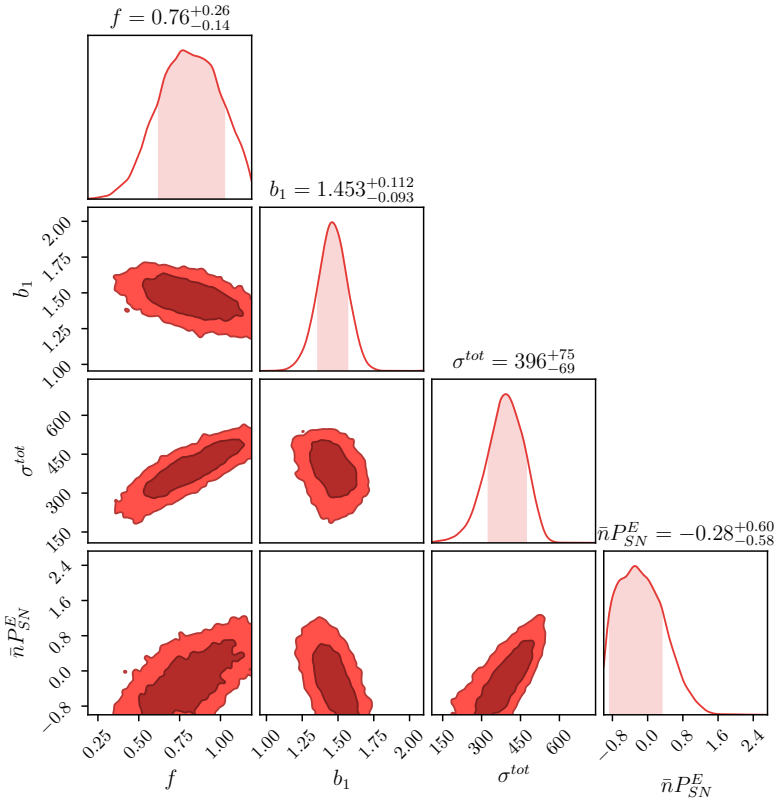


**Figure 5.6:** Constraints obtained on $f$ and nuisance parameters using monopole and quadrupole of the power spectra obtained from the $z_1$ redshift slice of the $W_1$ observation field of the VIPERS survey.

Figure (5.6) shows the constraints obtained for the $z_1$ redshift slice of the $W_1$ observation field using the monopole and quadrupole of the power spectrum up to $k_{\text{max}} = 0.3[h/\text{Mpc}]$, and figure (5.7) shows the comparison of the model computed at the best fit parameter values and the measured spectra. The values of $f\sigma_8$ for each of the three redshift slices, their associated errors, and reduced chi-squared values can be seen in table (5.1); moreover, in figure (5.8) we plot these constraints on a diagram of $z$ by $f\sigma_8$, next to the main relevant constraints on this quantity obtained up to date. These constraints show no relevant tension with the $\Lambda$-CDM prediction for $f\sigma_8(z)$, computed with the best-fit cosmology from Hinshaw et al., 2013, and are also well in agreement with previous measurements of $f\sigma_8(z)$ obtained from VIPERS data by Pezzotta et al., 2017.

Although the parameters $b_1$, $\sigma_v$ and $\bar{n}P^E_{SN}$, called *nuisance* parameters, are not of our direct interest, their constrained values may indicate possible deficiencies of our modelling, or shifts in the properties of galaxies. As $z$ increases, there is a clear growth

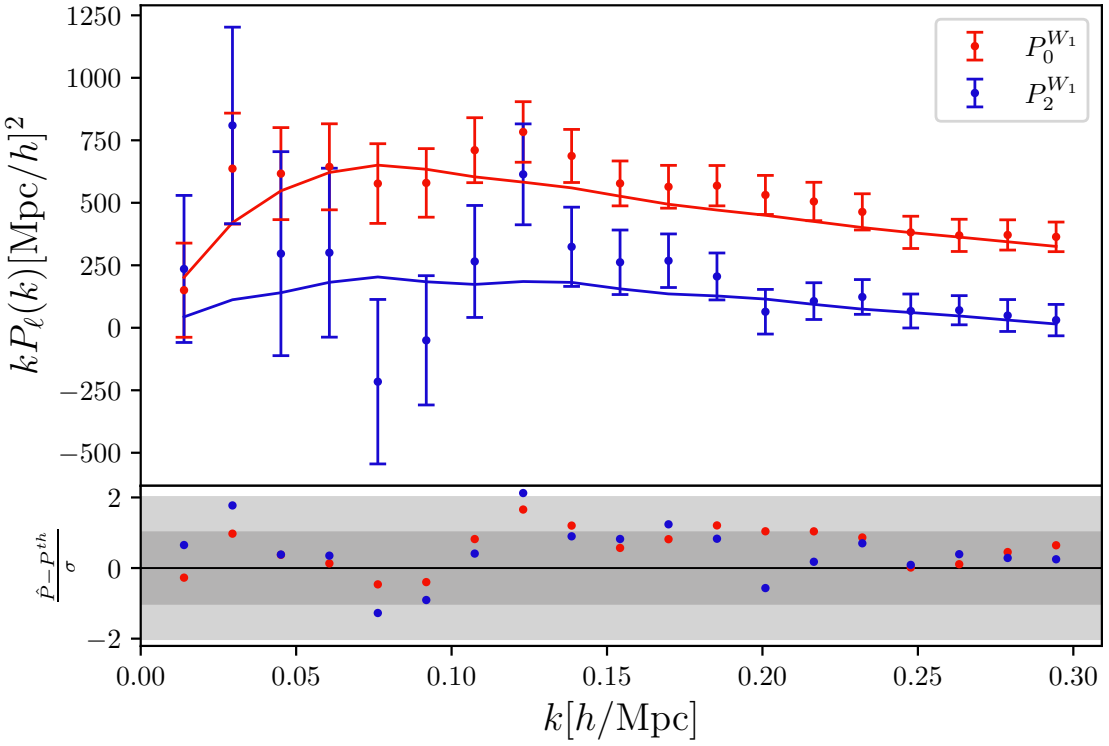


**Figure 5.7:** Measurements of the monopole and quadrupole from the $z_1$ redshift slice of the $W_1$ observation field of the VIPERS survey are represented by points with error bars. The model computed with the best fit set of parameters, obtained using $k_{\mathrm{max}} = 0.3[h/\mathrm{Mpc}]$ is represented by the solid lines. The reduced chi-squared for this fit is given by $\chi^2_{\mathrm{red}} = 1.44$. The general agreement between model and data is good, and the reduced chi-squared value indicates a good fit.

tendency of the linear bias parameter, $b_1$; the VIPERS survey observes galaxies only up to values of apparent magnitude $i_{AB} < 22.5$, therefore, when one goes to higher values of redshifts, the galaxies which will satisfy this condition will have progressively larger *absolute magnitudes*, and it is a known fact that these will have larger biases. It is also interesting to notice that, for $z_1$ and $z_2$ the extra shot-noise term is consistent with $0$, indicating that the mean density of these slices has been well estimated; however, for $z_3$ one can see that this is no longer the case, and the extra shot-noise prefers a value of $0.91$, clearly indicating that our modelling of shot-noise is insufficient. The data shows a larger shot-noise than the subtracted value of $\frac{1}{\bar{n}}$, and therefore, the model attempts to compensate for this, summing a large contribution to the model; a possibility to explain this deficiency of the model is that the assumption that shot-noise is Poissonian is no longer valid for a tracer with such a low number density, as are the galaxies in the $z_3$ slice, and more sophisticated models should be used. It can also be conjectured that this increased shot-noise

| | $z_{eff}$ | $z$ | $f\sigma_8(z_{eff})$ | $\chi^2_{\text{red}}$ |
|---|---|---|---|---|
| $z_1$ | 0.625 | $0.55 \leq z \leq 0.7$ | $0.45^{+0.15}_{-0.08}$ | 1.44 |
| $z_2$ | 0.8 | $0.7 \leq z \leq 0.9$ | $0.53^{+0.10}_{-0.15}$ | 1.31 |
| $z_3$ | 1.0 | $0.9 \leq z \leq 1.1$ | $0.48^{+0.10}_{-0.12}$ | 1.05 |

**Table 5.1:** Values of the constraints on $f\sigma_8(z)$ for each of the redshift slices, and values of reduced chi-squared for these fits.

is due to the manifestation of the $1-$halo term; Abramo et al., 2015 has shown that the 1-halo term scales much faster with $b_1$ than the 2-halo term, and therefore, it could be that for this redshift slice it becomes large enough to be relevant at scales $k \sim 0.3[h\text{Mpc}^{-1}]$.

This pipeline has been tested for possible biases, and used to constrain cosmological parameters, without presenting significant issues. Therefore, the next step is to do a slight generalization, enabling it to deal with multiple tracers of the density field. This has in fact already been done, but the set of galaxy mocks for the VIPERS survey which we had been using showed inconsistencies with the data when we separated them into different populations by absolute magnitude; this delayed the multi-tracer analysis, and for this reason we could not present it in this work. In the near future we will once again apply this pipeline to the VIPERS data set, estimating the power spectrum multipoles both with FKP and MTOE, and compare their constraints to decide on the relevance of the improvement brought by the latter.

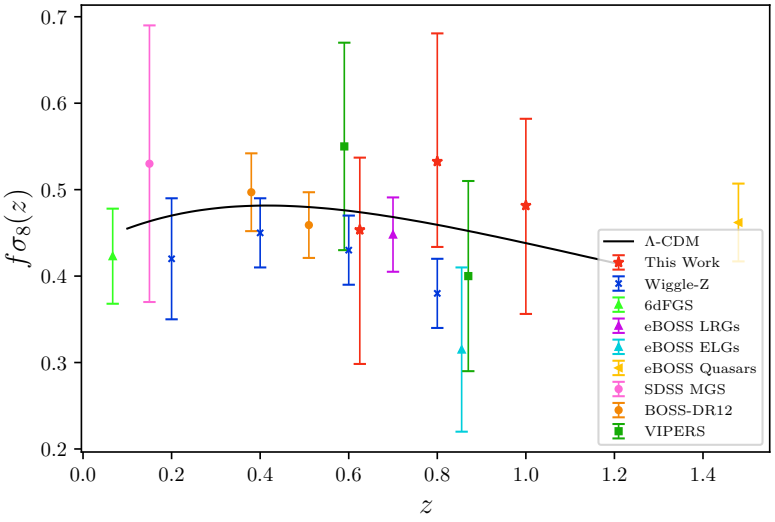


**Figure 5.8:** Constraints on the matter growth-rate from most relevant recent observation campaigns, and from this work. The latter are shown in red stars for the effective redshifts of 0.625, 0.8 and 1.0.

# Chapter 6

# Fixed and Paired Simulations

Stage IV galaxy surveys such as Euclid[1], Dark Energy Spectroscopic Instrument (DESI)[2], Javalambre Physics of the Accelerated Universe Astrophysical Survey (J-PAS)[3], Prime Focus Spectrograph survey (PFS)[4], or Legacy Survey of Space and Time (LSST)[5] are expected to give an unprecedented amount of data over the next decade, shrinking the current error bars to a fraction of their values, and possibly uncovering flaws of the $\Lambda$-CDM models or new cosmological phenomena. In order to take advantage of this large amount of data, it is imperative to have very accurate and precise theoretical models; N-Body simulations are arguably the most accurate theoretical tool available, especially in the non-linear regime of structure formation. Therefore, it would be very desirable to use the power of these predictions to constrain cosmological parameters.

Integrating these simulations into analysis pipelines is currently not possible due to their prohibitive computational cost. Recent works have been tackling this question by using machine-learning techniques to reduce the time necessary in accessing these predictions (Heitmann et al., 2013; Lawrence et al., 2017; Zennaro et al., 2021; Kokron et al., 2021). Using a set of simulations ran at strategical points of parameter space, one can interpolate over their predictions to produce very precise emulators of statistical

[1] https://www.euclid-ec.org
[2] https://www.desi.lbl.gov/
[3] http://www.j-pas.org/
[4] https://pfs.ipmu.jp/
[5] https://www.lsst.org/

quantities such as the power spectrum and bispectrum (Angulo and White, 2010; Angulo et al., 2020). The cost associated with evaluating the model is reduced by several orders of magnitude, making it possible to integrate accurate $n$-point function predictions into algorithms that sample the posterior probability distribution of a certain dataset.

Although the accuracy of N-Body simulations is unmatched in the non-linear regime, perturbation theory (PT) is also extremely accurate in the linear regime, with the advantage of having no variance at all, whereas quantities derived from N-Body simulations will have large variances at small $k$ due to being sampled from a small number of modes. An interesting approach is to combine these tools to obtain $n$-point functions which are both exact in large scales and extremely accurate in small scales. To do that one must define a scale $k^*$ at which the transition between them will take place (Kokron et al., 2021; Zennaro et al., 2021; Hadzhiyska et al., 2021); the choice of this scale involves a trade-off between the model error in PT, which grows as $k^*$ increases, and the variance in N-Body spectra which gets larger as $k^*$ decreases. This makes it clear that, even substituting the large scales by perturbation theory, it is still highly desirable to reduce the variance in statistical quantities from N-Body simulations, to be able to push $k^*$ to smaller values, thus avoiding model error without compromising precision.

Both PT and N-Body simulations will give us predictions for $n$-point functions of the dark-matter field, and we have, up to now, omitted the discussion of how to connect this with the observed galaxy quantities. Schmittfull et al., 2019; Modi, Chen, and White, 2020 have shown that performing the bias expansion in Lagrangian space and then evolving the obtained tracer spectra into Eulerian space allows one to reproduce well quantities measured from simulated halo or galaxy catalogs, at the expense of having to compute 15 auto and cross spectra between different dark-matter density fields

$$P_{gg} = \sum_{i,j\in[1,\delta,\delta^2,s^2,\nabla^2\delta]} b_i b_j P_{ij}. \tag{6.1}$$

Thus, it is these auto and cross spectra which must be obtained from the combination of PT and N-Body simulations, evaluating the trade-off between model error and simulational variance, as discussed in the previous paragraphs.

One way to reduce the variance in the simulation spectra was introduced by Angulo and Pontzen, 2016. The procedure consists of two steps; the first is to generate initial conditions with amplitudes fixed to their fiducial values $\delta(k) = \sqrt{L^3 P(k)} e^{i\theta}$, thus reducing the level of randomness while maintaining the matter power spectrum unbiased. Secondly, one combines two such simulations with the same initial seed, but displacing the phases of one of them by $\pi$, or equivalently, generating it with opposite initial conditions $\delta(k) = -\sqrt{L^3 P(k)} e^{i\theta}$. This will have the effect of averaging over the fluctuations in $n$-point functions generated by a particular seed of the random phases, making it converge to the mean much faster. Although Villaescusa-Navarro et al., 2018 and Klypin, Prada, and Byun, 2020 investigated a wide range of statistics derived from paired-fixed simulations, finding that they are unbiased, such results have never been presented for the auto and cross-spectra of equation (6.1); it is also unclear from previous results whether these spectra will present any reduction to their variance.

Fixing and pairing has been shown to drastically reduce the variance in certain statistical quantities, without biasing them (Angulo and Pontzen, 2016; Villaescusa-Navarro et al., 2018; Klypin, Prada, and Byun, 2020); a side-effect of this procedure is that we no longer know the value of the variance, only that it is smaller. Therefore, a theoretical prediction of the variance in fixed and paired simulations would be very useful; in the specific case discussed above, one could use it to choose the transition scales $k^*_{ij}$ needed to obtain a desired precision, before running any simulations at all. This would allow one to tailor simulation sizes to a specific need, perhaps saving many computational resources, or simply enabling better planning for future simulation runs.

The achievements of this chapter can be resumed into three points: (i) we show that the auto and cross-spectra entering the bias expansion are unbiased when computed from fixed and paired simulations; (ii) using Lagrangian Perturbation-Theory we obtain analytical expressions for the variance in fixed and paired spectra for the first time. This enables the understanding of why certain spectra have their variance reduced in fixed and paired simulations, while others do not. Finally, we compare these calculations to results from numerical simulations, showing a remarkable agreement.

## 6.1 Fixed and Paired Fields

In this section we give a brief overview to contextualize fixed and paired fields, and also to settle on the notation to be used throughout this work.

Let us say $\rho(\mathbf{x})$ is the density of dark matter, then we can define the matter overdensity field as $\delta(\mathbf{x}) = \frac{\rho(\mathbf{x})}{\bar{\rho}} - 1$. It is customary to work with its Fourier transform, defined by

$$\delta(\mathbf{k}) = \int d^3\mathbf{x}\delta(\mathbf{x})e^{-i\mathbf{k}\cdot\mathbf{x}}. \tag{6.2}$$

This field will be complex, and therefore can be decomposed into an amplitude and a phase, $\delta(\mathbf{k}) = |\delta(\mathbf{k})|e^{i\theta_\mathbf{k}}$; due to $\delta(\mathbf{x})$ being real, these fields must satisfy $\delta^*(\mathbf{k}) = \delta(-\mathbf{k})$ and consequently $\theta_{-\mathbf{k}} = -\theta_\mathbf{k}$. One can in general define the power spectrum of this field through the expression

$$\langle\delta(\mathbf{k})\delta(\mathbf{k}')\rangle = (2\pi)^3\delta_D(\mathbf{k}-\mathbf{k}')P(k), \tag{6.3}$$

in which we express the power spectrum directly as depending only on the modulus of the wave vector due to the assumption of isotropy in the density field. In the case of a numerical simulation with finite volume $L^3$ the power spectrum can be defined as

$$P(\mathbf{k}) = V_f\delta(\mathbf{k})\delta(-\mathbf{k}), \tag{6.4}$$

in which $V_f = \frac{(2\pi)^3}{L^3}$, and isotropy is only valid in the limit of $L^3 \to \infty$, so in order to obtain $P$ as a function of the modulus of the wave-vector, one must average over a spherical shell of radius $k_i$ and width $\delta k$,

$$P(k_i) = \frac{1}{V_s(k_i)}\int_{\hat{\mathbf{k}}_i}\frac{d^3\mathbf{k}}{(2\pi)^3}P(\mathbf{k}), \tag{6.5}$$

in which $V_s(k_i) = 4\pi k_i^2\delta k = 4\pi k_i^3\delta\ln k$, depending on whether one uses linear or logarithmic binning of the wave-modes, and $\int_{\hat{\mathbf{k}}_i}$ is an integral over $V_s(k_i)$.

Observations of the cosmic microwave-background (CMB) (Aghanim et al., 2020) have shown that perturbations in the early universe were, to a very good approximation,

gaussianly distributed. This can be expressed equivalently by saying that the absolute values of the Fourier modes follow a Rayleigh distribution, and the phases are uniformly distributed in the interval $[0, 2\pi]$, resulting in a combined distribution given by

$$\mathcal{P}(|\delta(\mathbf{k})|, \theta_{\mathbf{k}}) = \frac{|\delta|}{\pi L^3 P} e^{-|\delta|^2/L^3 P}. \tag{6.6}$$

Therefore, the standard procedure to generate initial conditions for cosmological simulations is to sample this distribution for amplitudes and phases, using the linear power spectrum at high redshift in the place of $P$. To generate fixed simulations, in contrast, one substitutes this probability density function by a Dirac delta centered at $\sqrt{V_f^{-1} P(\mathbf{k})}$, that is,

$$\mathcal{P}^f(|\delta|(\mathbf{k})|, \theta_{\mathbf{k}}) = \frac{1}{2\pi} \delta_D \left( |\delta| - \sqrt{V_f^{-1} P} \right), \tag{6.7}$$

which amounts to fixing all the amplitudes to the value $|\delta(\mathbf{k})| = \sqrt{V_f^{-1} P(\mathbf{k})}$ while allowing the phases to be uniformly sampled between $0$ and $2\pi$. From this initial density field, $\delta_1(\mathbf{k}) = |\delta(\mathbf{k})| e^{i\theta_{\mathbf{k}}}$, one can easily generate its corresponding pair simply by displacing the phases of $\pi$, $\delta_2(\mathbf{k}) = |\delta(\mathbf{k})| e^{i(\theta_{\mathbf{k}} + \pi)}$. Fixing clearly reduces the level of randomness in the field, while destroying its gaussianity. Nevertheless, Villaescusa-Navarro et al., 2018 has done an extensive study of many statistical quantities derived from fixed and paired simulations, finding that none are biased; the matter power spectrum and bispectrum had already been demonstrated to be unbiased by Angulo and Pontzen, 2016.

## 6.2 Simulations

To perform our analyses we have used two different sets of simulations. The first is an ensemble of 100 2LPT simulations; these were used mainly to validate our theoretical calculations of the variances for the basis spectra. The second is an ensemble of 100 L-PICOLA simulations, used for comparing Gaussian and fixed and paired spectra, and for understanding up to which scales our theoretical predictions are valid; both sets were run with the cosmological parameters resumed in table (6.1), for Gaussian and fixed initial conditions, and for phase offsets $\phi = 0, \pi$. The original L-PICOLA code developed by Howlett, Manera, and Percival, 2015 did not include an option for fixing, and therefore,

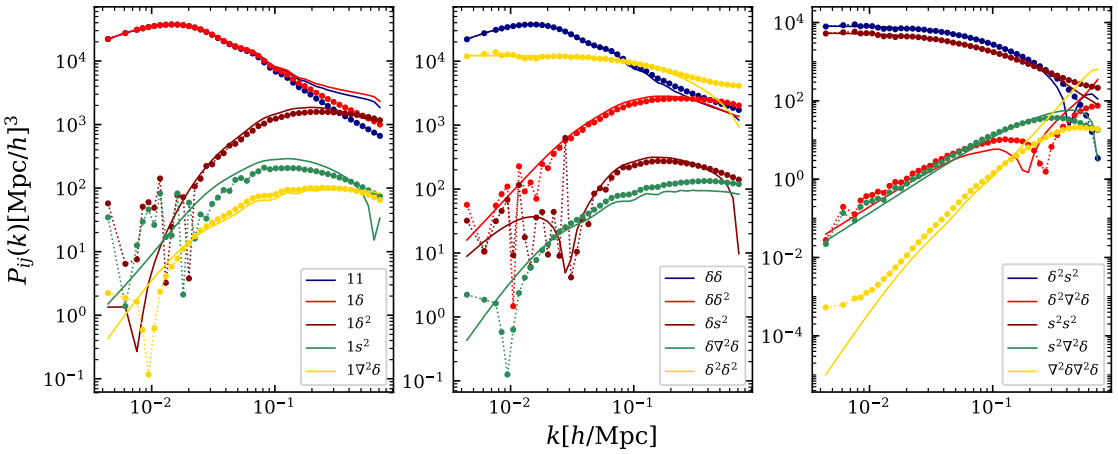


**Figure 6.1:** Basis spectra entering the Lagrangian bias expansion, advected to Eulerian space. Solid lines represent theoretical calculations using second-order LPT, and dots represent the mean of these spectra measured from a set of 100 L-PICOLA simulations.

minor modifications had to be done to it. The 2LPT code is a part of the Bacco project.

In order to measure the basis spectra entering equation (6.1) we took the following procedure:

1. Generate initial conditions with the same seed and phase offset as the simulation to be analyzed;

2. Use this generated field to compute $\delta(\mathbf{q}), \delta^2(\mathbf{q}), s^2(\mathbf{q})$ and $\nabla_q^2\delta(\mathbf{q})$ in Lagrangian space;

3. Compare the initial positions of the particles to their positions at the desired redshift, thus obtaining their displacement $\psi_i = \mathbf{x}_i(z_{final}) - \mathbf{x}_i(z_{init})$;

4. Advect the quantities from Lagrangian to Eulerian space using the expression

$$F(\mathbf{x}) = \int d^3\mathbf{q} F(\mathbf{q}) \delta_D(\mathbf{x} - \mathbf{q} - \psi(\mathbf{q})); \tag{6.8}$$

5. Compute their auto and cross-spectra using the fields obtained in Eulerian space. For the paired spectra we then average over the two simulations run with the same seed, but different phase offsets.

The mean of these spectra is shown in figure (6.1), along with theoretical predictions

| | |
|---|---|
| $\Omega_m$ | $0.25$ |
| $\Omega_b$ | $0.045$ |
| $\Omega_\Lambda$ | $0.75$ |
| $h$ | $0.73$ |
| $\sigma_8$ | $0.90$ |
| $n_s$ | $0.96$ |
| $L$ | $1.5$ Gpc$/h$ |
| $z_i$ | $9$ |

**Table 6.1:** Cosmological parameters used to run the ensemble of LPT and L-PICOLA simulations used in this work.

obtained using 2LPT.

## 6.3 Bias and Variance Reduction

In this section we use L-PICOLA simulations to numerically assess by how much does pairing and/or fixing reduce the variance in the basis spectra, and whether these spectra are unbiased compared to the ones obtained using Gaussian initial conditions. To do that we compute the mean and variance of these spectra,

$$\langle P_{ij} \rangle = \frac{1}{N} \sum_{l=1}^{N} P_{ij,l}, \tag{6.9}$$

$$\sigma_{ij}^2 = \frac{1}{(N-1)} \sum_{l=0}^{N} \left( P_{ij,l} - \langle P_{ij} \rangle \right)^2 . \tag{6.10}$$

Notice, however, that equation (6.10) gives the variance of one simulation, and we must further divide it by $N$ to get the variance of the mean. We will label spectra derived from fixed, paired, fixed and paired, and Gaussian simulations respectively by $P^f$, $P^p$, $P^{fp}$, $P^g$, and all of the other quantities accordingly.

Using the simulation results, we estimate the bias of fixed and paired simulations

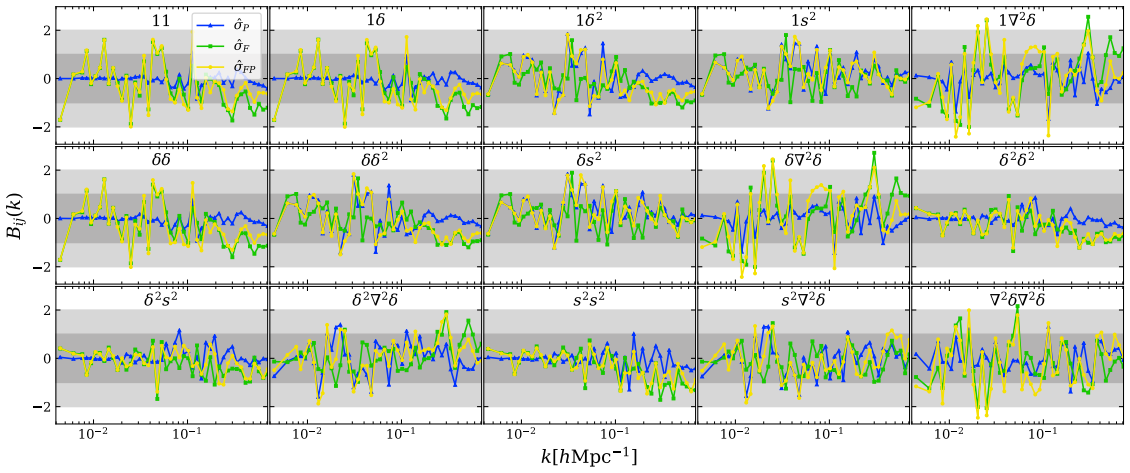


**Figure 6.2:** Differences of fixed and/or paired spectra to Gaussian ones, divided by the expected standard deviation of this difference. These plots indicates clearly that there are no significant biases in these spectra, since these differences generally remain inside the 1 or 2-$\sigma$ region. Notice how in general it may seem like the paired spectra are much less biased; however, this is simply an effect of its variance being much larger, and therefore the ratio is a lot smaller.

with respect to Gaussian ones through the expression

$$B_N^{fp} = \frac{\langle P^{fp} \rangle_N - \langle P^G \rangle_N}{\sigma_N^{fp-G}}, \tag{6.11}$$

in which $\langle P^{fp} \rangle_N$ is the average of $N$ fixed and paired simulations, and analogously for $\langle P^G \rangle_N$; $\sigma_N^{fp-G}$ is the expected error in their difference, defined by the expression

$$\sigma_{fp-G} = \sqrt{\left[\sigma_N^{fp}\right]^2 + [\sigma_N^G]^2}. \tag{6.12}$$

The standard deviations $\sigma_N^{fp}$ and $\sigma_N^G$ are the expected errors on the average of $N$ spectra, defined by

$$\left[\sigma_N^{fp}\right]^2 = \frac{1}{n-1} \sum_{i=1}^{n} \left( \langle P^{fp} \rangle_{N_i} - \langle P^{fp} \rangle \right)^2, \tag{6.13}$$

$n$ being the number of independent sets of $N$ spectra available. In figure (6.2) we show the results for the computation of these biases from 20 sets of 5 simulations; it is not hard to see that, for all of the 15 basis spectra, no significant bias can be detected, as most of the points are located inside the $1$ or $2-\sigma$ region, represented by gray-shaded areas in the figure.

To quantify the statistical improvement derived from fixing we directly take the ra-

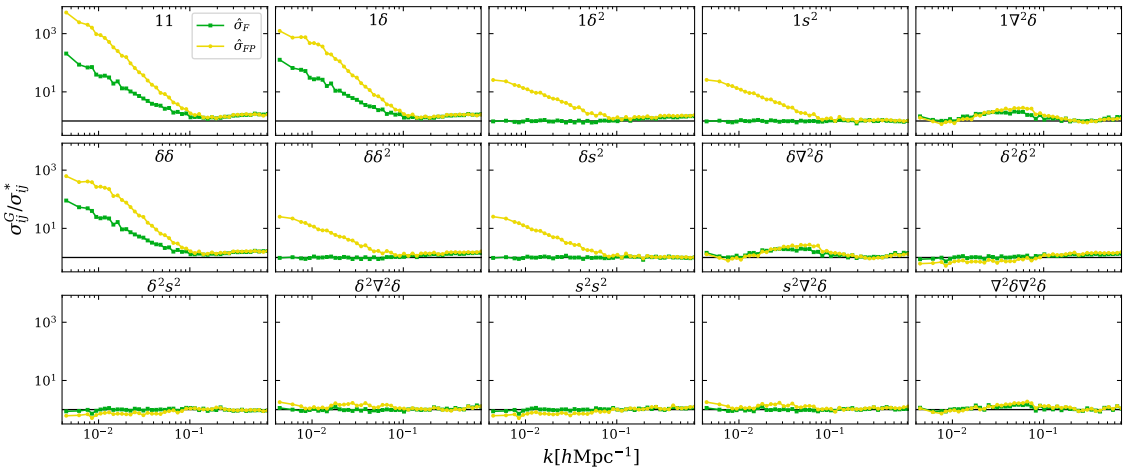


**Figure 6.3:** Ratio of the standard-deviation in fixed and/or paired spectra to the same quantity for standard spectra. One can see what are the effects of fixing and/or pairing in the variances for these spectra. These computations were carried out using a set of 100 L-PICOLA simulations.

tio between the variances of fixed and Gaussian spectra, $\frac{\sigma_G}{\sigma_f}$. Quantifying the statistical improvement coming from pairing is slightly more delicate. Paired spectra are obtained from the average of two simulations with same seed, but opposite phases; if they were uncorrelated, then the variance would be divided by 2, in a well known result. Of course, this would not be much of an improvement, since we could just have run an additional simulation, with a different seed, to get the same effect; the interesting case is when, due to having opposed phases, these simulations are anti-correlated, and their fluctuations around the mean will cancel out making the spectra converge to the mean much faster. Therefore, we choose to multiply the variance of paired simulations by 2 before comparing them to the other ones, to avoid seeing the effects of simply taking an average over two simulations. A side effect to this, is that, for some spectra, their measurements from the two simulations are highly correlated, so that the second simulation adds almost no information, giving only a small reduction in variance from taking their average; multiplying it by 2, can then make it artificially larger than the variance of the non-paired spectra, which does not mean that pairing worsened the variance, but only that the second simulation did not add new information, and thus running it was a waste of energy.

Figures (6.3), (6.4), and (6.5) show analyses assessing the variance reductions from fixing and/or pairing, using simulations run with L-PICOLA, 1LPT and 2LPT, respectively. It is useful to divide these spectra into four categories to best understand the reduc-

tion in variance:

- Spectra involving two linear fields, $P_{11}, P_{1\delta}, P_{\delta\delta}$; for scales $k \lesssim 0.1[h\text{Mpc}^{-1}]$, fixing gives a large reduction in $\sigma$ for these spectra, of a factor of around $\mathcal{O}(10^2)$. Pairing further reduces it by a factor of $\mathcal{O}(10)$, and the upshot is a final reduction of $\mathcal{O}(10^3)$. For scales $k \gtrsim 0.1$, we see a small improvement from fixing, which reduces the $\sigma$ by a factor of $\sim 2$.

- Spectra involving one linear and one squared field, $P_{1\delta^2}, P_{1s^2}, P_{\delta\delta^2}, P_{\delta s^2}$; for scales $k \lesssim 0.1[h\text{Mpc}^{-1}]$ fixing gives no benefit at all for these spectra, but pairing reduces $\sigma$ by a factor of $\mathcal{O}(10)$. For scales $k \gtrsim 0.1$, we see a slight improvement from fixing, which reduces $\sigma$ by a factor $\sim 1.5$.

- Spectra involving two squared fields $P_{\delta^2\delta^2}, P_{\delta^2 s^2}, P_{s^2 s^2}$; for these spectra we see no improvement from fixing or pairing.

- Spectra involving the laplacian field; the laplacian field displays a behaviour similar to that of linear fields, in the sense that, when it is combined with a linear field such as $1$ or $\delta$, it displays a large variance reduction for fixing, and a smaller one for pairing. Moreover, when combined to a squared field such as $\delta^2$ or $s^2$, it shows no variance reduction from fixing, but substantial reduction from pairing. However, we did not include it into that category because these reductions are much smaller than for the auto and cross spectra actually computed from linear fields. Furthermore, the results which we find seem to depend on the type of simulations used. For 1LPT simulations we see a result which resembles that of the first category, but for 2LPT simulations one can already see a smaller reduction in variance; for the L-PICOLA simulations this becomes even more nitid, as one can see only a mild reduction in variance at intermediate scales of $k \sim 0.05[h\text{Mpc}^{-1}]$.

In the next section we will compute these variances analytically and provide simple explanations to these classes of behaviours.

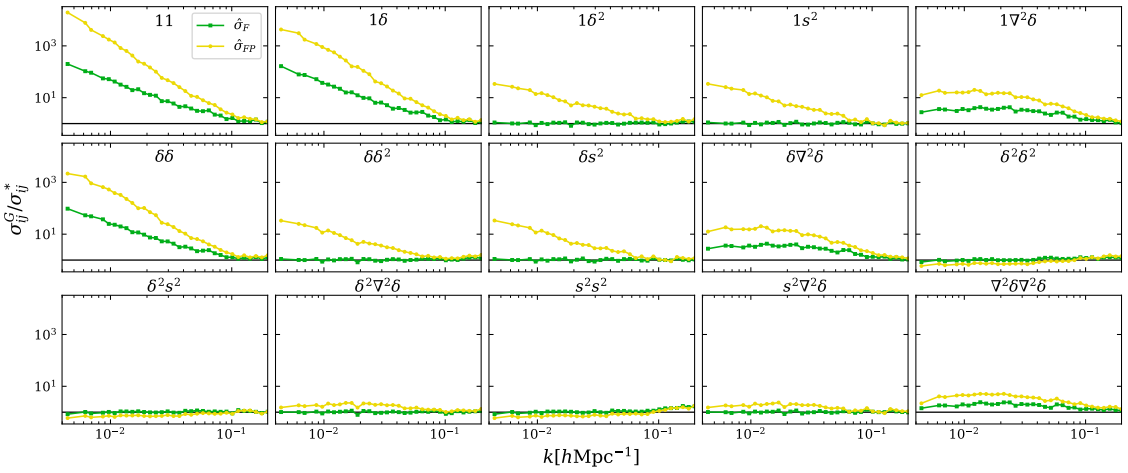


**Figure 6.4:** Ratio of the standard deviation in fixed and/or paired spectra to the same quantity in Gaussian spectra. These computations were carried out using a set of 100 1-LPT simulations. One can see small, but perceptible, differences from this plot to figure (6.3), mainly in the ratios for spectra containing the laplacian term, which in this case present a larger reduction in variance from fixing and/or pairing. Notice how, unlike in figure (6.3), the maximum value of $k$ represented in this plot is of $0.2[h\mathrm{Mpc}^{-1}]$; it is important to stop at this wavemode, because LPT simulations do not converge for $k$ values larger than this.

## 6.4 Theoretical Predictions

In order to make predictions for the variance of the basis spectra that go into equation (6.1), we use the LPT formalism. Let us call $F(\mathbf{q})$ a field in lagrangian space such that $F(\mathbf{q}) \in [1, \delta, \delta^2, s^2, \nabla^2\delta]$, which one must advect into eulerian space. This can be achieved with the following expression,

$$F(\mathbf{x}) = \int d^3\mathbf{q} F(\mathbf{q}) \delta_D(\mathbf{x} - \mathbf{q} - \boldsymbol{\psi}(\mathbf{q})) \tag{6.14}$$

meaning that the field $F$ in eulerian space will be the summation of the lagrangian field evaluated at all positions $\mathbf{q}$ satisfying $\mathbf{q} + \psi(\mathbf{q}) = \mathbf{x}$. Taking the Fourier transform of both sides, and expanding the displacement to second order in perturbation theory we obtain

$$\begin{aligned} F(\mathbf{k}) &\approx \int d^3\mathbf{q} e^{-i\mathbf{k}\cdot\mathbf{q}} F(\mathbf{q}) e^{-i\mathbf{k}\left(\cdot\boldsymbol{\psi}^{(1)}(\mathbf{q}) + \boldsymbol{\psi}^{(2)}(\mathbf{q})\right)} \\ &\approx \int d^3\mathbf{q} e^{-i\mathbf{k}\cdot\mathbf{q}} F(\mathbf{q}) \left[1 - i\mathbf{k}\cdot\left(\boldsymbol{\psi}^{(1)} + \boldsymbol{\psi}^{(2)}\right) - \frac{(\mathbf{k}\cdot\boldsymbol{\psi}^{(1)})^2}{2}\right] \end{aligned} \tag{6.15}$$

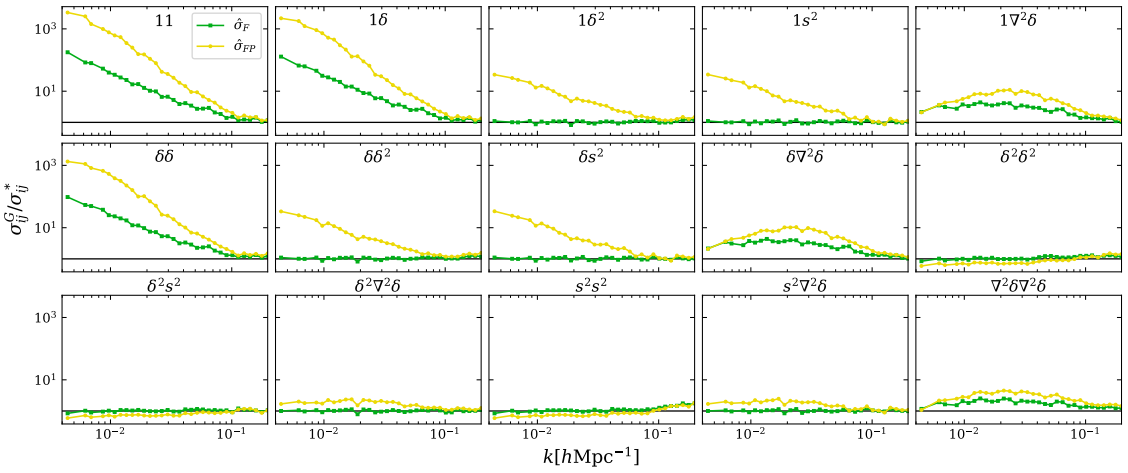


**Figure 6.5:** Ratio of the standard deviation in fixed and/or paired spectra to the same quantity in Gaussian spectra. These computations were carried out using a set of 100 2-LPT simulations. One can see small, but perceptible, differences from this plot to figures (6.3) and (6.4). The reduction in variance is clearly larger than what was seen for L-PICOLA, but smaller than for 1-LPT, indicating that higher order terms have a strong influence in this process. Notice how, unlike in figure (6.3), the maximum value of $k$ represented in this plot is of $0.2[h\mathrm{Mpc}^{-1}]$; it is important to stop at this wavemode, because LPT simulations do not converge for $k$ values larger than this.

in which going to the second line we simply Taylor expanded the exponential up to second order. One can then plug in the different fields into these expressions and crank the wheel to obtain them in eulerian space. The results of these calculations can be seen in appendix C.

With the expressions of $F(\mathbf{k})$ at hand, we can obtain the auto and cross power spectra of these fields through

$$\widehat{P}_{\mu\nu}(k_i) = V_f \,\mathrm{Re}\left[\delta_\mu(\mathbf{k})\delta_\nu(-\mathbf{k})\right]_{\Theta(k_i)}\,, \tag{6.16}$$

in which $\mu, \nu \in [1, \delta, \delta^2, s^2, \nabla^2\delta]$, $V_f = \frac{(2\pi)^3}{V}$, and the subscript $\Theta(k_i)$ indicates we are taking an average over a spherical shell of radius $k_i$. One can then combine these power spectra to obtain their covariance matrices through the expression

$$\mathrm{Cov}_{\mu\nu}(k_i) = \left\langle P_{\mu\nu}(k_i)P_{\mu\nu}(k_j)\right\rangle - \left\langle P_{\mu\nu}(k_i)\right\rangle\left\langle P_{\mu\nu}(k_j)\right\rangle\,, \tag{6.17}$$

in which

$$\langle P_{\mu\nu}(k_i)P_{\mu\nu}(k_j)\rangle = \frac{V_f^2}{V_s(k_i)V_s(k_j)}\int_{\hat{\mathbf{k}}_i}\frac{d^3\mathbf{k}}{(2\pi)^3}\int_{\hat{\mathbf{k}}_j}\frac{d^3\mathbf{k}'}{(2\pi)^3}\,\mathrm{Re}\,\langle\delta_\mu(\mathbf{k})\delta_\nu(-\mathbf{k})\delta_\mu(\mathbf{k}')\delta_\nu(-\mathbf{k}')\rangle\,. \tag{6.18}$$

We are now in position to substitute the relevant fields into equation (6.18) and determine their variances; for brevity, the actual calculations will be presented in appendix $D$, and in the remainder of this section we will give intuitive explanations of why the variances of the basis spectra respond to fixing and pairing in the way observed in figures (6.3), (6.4) and (6.5).

## 6.5 $P_{11}, P_{1\delta}, P_{\delta\delta}$

Using equations (C.4) and (C.12) one can easily obtain the expression for $P_{11}$, in the case of fixed initial conditions

$$\begin{aligned}P_{11}^F(\mathbf{k}) =& P_{\mathbf{k}}^L + \frac{1}{V_f^{1/2}}\int_{\mathbf{q}_1}\sqrt{P_{\mathbf{k}}^L P_{\mathbf{q}_1}^L P_{\mathbf{q}_1-\mathbf{k}}^L}\cos\left[\theta_{\mathbf{k}}-\theta_{\mathbf{q}_1}-\theta_{\mathbf{q}_1-\mathbf{k}}\right]\mathcal{K}_1(\mathbf{q}_1,\mathbf{k}-\mathbf{q}_1,\mathbf{k})\\ &+\frac{1}{4V_f}\int_{\mathbf{q}_1}\int_{\mathbf{q}_2}\sqrt{P_{\mathbf{q}_1}^L P_{\mathbf{k}-\mathbf{q}_1}^L P_{\mathbf{q}_2}^L P_{\mathbf{q}_2-\mathbf{k}}^L}\cos\left[\theta_{\mathbf{q}_1}+\theta_{\mathbf{k}-\mathbf{q}_1}-\theta_{\mathbf{q}_2}-\theta_{\mathbf{k}-\mathbf{q}_2}\right]\\ &\times\mathcal{K}_1(\mathbf{q}_1,\mathbf{k}-\mathbf{q}_1,\mathbf{k})\mathcal{K}_1(\mathbf{q}_2,\mathbf{k}-\mathbf{q}_2,\mathbf{k}).\end{aligned} \tag{6.19}$$

This expression is derived in detail, and further explained, in appendix D.

Notice here that the leading order contribution to this spectrum is the linear power spectrum, $P_{\mathbf{k}}^L$, and that, for the fixed case, this has no variance whatsoever; indeed, when we combined the two fixed fields, their phases cancelled completely, and since their amplitudes are fixed to the square root of the linear power spectrum, we obtain it completely free of noise. It is not hard to see that, for all spectra which have the linear power spectrum as their leading order term, fixing will greatly suppress their variance, by cancelling its leading order contribution. This is precisely the case of these spectra,

$$P_{11}, P_{1\delta}, P_{\delta\delta} \supset P^L, \tag{6.20}$$

explaining why fixing provides a large reduction in their variances.

The next to leading order contribution to $P_{11}$ is given by a term which came from the combination of three factors of $\delta^L$, and we will thus denote it schematically by $(\delta\delta\delta)$. Notice that we have not taken the expected value of this expression, otherwise this term would have gone to zero; this was done precisely to keep this kind of term, which is present in the numerical calculations of the spectra, but which would otherwise not appear in analytical calculations. Taking a closer look at the term $(\delta\delta\delta)$ we can see that, for a simulation which had all of its phases displaced by $\pi$, one would obtain

$$\begin{aligned}(\delta\delta\delta)_\pi =& \frac{1}{V_f^{1/2}}\int_{\mathbf{q}_1}\sqrt{P^L_{\mathbf{k}}P^L_{\mathbf{q}_1}P^L_{\mathbf{q}_1-\mathbf{k}}}\underbrace{\cos\left[\theta_{\mathbf{k}}-\theta_{\mathbf{q}_1}-\theta_{\mathbf{q}_1-\mathbf{k}}-\pi\right]}_{-\cos\left[\theta_{\mathbf{k}}-\theta_{\mathbf{q}_1}-\theta_{\mathbf{q}_1-\mathbf{k}}\right]}\mathcal{K}_1(\mathbf{q}_1,\mathbf{k}-\mathbf{q}_1,\mathbf{k}) \\ =& -(\delta\delta\delta).\end{aligned} \tag{6.21}$$

The pairing procedure consists precisely of creating two simulations with the same seed – but one of them with all the phases displaced by $\pi$ – and then average their spectra. Through the arguments above one can clearly see that this would cancel the $(\delta\delta\delta)$ from the spectrum, leaving us with

$$\begin{aligned}P^F_{11}(\mathbf{k}) =& P^L_{\mathbf{k}} + \frac{1}{4V_f}\int_{\mathbf{q}_1}\int_{\mathbf{q}_2}\sqrt{P^L_{\mathbf{q}_1}P^L_{\mathbf{k}-\mathbf{q}_1}P^L_{\mathbf{q}_2}P^L_{\mathbf{q}_2-\mathbf{k}}}\cos\left[\theta_{\mathbf{q}_1}+\theta_{\mathbf{k}-\mathbf{q}_1}-\theta_{\mathbf{q}_2}-\theta_{\mathbf{k}-\mathbf{q}_2}\right] \\ &\times\mathcal{K}_1(\mathbf{q}_1,\mathbf{k}-\mathbf{q}_1,\mathbf{k})\mathcal{K}_1(\mathbf{q}_2,\mathbf{k}-\mathbf{q}_2,\mathbf{k}).\end{aligned} \tag{6.22}$$

Although the explanation we gave was focused on the case of $P_{11}$, it is valid for the other two spectra, as all of these contain a term composed of three linear fields which has a completely analogous structure to the one described above, despite minor differences. Schematically, one can say that,

$$P_{11}, P_{1\delta}, P_{\delta\delta} \supset (\delta\delta\delta), \tag{6.23}$$

and therefore, all of these spectra have their variances greatly reduced by pairing.

## 6.6 $P_{1\delta^2}, P_{1s^2}, P_{\delta\delta^2}, P_{\delta s^2}$

From appendix D we can take the expression for the $P_{1\delta^2}$ spectra up to fourth order in $\delta^L$, for fixed initial conditions; this will be given by

$$\begin{aligned} P^F_{1\delta^2}(\mathbf{k}) =& \frac{1}{V_f^{1/2}} \int_{\mathbf{q}_1} \sqrt{P^L_{\mathbf{k}} P^L_{-\mathbf{q}_1} P^L_{\mathbf{q}_1-\mathbf{k}}} \cos\left[\theta_{\mathbf{k}} - \theta_{\mathbf{q}_1} - \theta_{\mathbf{k}-\mathbf{q}_1}\right] \\ &+ \frac{1}{V_f} \int_{\mathbf{q}_1} \int_{\mathbf{q}_2} \frac{\mathbf{k}\cdot(\mathbf{k}-\mathbf{q}_{12})}{|\mathbf{k}-\mathbf{q}_{12}|^2} \sqrt{P^L_{\mathbf{k}} P^L_{\mathbf{q}_1} P^L_{\mathbf{q}_2} P^L_{\mathbf{k}-\mathbf{q}_{12}}} \cos\left[\theta_{\mathbf{k}} - \theta_{\mathbf{q}_1} - \theta_{\mathbf{q}_2} - \theta_{\mathbf{k}-\mathbf{q}_12}\right] \\ &+ \frac{1}{2V_f} \int_{\mathbf{q}_1} \int_{\mathbf{q}_2} \mathcal{K}_1(\mathbf{q}_1, \mathbf{k}-\mathbf{q}_1) \sqrt{P^L_{\mathbf{q}_1} P^L_{\mathbf{k}-\mathbf{q}_1} P^L_{\mathbf{q}_2} P^L_{\mathbf{k}-\mathbf{q}_2}} \cos\left[\theta_{\mathbf{q}_1} + \theta_{\mathbf{k}-\mathbf{q}_1} - \theta_{\mathbf{q}_2} - \theta_{\mathbf{k}-\mathbf{q}_2}.\right] \end{aligned} \tag{6.24}$$

It is clear, then that

$$P_{1\delta^2}, P_{\delta\delta^2}, P_{1s^2}, P_{\delta s^2} \not\supseteq P^L, \tag{6.25}$$

and there will be none, or only very marginal, improvement to the variances of these spectra from fixing. Moreover, we see that the leading order term for this spectra is precisely of the shape $(\delta\delta\delta)$, allowing us to affirm

$$P_{1\delta^2}, P_{\delta\delta^2}, P_{1s^2}, P_{\delta s^2} \supset (\delta\delta\delta), \tag{6.26}$$

giving a clear explanation of why for this term, the fixing does not seem to give any relevant improvement, but pairing greatly reduces the variance.

## 6.7 $P_{\delta^2\delta^2}, P_{s^2s^2}$

Once again, we can take the expression for the $P_{\delta^2\delta^2}$ from appendix B, which will be given by

$$P^{F\&P}_{\delta^2\delta^2} = \frac{1}{V_f} \int_{\mathbf{q}_1} \int_{\mathbf{q}_2} \sqrt{P^L_{\mathbf{q}_1} P^L_{\mathbf{k}-\mathbf{q}_1} P^L_{\mathbf{q}_2} P^L_{\mathbf{k}-\mathbf{q}_2}} \cos\left[\theta_{\mathbf{q}_1} + \theta_{\mathbf{k}-\mathbf{q}_1} - \theta_{\mathbf{q}_2} - \theta_{\mathbf{k}-\mathbf{q}_2}\right]. \tag{6.27}$$

For these spectra, it is then clear how

$$P_{\delta^2\delta^2}, P_{s^2s^2} \not\supseteq P^L, \tag{6.28}$$

essentially justifying why we do not see any improvement in the variance due to fixing, and

$$P_{\delta^2\delta^2}, P_{s^2s^2} \not\supseteq (\delta\delta\delta), \tag{6.29}$$

showing that the pairing procedure does not help either with reducing the variance in the leading order term. It is not entirely clear why does fixing not reduce in any way the variance of these terms which involve the combination of four linear fields, but one may conjecture that the mode mixing is so intense that the nice structure imposed by the fixed initial conditions is destroyed, and the variance will be dominated by the noise in the phase field, which remains unchanged.

## 6.8 $P_{1\nabla^2\delta}, P_{\delta\nabla^2\delta}, P_{\delta^2\nabla^2\delta}, P_{s^2\nabla^2\delta}, P_{\nabla^2\delta\nabla^2\delta}$

Analytically, the behaviour of these terms would be very simple to derive, since in Fourier space one can write $\nabla^2\delta \rightarrow k^2\delta$. It is quite clear that, although multiplying $\delta$ by $k^2$ could change the kernels connecting the linear fields, it would not change the general structure of these terms, which should then behave as if the laplacian was a linear field. As stated earlier, this is not what we see, and most surprisingly, the behaviour of the variance reduction changes appreciably for 1LPT, 2LPT and L-PICOLA simulations. It is not yet clear whether these effects are a product of a lack of numerical resolution to which the laplacian would be exceedingly sensible; or perhaps for this field this series enters earlier into a non-perturbative regime, in which the higher-order terms will dominate even at large scales, therefore washing away the improvement to the variance which would have come at the leading order from fixing and pairing.

## 6.9 Testing Predictions

The preceding section developed a qualitative understanding on the behaviour of the variances for the basis spectra of the bias expansion in fixed and paired simulations. Now we wish to take a step further, providing quantitative predictions. The calculations described in detail in appendix D led us to relatively simple expressions for the variances of these spectra, which we then implemented computationally. Although in appendix D we have described these calculations up to second order in LPT, our implementation included only first order LPT.

In figure (6.6) one can see the theoretical calculations compared to the variances measured from sets of 1LPT, 2LPT, and L-PICOLA simulations. The first panel shows this comparison for the $P_{11}$ spectrum; notice how our calculation reproduces the general form, but is not able to capture the precise value of this variance. Remember that, for $P_{11}$, the leading order contribution to the variance was cancelled by fixing, and the next to leading order contribution was cancelled by pairing; therefore, the remaining terms are of high perturbative order, and our implementation keeping only first order LPT terms was not able to precisely reproduce the numerical results. The second and third panels show analogous comparisons, but now for $P_{1\delta^2}$ and $P_{\delta^2\delta^2}$, which can be well predicted by our calculations until scales of $k \sim 0.2[h\text{Mpc}^{-1}]$.

One of the main applications which we envisaged with this work is to be able to better define transition scales between simulation and theoretical spectra when building emulators for these quantities. This can clearly be done for the spectra $P_{1\delta^2}$ and $P_{\delta^2\delta^2}$, for which our predictions are sufficiently precise, and one would be able to compare the value of the standard-deviation with the expected model error at a certain scale. For $P_{11}$, further advancements are still necessary, since the predictions have important differences from the numerical results, which could lead to inaccurate conclusions.

However, this is currently extremely useful for better predicting the noise in spectra derived from galaxy mocks which were built upon fixed and paired dark-matter only simulations. Part of this noise will come from the process through which one populated halos with galaxies, part from shot-noise, and a relevant fraction will come from the noise in

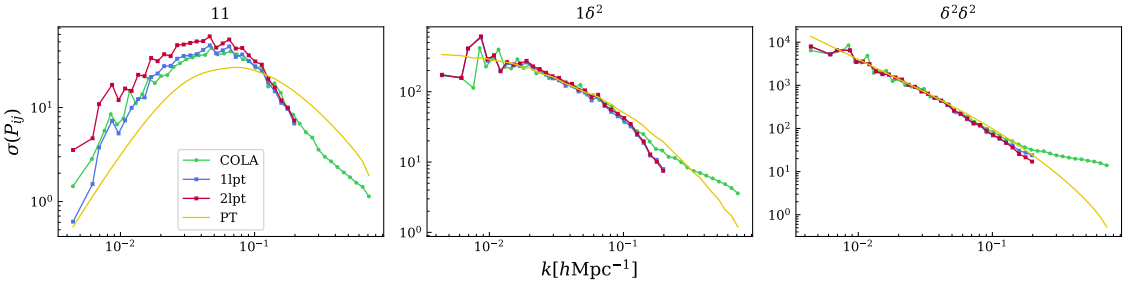


**Figure 6.6:** Comparison of the variances for fixed and paired spectra computed from simulations, and using our expressions derived from LPT. The yellow line represents the theoretical calculations, while the other three curves were computed from sets of 100 simulations using L-PICOLA, 1LPT and 2LPT. The so-called 1LPT simulations will generate an initial density field from an input power spectrum, compute the first order displacements, and then use them to advect the relevant density fields to Eulerian space; the same is true for the 2LPT simulations, only the displacements are computed up to second order.

the subjacent dark-matter field. Therefore, in order to understand the actual error in these simulations, without having to run many of them and compute a sampling covariance, we can sum up all of these contributions which were computed theoretically. To understand how the variance in each spectrum will manifest itself in the variance of the galaxy spectrum, we use the bias expansion. It is not hard to see that the generalization of equation (6.1) for the variance will be

$$\begin{aligned}\sigma^2_{gg} = \sigma^2_{11} &+ b_1^2\left(2\sigma^2_{1\delta} + b_1^2\sigma^2_{\delta\delta} + 2b_2^2\sigma^2_{\delta\delta^2} + 2b_s^2\sigma_{\delta s^2} + 2b^2_{\nabla^2}\sigma^2_{\delta\nabla^2\delta}\right)\\ &+ b_2^2\left(2\sigma^2_{1\delta^2} + b_2^2\sigma^2_{\delta^2\delta^2} + 2b_s^2\sigma_{s^2\delta^2} + 2b^2_{\nabla^2}\sigma^2_{\delta^2\nabla^2\delta}\right)\\ &+ b_s^2\left(2\sigma^2_{1s^2} + b_s^2\sigma^2_{s^2s^2} + 2b^2_{\nabla^2}\sigma^2_{s^2\nabla^2\delta}\right)\\ &+ b^2_{\nabla^2}\left(2\sigma^2_{1\nabla^2} + b^2_{\nabla^2}\sigma^2_{\nabla^2\delta\nabla^2\delta}\right),\end{aligned} \tag{6.30}$$

and one can then use this expression to give predictions about the errors, updating it as one varies the values of the bias parameters attempting to fit them. It may seem like this will also not work due to the lack of precision in the determination of $\sigma_{11}$, but looking at figure (6.7) we can see that this variance is highly subdominant at roughly all the scales of interest, and the most important terms are in fact $\sigma_{1\delta^2}$, $\sigma_{\delta^2\delta^2}$ and $\sigma_{\delta^2 s^2}$, and for the first two, our predictions work very well until relatively small scales, at which shot-noise will begin to dominate.

Finally, another application for this result would be that of using equation (6.30) to

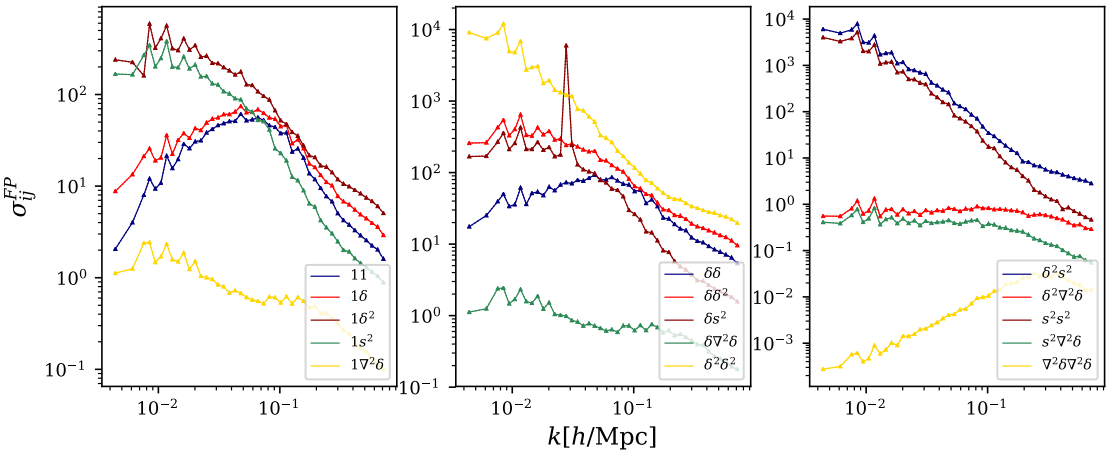


**Figure 6.7:** Plot of variances computed from an ensemble of 100 L-PICOLA simulations. Notice how, due to fixing and pairing, the spectra involving two linear fields have their variances highly suppressed, and therefore, it is the spectra such as $P_{1\delta^2}$ or $P_{\delta^2\delta^2}$ which will dominate the variance of a galaxy power spectrum built through the bias expansion.

predict the size of simulations which will be necessary to build models for upcoming surveys, e.g.: Euclid, DESI. By supposing a certain typical value for the bias parameters, and substituting the survey volume, one can quickly compute this expression, and find out the expected variance for a model of the galaxy power spectrum based on emulators completely built from numerical simulations. This would allow one to plan future simulation runs which will be necessary for the precise analysis of the upcoming data.

# Chapter 7

# Conclusions and Final Remarks

The prime realization of this work has been to develop a complete pipeline for the extraction of cosmological constraints from the effect of redshift-space distortions in galaxies. This was done with great control over systematical effects, and indeed, the tests performed on simulated data indicate that systematical errors are at least one order of magnitude smaller than the statistical errors in the observed spectra. It stands out that our model, although relatively simple, is able to recover unbiased values for the cosmological parameters, using wavemodes as large as $k_{max} = 0.3[h/\text{Mpc}]$. Although legitimate, this result seems to be true only in the specific case of the VIPERS survey, not being reported in the analysis of other spectroscopic surveys. Finally, we were able to produce constraints for the value of $f\sigma_8(z)$ which show no statistically relevant disagreement with the predictions of $\Lambda$-CDM.

Although these are not new results, as power spectrum analysis of the VIPERS survey had already been carried out (Rota et al., 2017; Wilson, 2016), it is extremely useful to have developed this machinery, to be used inside our research group. The machinery developed to forward-model the window-function of the survey into the theoretical model is completely general, and can be used to analyze data from any spectroscopic survey. With this pipeline it is straightforward to divide the VIPERS galaxies into multiple populations, estimate their spectra with FKP and MTOE, and compare the recovered constraints to perform the test of whether the latter does indeed provide smaller errors.

In a complementary fashion to this work, more focused on the observational aspects, interesting results were also derived concerning numerical simulations, using perturbation theory techniques. Through analytical calculations of the basis spectra that go into the bias expansion for the galaxy spectrum, we were able to provide simple and intuitive explanations for the behaviour of the variances for these spectra in fixed and paired simulations. Moreover, the analytical expressions which we obtained were capable of roughly describing $\sigma_{11}$, but predicting $\sigma_{1\delta^2}$ and $\sigma_{\delta^2\delta^2}$ to remarkable precision. We anticipate that this can be used to give better predictions for the variance in galaxy spectra derived from galaxy mocks built upon fixed and paired dark-matter only simulations; we also envisage applications of these results to better decide transition scales between perturbation theory predictions and numerical simulations in order to build emulators for power spectra; finally, this should also be useful to plan the simulation sizes necessary for accurate analysis of upcoming surveys.

# Bibliography


Abramo, L. R. and K. E. Leonard (2013). "Why multitracer surveys beat cosmic variance". In: *Monthly Notices of the Royal Astronomical Society* 432.1, 318–326.

Abramo, L. Raul (2012). "The full Fisher matrix for galaxy surveys". In: *Monthly Notices of the Royal Astronomical Society* 420.3, 2042–2057.

Abramo, L. Raul, Lucas F. Secco, and Arthur Loureiro (2015). "Fourier analysis of multitracer cosmological surveys". In: *Monthly Notices of the Royal Astronomical Society* 455.4, 3871–3889.

Abramo, L. Raul et al. (2015). "Scaling of the 1-halo terms with bias". In: *Monthly Notices of the Royal Astronomical Society* 454.3, 2844–2854.

Aghanim, N. et al. (2020). "Planck 2018 results". In: *Astronomy & Astrophysics* 641, A6.

Alam, Shadab et al. (2017). "The clustering of galaxies in the completed SDSS-III Baryon Oscillation Spectroscopic Survey: Cosmological analysis of the DR12 galaxy sample". In: *Monthly Notices of the Royal Astronomical Society* 470.3, pp. 2617–2652. arXiv: 1607.03155.

Alcock, Charles and Bohdan Paczyński (1979). "An evolution free test for non-zero cosmological constant". In: *Nature* 281, 358–359.

Angulo, R. E. and S. D. M. White (2010). "One simulation to fit them all - changing the background parameters of a cosmologicalN-body simulation". In: *Monthly Notices of the Royal Astronomical Society*.

Angulo, Raul E. and Andrew Pontzen (2016). "Cosmological N-body simulations with suppressed variance". In: *Monthly Notices of the Royal Astronomical Society: Letters* 462.1, pp. L1–L5. eprint: https://academic.oup.com/mnrasl/article-pdf/462/1/L1/8009434/slw098.pdf.

Angulo, Raul E. et al. (2020). *The BACCO Simulation Project: Exploiting the full power of large-scale structure for cosmology*. arXiv: 2004.06245 [astro-ph.CO].

Bernardeau, F. et al. (2002). "Large-scale structure of the Universe and cosmological perturbation theory". In: *Physics Reports* 367.1-3, 1–248.

Beutler, Florian, Emanuele Castorina, and Pierre Zhang (2019). "Interpreting measurements of the anisotropic galaxy power spectrum". In: *Journal of Cosmology and Astroparticle Physics* 2019.03, 040–040.

Beutler, Florian et al. (2014). "The clustering of galaxies in the SDSS-III Baryon Oscillation Spectroscopic Survey: testing gravity with redshift space distortions using the power spectrum multipoles". In: *Monthly Notices of the Royal Astronomical Society* 443.2, 1065–1089.

Bianchi, Davide et al. (2015). "Measuring line-of-sight-dependent Fourier-space clustering using FFTs". In: *Monthly Notices of the Royal Astronomical Society: Letters* 453.1, L11–L15.

Blake, Chris et al. (2011). "The WiggleZ Dark Energy Survey: testing the cosmological model with baryon acoustic oscillations at z= 0.6". In: *Monthly Notices of the Royal Astronomical Society* 415.3, 2892–2909.

Bottini, D. et al. (2005). "The Very Large Telescope Visible Multi-Object Spectrograph Mask Preparation Software". In: *Publications of the Astronomical Society of the Pacific* 117.835, pp. 996–1003.

Carrasco, John Joseph M., Mark P. Hertzberg, and Leonardo Senatore (2012). "The effective field theory of cosmological large scale structures". In: *Journal of High Energy Physics* 2012.9.

Colless, Matthew et al. (2001). "The 2dF Galaxy Redshift Survey: spectra and redshifts". In: *Monthly Notices of the Royal Astronomical Society* 328.4, pp. 1039–1063. eprint: https://academic.oup.com/mnras/article-pdf/328/4/1039/3780131/328-4-1039.pdf.

Davis, M. and P. J. E. Peebles (Apr. 1983). "A survey of galaxy redshifts. V. The two-point position and velocity correlations." In: *The Astrophysical Journal* 267, pp. 465–482.

de la Torre, S. et al. (2013). "The VIMOS Public Extragalactic Redshift Survey (VIPERS)". In: *Astronomy & Astrophysics* 557, A54.

de la Torre, Sylvain and Luigi Guzzo (2012). “Modelling non-linear redshift-space distortions in the galaxy clustering pattern: systematic errors on the growth rate parameter”. In: *Monthly Notices of the Royal Astronomical Society* 427.1, 327–342.

de Mattia, Arnaud and Vanina Ruhlmann-Kleider (2019). “Integral constraints in spectroscopic surveys”. In: *Journal of Cosmology and Astroparticle Physics* 2019.08, 036–036.

Desjacques, Vincent, Donghui Jeong, and Fabian Schmidt (2018). “Large-scale galaxy bias”. In: *Physics Reports* 733, 1–193.

Dodelson, Scott and Fabian Schmidt (2021). “11 - Probes of structure: tracers”. In: *Modern Cosmology (Second Edition)*. Ed. by Scott Dodelson and Fabian Schmidt. Second Edition. Academic Press, pp. 295–323.

Euclid Collaboration et al. (2020). *Euclid preparation: IX. EuclidEmulator2 – Power spectrum emulation with massive neutrinos and self-consistent dark energy perturbations*. arXiv: 2010.11288 [astro-ph.CO].

Feldman, Hume A., Nick Kaiser, and John A. Peacock (1994). “Power-spectrum analysis of three-dimensional redshift surveys”. In: *The Astrophysical Journal* 426, p. 23.

Garilli, B. et al. (2014). “The VIMOS Public Extragalactic Survey (VIPERS) - First Data Release of 57 spectroscopic measurements”. In: *Astronomy & Astrophysics* 562, A23.

Gong, Yungui (2008). “Growth factor parametrization and modified gravity”. In: *Physical Review D* 78.12.

Guzzo, L. et al. (2014). “The VIMOS Public Extragalactic Redshift Survey (VIPERS): An unprecedented view of galaxies and large-scale structure at $0.5 < z < 1.2$”. In: *Astron. Astrophys.* 566, A108. arXiv: 1303.2623 [astro-ph.CO].

Hadzhiyska, Boryana et al. (2021). *Hefty enhancement of cosmological constraints from the DES Y1 data using a Hybrid Effective Field Theory approach to galaxy bias*. arXiv: 2103.09820 [astro-ph.CO].

Hamilton, A. J. S. (2000). “Uncorrelated modes of the non-linear power spectrum”. In: *MNRAS* 312, pp. 257–284. eprint: astro-ph/9905191.

Heitmann, Katrin et al. (2013). “THE COYOTE UNIVERSE EXTENDED: PRECISION EMULATION OF THE MATTER POWER SPECTRUM”. In: 780.1, p. 111.

Hinshaw, G. et al. (2013). “NINE-YEAR WILKINSON MICROWAVE ANISOTROPY PROBE ( WMAP ) OBSERVATIONS: COSMOLOGICAL PARAMETER RESULTS”. In: *The Astrophysical Journal Supplement Series* 208.2, p. 19.

Howlett, Cullan, Marc Manera, and Will J. Percival (2015). *L-PICOLA: A parallel code for fast dark matter simulation*. arXiv: 1506.03737 [astro-ph.CO].

Jing, Y. P. (2005). “Correcting for the Alias Effect When Measuring the Power Spectrum Using a Fast Fourier Transform”. In: *The Astrophysical Journal* 620.2, 559–563.

Jones, D. Heath et al. (Dec. 2004). “The 6dF Galaxy Survey: samples, observational techniques and the first data release”. In: *Monthly Notices of the Royal Astronomical Society* 355.3, pp. 747–763. arXiv: astro-ph/0403501 [astro-ph].

Kaiser, Nick (1987). “Clustering in real space and in redshift space”. In: *Monthly Notices of the Royal Astronomical Society* 227.1, pp. 1–21. eprint: https://academic.oup.com/mnras/article-pdf/227/1/1/18522208/mnras227-0001.pdf.

Kennicutt Robert C., Jr. (Apr. 1992). “A Spectrophotometric Atlas of Galaxies”. In: *The Astrophysical Journal* 79, p. 255.

Klypin, Anatoly, Francisco Prada, and Joyce Byun (2020). “Suppressing cosmic variance with paired-and-fixed cosmological simulations: average properties and covariances of dark matter clustering statistics”. In: *Monthly Notices of the Royal Astronomical Society* 496.3, 3862–3869.

Kobayashi, Yosuke et al. (2020). “Accurate emulator for the redshift-space power spectrum of dark matter halos and its application to galaxy power spectrum”. In: *Physical Review D* 102.6.

Kokron, Nickolas et al. (2021). *The cosmology dependence of galaxy clustering and lensing from a hybrid $N$-body-perturbation theory model*. arXiv: 2101.11014 [astro-ph.CO].

Lawrence, Earl et al. (2017). “The Mira-Titan Universe. II. Matter Power Spectrum Emulation”. In: *The Astrophysical Journal* 847.1, p. 50.

Liske, J. et al. (Sept. 2015). “Galaxy And Mass Assembly (GAMA): end of survey report and data release 2”. In: *Monthly Notices of the Royal Astronomical Society* 452.2, pp. 2087–2126. arXiv: 1506.08222 [astro-ph.GA].

Matsubara, Takahiko (2015). “Recursive solutions of Lagrangian perturbation theory”. In: *Physical Review D* 92.2.

McDonald, Patrick and Uroš Seljak (2009). “How to evade the sample variance limit on measurements of redshift-space distortions”. In: *Journal of Cosmology and Astroparticle Physics* 2009.10, 007–007.

Modi, Chirag, Shi-Fan Chen, and Martin White (2020). “Simulations and symmetries”. In: *Monthly Notices of the Royal Astronomical Society* 492.4, 5754–5763.

Mohammad, F. G. et al. (2018). “The VIMOS Public Extragalactic Redshift Survey (VIPERS)”. In: *Astronomy and Astrophysics* 619, A17.

Montero-Dorta, Antonio D et al. (2020). “The Multi-Tracer Optimal Estimator applied to VIPERS”. In: *Monthly Notices of the Royal Astronomical Society* 493.4, 5257–5272.

Newman, Jeffrey A. et al. (Sept. 2013). “The DEEP2 Galaxy Redshift Survey: Design, Observations, Data Reduction, and Redshifts”. In: *The Astrophysical Journal Supplement* 208.1, 5, p. 5. arXiv: 1203.3192 [astro-ph.CO].

Nishimichi, Takahiro et al. (2020). “Blinded challenge for precision cosmology with large-scale structure: Results from effective field theory for the redshift-space galaxy power spectrum”. In: *Physical Review D* 102.12.

Padmanabhan, Nikhil et al. (Dec. 2012). “A 2 per cent distance to z = 0.35 by reconstructing baryon acoustic oscillations - I. Methods and application to the Sloan Digital Sky Survey”. In: *Monthly Notices of the Royal Astronomical Society* 427.3, pp. 2132–2145. arXiv: 1202.0090 [astro-ph.CO].

Peacock, J. A. and S. J. Dodds (1994). “Reconstructing the linear power spectrum of cosmological mass fluctuations”. In: *Monthly Notices of the Royal Astronomical Society* 267.4, 1020–1034.

Percival, W. J., L. Verde, and J. A. Peacock (2004). “Fourier analysis of luminosity-dependent galaxy clustering”. In: *Monthly Notices of the Royal Astronomical Society* 347.2, 645–653.

Perlmutter, S. et al. (1999). “Measurements of $\Omega$ and $\Lambda$ from 42 High-Redshift Supernovae”. In: *The Astrophysical Journal* 517.2, pp. 565–586.

Pezzotta, A. et al. (2017). “The VIMOS Public Extragalactic Redshift Survey (VIPERS)”. In: *Astronomy & Astrophysics* 604, A33.

Planck Collaboration (2018). “Planck 2018 results. VI. Cosmological parameters”. In: *Astronomy & Astrophysics*. arXiv: 1807.06209.

Reid, Beth A. et al. (2014). “A 2.5 per cent measurement of the growth rate from small-scale redshift space clustering of SDSS-III CMASS galaxies”. In: *Monthly Notices of the Royal Astronomical Society* 444.1, pp. 476–502. eprint: https://academic.oup.com/mnras/article-pdf/444/1/476/18502117/stu1391.pdf.

Riess, Adam G. (2019). “The expansion of the Universe is faster than expected”. In: *Nature Reviews Physics* 2.1, 10–12.

Riess, Adam G. et al. (1998). “Observational evidence from supernovae for an accelerating universe and a cosmological constant”. In: *Astron. J.* 116, pp. 1009–1038. arXiv: astro-ph/9805201.

Rota, S. et al. (2017). “The VIMOS Public Extragalactic Redshift Survey (VIPERS)”. In: *Astronomy & Astrophysics* 601, A144.

Rubin, Vera C. and W. Kent Ford Jr. (1970). “Rotation of the Andromeda Nebula from a Spectroscopic Survey of Emission Regions”. In: *Astrophys. J.* 159, pp. 379–403.

Schmittfull, Marcel et al. (2019). “Modeling biased tracers at the field level”. In: *Physical Review D* 100.4.

Scoccimarro, Román (2004). “Redshift-space distortions, pairwise velocities, and nonlinearities”. In: *Physical Review D* 70.8.

— (2015). “Fast estimators for redshift-space clustering”. In: *Physical Review D* 92.8.

Sefusatti, E. et al. (2016). “Accurate estimators of correlation functions in Fourier space”. In: *Monthly Notices of the Royal Astronomical Society* 460.4, 3624–3636.

Sheth, R. K. (1996). “The distribution of pairwise peculiar velocities in the non-linear regime”. In: *Monthly Notices of the Royal Astronomical Society* 279.4, 1310–1324.

Song, Yong-Seon and Will J Percival (2009). “Reconstructing the history of structure formation using redshift distortions”. In: *Journal of Cosmology and Astroparticle Physics* 2009.10, 004–004.

Taruya, Atsushi, Takahiro Nishimichi, and Shun Saito (2010). “Baryon acoustic oscillations in 2D: Modeling redshift-space power spectrum from perturbation theory”. In: *Physical Review D* 82.6.

Tegmark, Max et al. (1998). “Measuring the Galaxy Power Spectrum with Future Redshift Surveys”. In: *The Astrophysical Journal* 499.2, 555–576.

Torre, S. de la et al. (2017). “The VIMOS Public Extragalactic Redshift Survey (VIPERS)”. In: *Astronomy & Astrophysics* 608, A44.

Trimble, Virginia (1987). “Existence and Nature of Dark Matter in the Universe”. In: *Annual Review of Astronomy and Astrophysics* 25.1, pp. 425–472. eprint: https://doi.org/10.1146/annurev.aa.25.090187.002233.

Villaescusa-Navarro, Francisco et al. (2018). “Statistical Properties of Paired Fixed Fields”. In: *The Astrophysical Journal* 867.2, p. 137.

Wechsler, Risa H. and Jeremy L. Tinker (2018). “The Connection Between Galaxies and Their Dark Matter Halos”. In: *Annual Review of Astronomy and Astrophysics* 56.1, 435–487.

Wilson, M. J. et al. (2016). “Rapid modelling of the redshift-space power spectrum multipoles for a masked density field”. In: *Monthly Notices of the Royal Astronomical Society* 464.3, pp. 3121–3130. eprint: https://academic.oup.com/mnras/article-pdf/464/3/3121/18519335/stw2576.pdf.

Wilson, Michael J. (2016). *Geometric and growth rate tests of General Relativity with recovered linear cosmological perturbations*. arXiv: 1610.08362 [astro-ph.CO].

Yamamoto, Kazuhiro et al. (2006). “A Measurement of the Quadrupole Power Spectrum in the Clustering of the 2dF QSO Survey”. In: *Publications of the Astronomical Society of Japan* 58.1, 93–102.

York, Donald G. et al. (2000). “The Sloan Digital Sky Survey: Technical Summary”. In: *The Astronomical Journal* 120.3, 1579–1587.

Zennaro, Matteo et al. (2021). *The BACCO simulation project: biased tracers in real space*. arXiv: 2101.12187 [astro-ph.CO].

# Appendix A

# Additional Results of VIPERS Analysis

## A.1 $z_2$

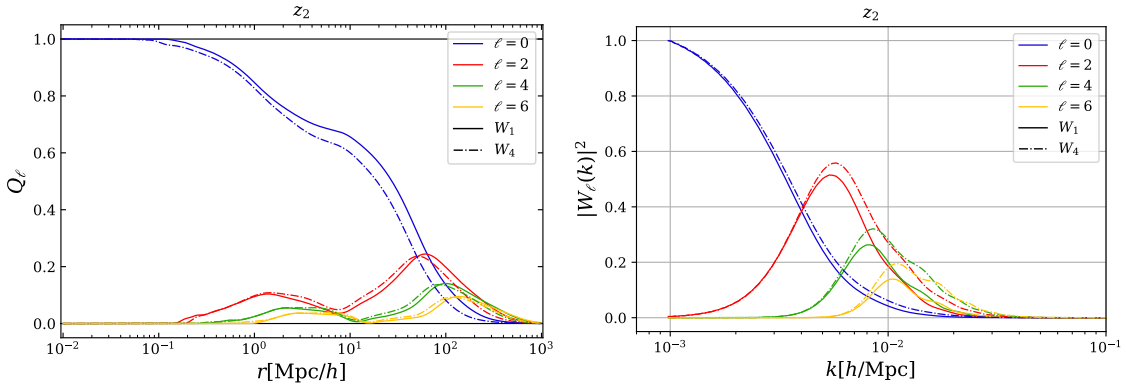


**Figure A.1:** *Left Panel:* Measurement of the $Q_\ell$ for the $z_2$ redshift slice, using a random catalogue which has the same mask and radial distribution as the data. *Right Panel:* Modulus squared of the Hankel transform of the $Q_\ell$. This quantity is important to correctly account for the integral constraint.

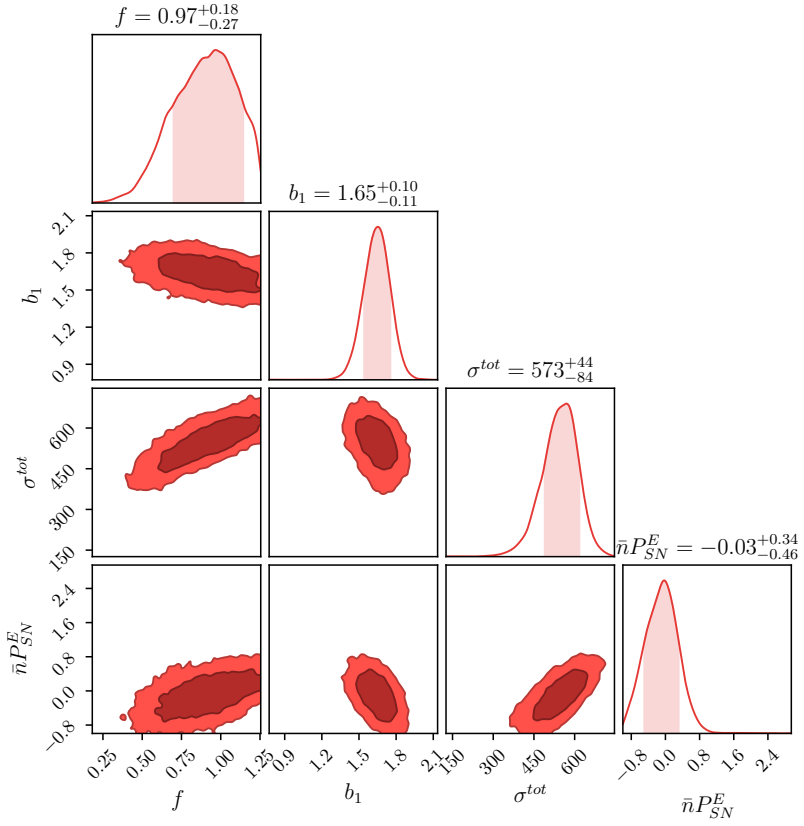


**Figure A.2:** Countours showing the posteriors on the parameters, obtained using real data from the $W_1$ observation field ov VIPERS, in the $z_2$ redshift slice, ranging from $z = 0.55$ to $0.7$. The constraint on $f$ can also be translated into a constraint on $f\sigma_8$, giving us $f\sigma_8 = 0.50^{+0.12}_{-0.10}$.

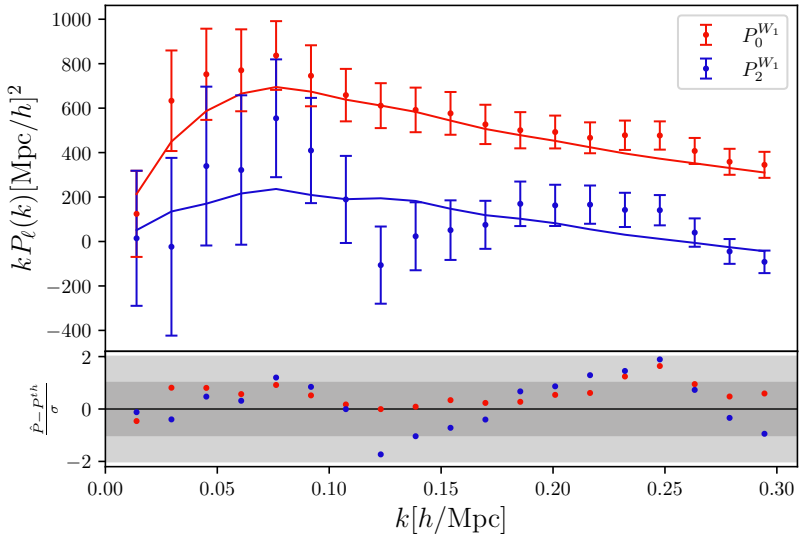


**Figure A.3:** Points with errorbars represent measurements of the monopole and quadrupole from real observations of the $z_2$ redshift slice in the $W_1$ observation field. Solid lines represent the model computed with the best fit parameters. Reduced chi-squared for this fit takes the value of $\chi^2_{\mathrm{red}} = 1.31$.

## A.2 $z_3$

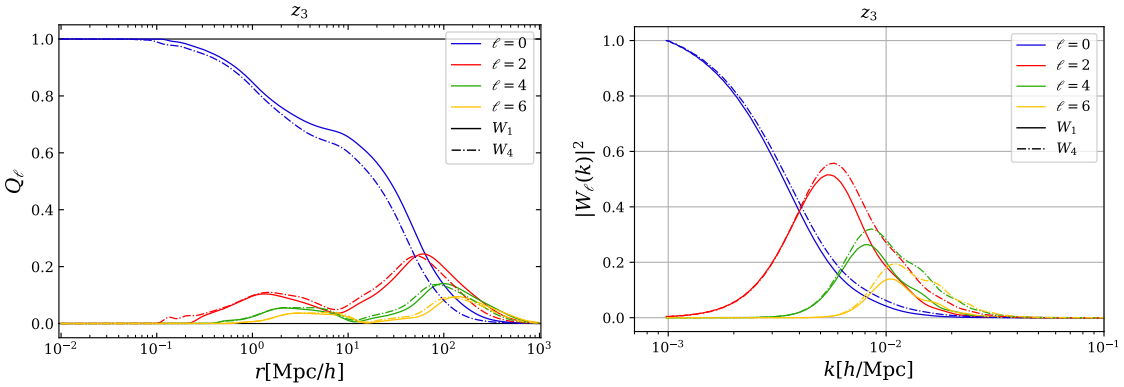


**Figure A.4:** *Left Panel:* Measurement of the $Q_\ell$ for the $z_3$ redshift slice, using a random catalogue which has the same mask and radial distribution as the data. *Right Panel:* Modulus squared of the Hankel transform of the $Q_\ell$. This quantity is important to correctly account for the integral constraint.

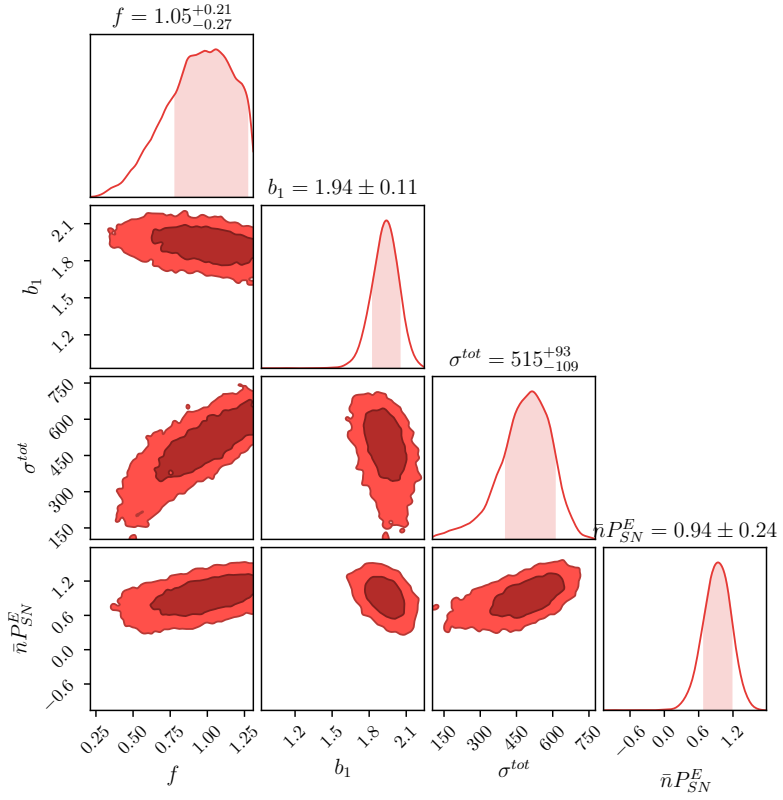


**Figure A.5:** Contours showing the posteriors on the parameters, obtained using real data from the $W_1$ observation field of VIPERS, in the $z_3$ redshift slice, ranging from $z = 0.7$ to 0.9. The constraint on $f$ can also be translated into a constraint on $f\sigma_8$, giving us $f\sigma_8 = 0.50^{+0.12}_{-0.10}$.

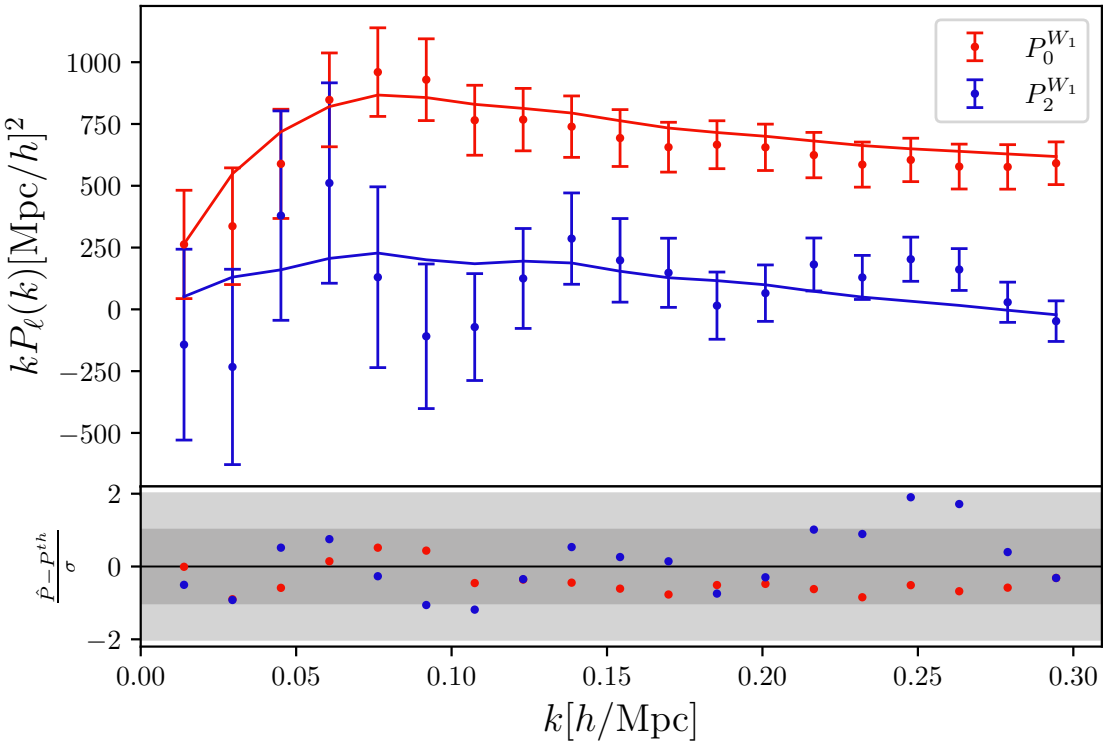


**Figure A.6:** Points with errorbars represent measurements of the monopole and quadrupole from real observations of the $z_3$ redshift slice in the $W_1$ observation field. Solid lines represent the model computed with the best fit parameters. Reduced chi-squared for this fit takes the value of $\chi^2_{\mathrm{red}} = 1.28$.

# Appendix B

# Lagrangian Perturbation Theory

As in fluid dynamics, there are two pictures through which one can look at the evolution of the dark-matter density; the Eulerian picture views density and velocity as cosmic fields, whose values are changing with time, and the Lagrangian picture takes a frame of reference which accompanies the motion of an arbitrary particle. Therefore, the central quantity in a Lagrangian picture is the displacement of a certain particle from its initial particle, defined by

$$\boldsymbol{\psi}(\mathbf{q}) = \mathbf{x}(\mathbf{q}) - \mathbf{q}. \tag{B.1}$$

The equation of motion for the position of a certain particle can be written as

$$\frac{d^2\mathbf{x}}{d\tau^2} + \mathcal{H}(\tau)\frac{d\mathbf{x}}{d\tau} = -\nabla\Phi, \tag{B.2}$$

in which $\mathbf{x}$ represents the particle position in Eulerian space, $\mathcal{H}$ is the conformal Hubble rate, $\tau$ is the conformal time, $\Phi$ denotes the gravitational potential, and $\nabla$ is the gradient with respect to Eulerian coordinates. Taking the divergence of this equation we can rewrite it as

$$\nabla \cdot \left[\frac{d^2\boldsymbol{\psi}}{d\tau^2} + \mathcal{H}(\tau)\frac{d\boldsymbol{\psi}}{d\tau}\right] = -\nabla^2\Phi, \tag{B.3}$$

in which we have discarded the derivative of $\mathbf{q}$ with respect to the conformal time. Substituting the Poisson equation we have

$$\nabla \cdot \left[ \frac{d^2\boldsymbol{\psi}}{d\tau^2} + \mathcal{H}(\tau) \frac{d\boldsymbol{\psi}}{d\tau} \right] = -\frac{3}{2} \Omega_m(\tau) \mathcal{H}^2(\tau) \delta(\mathbf{x}, \tau). \tag{B.4}$$

Since the evolution of this density field is only through gravity, one must have conservation of mass, at least before shell-crossing takes place; suppose we have a certain volume in Lagrangian space, $d^3\mathbf{q}$, which will be deformed due to the gravitational evolution into a volume $d^3\mathbf{x}$ in Eulerian space; the mass in these two volumes should be exactly the same, which can be expressed through the equation

$$\bar{\rho} \left[ 1 + \delta(\mathbf{x}, \tau) \right] d^3\mathbf{x} = \bar{\rho} d^3\mathbf{q}, \tag{B.5}$$

implying that the Jacobian of this coordinate transformation is given by

$$J(\mathbf{q}, \tau) = \left| \frac{d^3\mathbf{x}}{d^3\mathbf{q}} \right| = \det(\delta_{ij} + \psi_{i,j}) = \frac{1}{1 + \delta(\mathbf{x}, \tau)}. \tag{B.6}$$

Substituting this into our equation of motion, we obtain

$$J(\mathbf{q}, \tau) \nabla \cdot \left[ \frac{d^2\boldsymbol{\psi}}{d\tau^2} + \mathcal{H}(\tau) \frac{d\boldsymbol{\psi}}{d\tau} \right] = \frac{3}{2} \Omega_m(\tau) \mathcal{H}^2(\tau) \left( J - 1 \right). \tag{B.7}$$

We can now use the chain rule to transform the divergent operator from Eulerian to Lagrangian space

$$\frac{\partial}{\partial x_i} = \frac{\partial q_j}{\partial x_i} \frac{\partial}{\partial q_j} = \left[ \delta_{ij} + \psi_{i,j} \right]^{-1} \frac{\partial}{\partial q_j}, \tag{B.8}$$

allowing us to rewrite the equation of motion as

$$J(\mathbf{q}, \tau) \left[ \delta_{ij} + \psi_{i,j} \right]^{-1} \left[ \frac{d^2\psi_{i,j}}{d\tau^2} + \mathcal{H}(\tau) \frac{d\psi_{i,j}}{d\tau} \right] = \frac{3}{2} \Omega_m(\tau) \mathcal{H}^2(\tau) (J - 1). \tag{B.9}$$

This is the main equation for the Lagrangian perturbation theory formalism, which we will solve perturbatively, expanding the displacement as

$$\boldsymbol{\psi}(\mathbf{q}, \tau) = \boldsymbol{\psi}^{(1)}(\mathbf{q}, \tau) + \boldsymbol{\psi}^{(2)}(\mathbf{q}, \tau) + \cdots \tag{B.10}$$

## B.1 Linear Solution

To obtain the linear solution, we must first linearize the equation of motion; as a first step, we approximate the Jacobian of the transformation as

$$J(\mathbf{q},\tau) = \det(\delta_{ij} + \psi_{i,j}) = 1 + \psi^{(1)}_{i,i}, \tag{B.11}$$

and the inverse of the Jacobian matrix as

$$[\delta_{ij} + \psi_{i,j}]^{-1} = \delta_{ij} - \psi^{(1)}_{i,j}. \tag{B.12}$$

Substituting these expressions into the equation of motion, and keeping only linear order terms, we obtain

$$\frac{d^2(\nabla_{\mathbf{q}} \cdot \boldsymbol{\psi}^{(1)})}{d\tau^2} + \mathcal{H}(\tau)\frac{d(\nabla_{\mathbf{q}} \cdot \boldsymbol{\psi}^{(1)})}{d\tau} = \frac{3}{2}\Omega_m(\tau)\mathcal{H}^2(\tau)\nabla_{\mathbf{q}} \cdot \boldsymbol{\psi}^{(1)}. \tag{B.13}$$

Moreover, we can also make the approximation that

$$J(\mathbf{q},\tau) \approx 1 + \psi^{(1)}_{i,i} \approx 1 - \delta^{(1)}(\mathbf{q},\tau), \tag{B.14}$$

and thus, the linear solution is given by

$$\nabla_{\mathbf{q}}\boldsymbol{\psi}^{(1)} = -\delta^{(1)}(\mathbf{q},\tau), \tag{B.15}$$

and the time evolution is controlled by the equation of motion, factoring out the time-dependent part

$$\frac{d^2 D_1(\tau)}{d\tau^2} + \mathcal{H}(\tau)\frac{dD_1(\tau)}{d\tau} = \frac{3}{2}\Omega_m(\tau)\mathcal{H}^2(\tau)D_1(\tau). \tag{B.16}$$

In Fourier space, this can also be written as

$$\boldsymbol{\psi}^{(1)}(\mathbf{k},\tau) = i\frac{\mathbf{k}}{k^2}\delta^{(1)}(\mathbf{k},\tau). \tag{B.17}$$

## B.2 Recurrence Relations

It is possible to obtain recurrence relations for LPT, a work which has been carried out by Matsubara, 2015. We simply state the most useful expressions below, as deriving them is beyond the scope of this work. The n-th order displacement is given by

$$\psi^{(n)}(\mathbf{k},\tau) = \frac{1}{n!}\int d^3\mathbf{k}_1 \cdots d^3\mathbf{k}_n \mathbf{L}_n(\mathbf{k}_1,\cdots,\mathbf{k}_n,t)\delta^{(1)}(\mathbf{k}_1)\cdots\delta^{(1)}(\mathbf{k}_n)\delta^D(\mathbf{k}_1\cdots+\mathbf{k}_n-\mathbf{k}), \tag{B.18}$$

and the second order kernel is given by

$$\mathbf{L}_2(\mathbf{k}_1,\mathbf{k}_2) = \frac{3}{7}\frac{\mathbf{k}_1+\mathbf{k}_2}{|\mathbf{k}_1+\mathbf{k}_2|^2}\left(1-\left(\frac{\mathbf{k}_1\cdot\mathbf{k}_2}{k_1k_2}\right)^2\right) \tag{B.19}$$

# Appendix C

# Advected Basis Fields and Spectra

In this appendix we describe how one can advect the basis fields which go into the Lagrangian bias expansion of equation (6.1) and give the expressions for the 5 basis fields and 15 auto and cross basis spectra in Eulerian space. Notice that all of our computations will involve the perturbative expansion of the displacement field up to first order, and a Taylor expansion of the exponential up to second order.

## C.1 Advected Basis Fields

### C.1.1 $\delta_1$

The $1$ field is nothing more than a uniform field in Lagrangian space, and therefore, $\delta_1(\mathbf{k})$ will be the prediction for the Eulerian matter density field. If one would expand the displacement only up to first order, the result from this advection procedure would be the Z'eldovich field, i.e.: the prediction from first order Lagrangian perturbation theory, best known as the Z'eldovich approximation. Plugging in $F(\mathbf{q}) = 1$ into equation (6.15) one obtains

$$
\begin{aligned}
\delta_1(\mathbf{k}) =& \int d^3\mathbf{q}\left[1 - i\mathbf{k}\cdot\left(\boldsymbol{\psi}^{(1)}(\mathbf{q}) + \boldsymbol{\psi}^{(2)}(\mathbf{q})\right) - \frac{(\mathbf{k}\cdot\boldsymbol{\psi}^{(1)})^2}{2}\right] e^{-i\mathbf{k}\cdot\mathbf{q}} \\
=& \delta^D(\mathbf{k}) - ik_i \int d^3\mathbf{q} \int_{\mathbf{k}_1} e^{-i(\mathbf{k}-\mathbf{k}_1)\cdot\mathbf{q}} \left(\psi_i^{(1)}(\mathbf{k}_1) + \psi_i^{(2)}(\mathbf{k}_1)\right) \\
& - \frac{k_i k_j}{2} \int d^3\mathbf{q} \int_{\mathbf{k}_1}\int_{\mathbf{k}_2} e^{-i(\mathbf{k}-\mathbf{k}_{12})\cdot\mathbf{q}} \psi_i^{(1)}(\mathbf{k}_1)\psi_j^{(1)}(\mathbf{k}_2) \\
=& \delta^D(\mathbf{k}) - ik_i \int_{\mathbf{k}_1} \delta^D(\mathbf{k}-\mathbf{k}_1) \left(\psi_i^{(1)}(\mathbf{k}_1) + \psi_i^{(2)}(\mathbf{k}_1)\right) \\
& - \frac{k_i k_j}{2} \int_{\mathbf{k}_1}\int_{\mathbf{k}_2} \delta^D(\mathbf{k}-\mathbf{k}_{12}) \psi_i^{(1)}(\mathbf{k}_1)\psi_j^{(1)}(\mathbf{k}_2)
\end{aligned}
\tag{C.1}
$$

and using the results of appendix B we can substitute for the displacements, obtaining

$$
\begin{aligned}
\delta_1(\mathbf{k}) =& -i\mathbf{k}\cdot\left(i\frac{\mathbf{k}}{k^2}\delta^L(\mathbf{k}) + \frac{i}{2}\int_{\mathbf{k}_1} \mathbf{L}_2(\mathbf{k}_1, \mathbf{k}-\mathbf{k}_1, \mathbf{k})\delta^L(\mathbf{k}_1)\delta^L(\mathbf{k}-\mathbf{k}_1)\right) \\
& + \frac{1}{2}\int_{\mathbf{k}_1}\int_{\mathbf{k}_2} \frac{\mathbf{k}\cdot\mathbf{k}_1}{kk_1}\frac{\mathbf{k}\cdot\mathbf{k}_2}{kk_2}\delta^D(\mathbf{k}-\mathbf{k}_{12})\delta^L(\mathbf{k}_1)\delta^L(\mathbf{k}-\mathbf{k}_1) \\
=& \delta^L(\mathbf{k}) + \frac{1}{2}\int_{\mathbf{k}_1} \mathbf{k}\cdot\mathbf{L}_2(\mathbf{k}_1, \mathbf{k}-\mathbf{k}_1, \mathbf{k})\delta^L(\mathbf{k}_1)\delta^L(\mathbf{k}-\mathbf{k}_1) \\
& + \frac{1}{2}\int_{\mathbf{k}_1} F_{ZA}(\mathbf{k}_1, \mathbf{k}-\mathbf{k}_1)\delta^L(\mathbf{k}_1)\delta^L(\mathbf{k}-\mathbf{k}_1),
\end{aligned}
\tag{C.2}
$$

in which $F_{ZA}$ is given by

$$
F_{ZA}(\mathbf{k}_1, \mathbf{k}_2) = 1 + \frac{\mathbf{k}_1\cdot\mathbf{k}_2}{k_i k_2}\left(\frac{k_1}{k_2} + \frac{k_2}{k_1}\right) + \frac{(\mathbf{k}_1\cdot\mathbf{k}_2)^2}{k_1^2 k_2^2},
\tag{C.3}
$$

and we have discarded the term which consisted solely of a Dirac delta, since it will contribute only to unphysical values of $\mathbf{k}$. Restating this result in a more compact notation, we have

$$
\boxed{\delta_1(\mathbf{k}) = \delta^L_{\mathbf{k}} + \frac{1}{2}\int_{\mathbf{q}_1} \mathbf{q}_1\cdot\mathcal{K}_1(\mathbf{q}_1, \mathbf{k}-\mathbf{q}_1, \mathbf{k})\delta^L_{\mathbf{q}_1}\delta^L_{\mathbf{k}-\mathbf{q}_1} + \mathcal{O}(\delta^3).}
\tag{C.4}
$$

We will not derive the other basis spectra in detail, since the process is extremely similar, and very cumbersome, but simply state the results.

### C.1.2 $\delta_\delta$

Substituting $F(\mathbf{q}) = \delta^L(\mathbf{q})$ into equation (6.15) we get

$$\delta_\delta(\mathbf{k}) = \int d^3\mathbf{q} e^{-i\mathbf{k}\cdot\mathbf{q}} \delta^L(\mathbf{q}) \left[1 - i\mathbf{k}\cdot(\boldsymbol{\psi}^{(1)} + \boldsymbol{\psi}^{(2)}) - \frac{(\mathbf{k}\cdot\boldsymbol{\psi}^{(1)})^2}{2}\right]. \tag{C.5}$$

We will split this expression into four different terms, to ease its computation, and make things clearer; these will be

$$\begin{aligned} A(\mathbf{k}) &= \int d^3\mathbf{q} e^{-i\mathbf{k}\cdot\mathbf{q}} \delta^L(\mathbf{q}) \\ B(\mathbf{k}) &= -i \int d^3\mathbf{q} e^{-i\mathbf{k}\cdot\mathbf{q}} \delta^L(\mathbf{q}) \mathbf{k}\cdot\boldsymbol{\psi}^{(1)}(\mathbf{q}) \\ C(\mathbf{k}) &= -i \int d^3\mathbf{q} e^{-i\mathbf{k}\cdot\mathbf{q}} \delta^L(\mathbf{q}) \mathbf{k}\cdot\boldsymbol{\psi}^{(2)}(\mathbf{q}) \\ D(\mathbf{k}) &= -\frac{1}{2} \int d^3\mathbf{q} e^{-i\mathbf{k}\cdot\mathbf{q}} \delta^L(\mathbf{q}) \left(\mathbf{k}\cdot\boldsymbol{\psi}^{(1)}\right)^2. \end{aligned} \tag{C.6}$$

The first is very simple, and is just a regular Fourier transform, leading to

$$A(\mathbf{k}) = \delta^L(\mathbf{k}). \tag{C.7}$$

The second is a bit more involved, and we do the same procedure as before, of writing the fields which are in Lagrangian space as inverse Fourier transforms

$$\begin{aligned} B(\mathbf{k}) &= -i \int d^3\mathbf{q} e^{-i\mathbf{k}\cdot\mathbf{q}} \int_{\mathbf{k}_1} e^{i\mathbf{k}_1\cdot\mathbf{q}} \delta^L(\mathbf{k}_1) \mathbf{k}\cdot\int_{\mathbf{k}_2} \boldsymbol{\psi}^{(1)}(\mathbf{k}_2) e^{i\mathbf{k}_2\cdot\mathbf{q}} \\ &= \int_{\mathbf{k}_1,\mathbf{k}_2} \int d^3\mathbf{q} e^{-i(\mathbf{k}-\mathbf{k}_{12})\cdot\mathbf{q}} \delta^L(\mathbf{k}_1)\delta^L(\mathbf{k}_2) \frac{\mathbf{k}\cdot\mathbf{k}_2}{k_2^2} \\ &= \int_{\mathbf{k}_1} \delta^L(\mathbf{k}_1)\delta^L(\mathbf{k}-\mathbf{k}_1) \frac{\mathbf{k}\cdot(\mathbf{k}-\mathbf{k}_1)}{|\mathbf{k}-\mathbf{k}_1|^2}. \end{aligned} \tag{C.8}$$

The next term can be computed by substituting the expression for $\boldsymbol{\psi}^{(2)}$

$$\begin{aligned} C(\mathbf{k}) &= -i \int_{\mathbf{k}_1,\mathbf{k}_2} \int d^3\mathbf{q} e^{i(\mathbf{k}-\mathbf{k}_{12})\cdot\mathbf{q}} \delta^L(\mathbf{k}_1)\mathbf{k}\cdot\boldsymbol{\psi}^{(2)}(\mathbf{k}_2) \\ &= \frac{1}{2}\int_{\mathbf{k}_1,\mathbf{k}_2} \int d^3\mathbf{q} e^{i(\mathbf{k}-\mathbf{k}_{12})\cdot\mathbf{q}} \delta^L(\mathbf{k}_1)\mathbf{k}\cdot\int_{\mathbf{p}} \mathbf{L}_2(\mathbf{p},\mathbf{k}_2-\mathbf{p},\mathbf{k}_2)\delta^L(\mathbf{p})\delta^L(\mathbf{k}_2-\mathbf{p}) \\ &= \frac{1}{2}\int_{\mathbf{k}_1}\int_{\mathbf{p}} \delta^L(\mathbf{k}_1)\delta^L(\mathbf{p})\delta^L(\mathbf{k}-\mathbf{k}_1-\mathbf{p})\mathbf{k}\cdot\mathbf{L}_2(\mathbf{p},\mathbf{k}-\mathbf{k}_1-\mathbf{p},\mathbf{k}-\mathbf{k}_1), \end{aligned} \tag{C.9}$$

and renaming the integrated wavevector $\mathbf{p} \to \mathbf{k}_2$, we can rewrite this as

$$C(\mathbf{k}) = \int_{\mathbf{k}_1,\mathbf{k}_2} \delta^L(\mathbf{k}_1)\delta^L(\mathbf{k}_2)\delta^L(\mathbf{k}-\mathbf{k}_{12})\mathbf{k}\cdot\mathbf{L}_2(\mathbf{k},\mathbf{k}-\mathbf{k}_{12},\mathbf{k}-\mathbf{k}_1). \tag{C.10}$$

Finally, for the last term

$$\begin{aligned} D(\mathbf{k}) &= -\frac{k_i k_j}{2}\int d^3\mathbf{q} \int_{\mathbf{k}_1,\mathbf{k}_2,\mathbf{k}_3} e^{-i(\mathbf{k}-\mathbf{k}_{123})\cdot\mathbf{q}} \delta^L(\mathbf{k}_1)\psi_i^{(1)}(\mathbf{k}_2)\psi_j^{(1)}(\mathbf{k}_3) \\ &= \frac{1}{2}\int_{\mathbf{k}_1,\mathbf{k}_2,\mathbf{k}_3} \delta^D(\mathbf{k}-\mathbf{k}_{123})\delta^L(\mathbf{k}_1)\delta^L(\mathbf{k}_2)\delta^L(\mathbf{k}_3)\frac{\mathbf{k}\cdot\mathbf{k}_2}{k_2^2}\frac{\mathbf{k}\cdot\mathbf{k}_3}{k_3^2} \\ &= \frac{1}{2}\int_{\mathbf{k}_1,\mathbf{k}_2} \delta^L(\mathbf{k}_1)\delta^L(\mathbf{k}_2)\delta^L(\mathbf{k}-\mathbf{k}_{12})F_{ZA}(\mathbf{k}_2,\mathbf{k}-\mathbf{k}_{12}). \end{aligned} \tag{C.11}$$

All of these terms can be combined into a more compact form

$$\boxed{\delta_\delta(\mathbf{k}) = \delta^L_{\mathbf{k}} + \int_{\mathbf{q}_1} \delta^L_{\mathbf{q}_1}\delta^L_{\mathbf{k}-\mathbf{q}_1}\frac{\mathbf{k}\cdot(\mathbf{k}-\mathbf{q}_1)}{|\mathbf{k}-\mathbf{q}_1|^2} + \frac{1}{2}\int_{\mathbf{q}_1,\mathbf{q}_2} \delta^L_{\mathbf{q}_1}\delta^L_{\mathbf{q}_2}\delta^L_{\mathbf{k}-\mathbf{q}_{12}}\mathcal{K}_1(\mathbf{q}_2,\mathbf{k}-\mathbf{q}_{12},\mathbf{k}-\mathbf{q}_1)} \tag{C.12}$$

### C.1.3 $\delta_{\delta^2}$

$$\delta_{\delta^2}(\mathbf{k}) = \int d^3\mathbf{q} e^{-i\mathbf{k}\cdot\mathbf{q}} \left[\delta^L(\mathbf{q})\right]^2 \left[1 - i\mathbf{k}\cdot(\boldsymbol{\psi}^{(1)}+\boldsymbol{\psi}^{(2)}) - \frac{(\mathbf{k}\cdot\boldsymbol{\psi}^{(1)})^2}{2}\right] \tag{C.13}$$

Once again we will split this expression into four terms, which we will analyze sep-

arately; these are:

$$
\begin{aligned}
A(\mathbf{k}) &= \int d^3\mathbf{q} e^{-i\mathbf{k}\cdot\mathbf{q}} \left[\delta^L\right]^2 \\
B(\mathbf{k}) &= -i\mathbf{k}\cdot \int d^3\mathbf{q} e^{-i\mathbf{k}\cdot\mathbf{q}} \left[\delta^L\right]^2 \boldsymbol{\psi}^{(1)} \\
C(\mathbf{k}) &= \int d^3\mathbf{q} e^{-i\mathbf{k}\cdot\mathbf{q}} \left[\delta^L\right]^2 \boldsymbol{\psi}^{(2)} \\
D(\mathbf{k}) &= -\frac{k_i k_j}{2} \int d^3\mathbf{q} e^{-i\mathbf{k}\cdot\mathbf{q}} \left[\delta^L\right]^2 \psi_i^{(1)} \psi_j^{(1)}
\end{aligned}
\tag{C.14}
$$

We begin by rewriting the $A(\mathbf{k})$ and $B(\mathbf{k})$ terms; the second last terms are of third order in $\delta^L$, which is beyond the perturbation order up to which we want to compute our results,

$$
\begin{aligned}
A(\mathbf{k}) &= \int_{\mathbf{k}_1,\mathbf{k}_2} \int d^3\mathbf{q} e^{-i(\mathbf{k}-\mathbf{k}_{12})\cdot\mathbf{q}} \delta^L(\mathbf{k}_1)\delta^L(\mathbf{k}_2) \\
&= \int_{\mathbf{k}_1} \delta^L(\mathbf{k}_1)\delta^L(\mathbf{k}-\mathbf{k}_1)
\end{aligned}
\tag{C.15}
$$

$$
\begin{aligned}
B(\mathbf{k}) &= -i\mathbf{k}\cdot \int_{\mathbf{k}_1,\mathbf{k}_2,\mathbf{k}_3} \int d^3\mathbf{q} e^{-i(\mathbf{k}-\mathbf{k}_{123})\cdot\mathbf{q}} \delta^L(\mathbf{k}_1)\delta^L(\mathbf{k}_2)\boldsymbol{\psi}^{(1)}(\mathbf{k}_3) \\
&= \int_{\mathbf{k}_1,\mathbf{k}_2} \delta^L(\mathbf{k}_1)\delta^L(\mathbf{k}_2)\delta^L(\mathbf{k}-\mathbf{k}_{12}) \frac{\mathbf{k}\cdot(\mathbf{k}-\mathbf{k}_{12})}{k|\mathbf{k}-\mathbf{k}_{12}|}.
\end{aligned}
\tag{C.16}
$$

Rewriting these results in a more compact notation, we obtain

$$
\boxed{\delta_{\delta^2}(\mathbf{k}) = \int_{\mathbf{k}_1} \delta^L_{\mathbf{k}_1}\delta^L_{\mathbf{k}-\mathbf{k}_1} + \int_{\mathbf{k}_1,\mathbf{k}_2} \delta^L_{\mathbf{k}_1}\delta^L_{\mathbf{k}_2}\delta^L_{\mathbf{k}-\mathbf{k}_{12}} \frac{\mathbf{k}\cdot(\mathbf{k}-\mathbf{k}_{12})}{k|\mathbf{k}-\mathbf{k}_{12}|}}
\tag{C.17}
$$

### C.1.4 $\delta_{s^2}$

$$
\delta_{s^2}(\mathbf{k}) = \int d^3\mathbf{q} e^{-i\mathbf{k}\cdot\mathbf{q}} s^2(\mathbf{q}) \left[1 - i\mathbf{k}\cdot(\boldsymbol{\psi}^{(1)} + \boldsymbol{\psi}^{(2)}) - \frac{(\mathbf{k}\cdot\boldsymbol{\psi}^{(1)})^2}{2}\right]
\tag{C.18}
$$

$$\delta_{s^2}(\mathbf{k}) = \int_{\mathbf{k}_1} \delta^L_{\mathbf{k}_1}\delta^L_{\mathbf{k}-\mathbf{k}_1} S_2(\mathbf{k}_1, \mathbf{k}-\mathbf{k}_1) + \int_{\mathbf{k}_1,\mathbf{k}_2} \frac{\mathbf{k}\cdot(\mathbf{k}-\mathbf{k}_{12})}{|\mathbf{k}-\mathbf{k}_{12}|^2} S_2(\mathbf{k}_1,\mathbf{k}_2)\delta^L_{\mathbf{k}_1}\delta^L_{\mathbf{k}_2}\delta^L_{\mathbf{k}-\mathbf{k}_{12}} + \mathcal{O}(\delta^4) \tag{C.19}$$

### C.1.5 $\delta_{\nabla^2\delta}$

$$\delta_{\nabla^2\delta}(\mathbf{k}) = \int d^3\mathbf{q} e^{-i\mathbf{k}\cdot\mathbf{q}} \nabla^2_{\mathbf{q}} \delta^L(\mathbf{q}) \left[1 - i\mathbf{k}\cdot(\boldsymbol{\psi}^{(1)} + \boldsymbol{\psi}^{(2)}) - \frac{(\mathbf{k}\cdot\boldsymbol{\psi}^{(1)})^2}{2}\right] \tag{C.20}$$

As for the other cases, we begin by dividing this into 4 distinct terms

$$\begin{aligned}
A(\mathbf{k}) &= \int_{\mathbf{k}_1} \int d^3\mathbf{q} e^{-i(\mathbf{k}-\mathbf{k}_1)\cdot\mathbf{q}} k_1^2 \delta^L(\mathbf{k}_1) \\
B(\mathbf{k}) &= -i\mathbf{k}\cdot \int_{\mathbf{k}_1,\mathbf{k}_2} \int d^3\mathbf{q} e^{-i(\mathbf{k}-\mathbf{k}_{12})\cdot\mathbf{q}} k_1^2 \delta^L(\mathbf{k}_1)\boldsymbol{\psi}^{(1)}(\mathbf{k}_2) \\
C(\mathbf{k}) &= -i\mathbf{k}\cdot \int_{\mathbf{k}_1,\mathbf{k}_2} \int d^3\mathbf{q} e^{-i(\mathbf{k}-\mathbf{k}_{12})\cdot\mathbf{q}} k_1^2 \delta^L(\mathbf{k}_1)\boldsymbol{\psi}^{(2)}(\mathbf{k}_2) \\
D(\mathbf{k}) &= -\frac{k_i k_j}{2} \int_{\mathbf{k}_1,\mathbf{k}_2,\mathbf{k}_3} \int d^3\mathbf{q} e^{-i(\mathbf{k}-\mathbf{k}_{123})\cdot\mathbf{q}} k_1^2 \delta^L(\mathbf{k}_1)\psi_i(\mathbf{k}_2)\psi_j(\mathbf{k}_3).
\end{aligned} \tag{C.21}$$

$A(\mathbf{k})$ can be rewritten as

$$A(\mathbf{k}) = k^2\delta^L(\mathbf{k}), \tag{C.22}$$

and working out the other terms as well,

$$\begin{aligned}
B(\mathbf{k}) &= \int_{\mathbf{k}_1,\mathbf{k}_2} k_1^2\delta^L(\mathbf{k}_1)\delta^L(\mathbf{k}_2)\frac{\mathbf{k}\cdot\mathbf{k}_2}{k_2^2}\delta^D(\mathbf{k}-\mathbf{k}_{12}) \\
&= \int_{\mathbf{k}_1} k_1^2\delta^L(\mathbf{k}_1)\delta^L(\mathbf{k}-\mathbf{k}_1)\frac{\mathbf{k}\cdot(\mathbf{k}-\mathbf{k}_1)}{|\mathbf{k}-\mathbf{k}_1|^2}.
\end{aligned} \tag{C.23}$$

One can already see from these computations that this is exactly equal to the case od $\delta_\delta$, but with one of the $\delta^L$ being multiplied by $k^2$. This allows us to write the following

expression for $\delta_{\nabla^2\delta}$

$$\boxed{\delta_{\nabla^2\delta}(\mathbf{k}) = k^2\delta^L_{\mathbf{k}} + \int_{\mathbf{q}_1} q_1^2\delta^L_{\mathbf{q}_1}\delta^L_{\mathbf{k}-\mathbf{q}_1}\frac{\mathbf{k}\cdot(\mathbf{k}-\mathbf{q}_1)}{|\mathbf{k}-\mathbf{q}_1|^2} + \frac{1}{2}\int_{\mathbf{q}_1,\mathbf{q}_2} q_1^2\delta^L_{\mathbf{q}_1}\delta^L_{\mathbf{q}_2}\delta^L_{\mathbf{k}-\mathbf{q}_{12}}\mathcal{K}_1(\mathbf{q}_2,\mathbf{k}-\mathbf{q}_{12},\mathbf{k}-\mathbf{q}_1)} \tag{C.24}$$

# Appendix D

# Detailed Variance Calculations

In this appendix we will present the full calculations through which we obtain theoretical predictions for the variances of the basis spectra in fixed and paired simulations. These were omitted from the text because the expressions are quite large, and are unnecessary for an intuitive explanation of the variance reduction in these spectra. A more interested reader can, however, find here a detailed account of how these expressions can be more rigorously derived, including discussions on the approximations eventually utilized.

In the following sections, whenever an integral of the kind $\int \frac{d^3\mathbf{k}}{(2\pi)^3}$ appears, we will simplify the notation, substituting it by

$$\int \frac{d^3\mathbf{k}}{(2\pi)^3} \longrightarrow \int_{\mathbf{k}}. \tag{D.1}$$

## D.1 $P_{11}$

The $\delta_1(\mathbf{k})$ field in Eulerian space is given by

$$\delta_1(\mathbf{k}) = \delta^L_{\mathbf{k}} + \frac{1}{2}\int_{\mathbf{q}_1} \mathbf{q}_1 \cdot \mathbf{L}_2(\mathbf{q}_1, \mathbf{k}-\mathbf{q}_1, \mathbf{k}) \delta^L_{\mathbf{q}_1} \delta^L_{\mathbf{k}-\mathbf{q}_1} + \frac{1}{2}\int_{\mathbf{q}_1} F_{ZA}(\mathbf{q}_1, \mathbf{k}-\mathbf{q}_1) \delta^L_{\mathbf{q}_1} \delta^L_{\mathbf{k}-\mathbf{q}_1} + \mathcal{O}(\delta^3), \tag{D.2}$$

in which $\mathbf{L}_2$ and $F_{ZA}$ are defined by

$$\begin{aligned}\mathbf{L}_2(\mathbf{p}_1,\mathbf{p}_2,\mathbf{k}) =& \frac{3\mathbf{k}}{7k^2}\left[1-\left(\frac{\mathbf{p}_1\cdot\mathbf{p}_2}{p_1p_2}\right)\right]\\ F_{ZA}(\mathbf{p}_1,\mathbf{p}_2) =& 1+\frac{\mathbf{p}_1\cdot\mathbf{p}_2}{p_1p_2}\left(\frac{p_1}{p_2}+\frac{p_2}{p_1}\right)+\frac{(\mathbf{p}_1\cdot\mathbf{p}_2)^2}{p_1^2p_2^2},\end{aligned} \tag{D.3}$$

and the power spectrum of this field will be given by

$$\begin{aligned}P_{11}(\mathbf{k}) =& V_f\delta^L_{\mathbf{k}}\delta^L_{-\mathbf{k}} + V_f\int_{\mathbf{q}_1}\mathrm{Re}\left[\delta^L_{\mathbf{k}}\delta^L_{-\mathbf{q}_1}\delta^L_{-\mathbf{k}+\mathbf{q}_1}\right]F_{ZA}(\mathbf{q}_1,\mathbf{k}-\mathbf{q}_1)\\ &+V_f\int_{\mathbf{q}_1}\mathbf{q}_1\cdot\mathbf{L}_2(\mathbf{q_1},\mathbf{k}-\mathbf{q}_1,\mathbf{k})\,\mathrm{Re}\left[\delta^L_{\mathbf{k}}\delta^L_{-\mathbf{q}_1}\delta^L_{\mathbf{q}_1-\mathbf{k}}\right]\\ &+\frac{V_f}{4}\int_{\mathbf{q}_1}\int_{\mathbf{q}_2}\mathrm{Re}\left[\delta^L_{\mathbf{q}_1}\delta^L_{\mathbf{k}-\mathbf{q}_1}\delta^L_{-\mathbf{q}_2}\delta^L_{\mathbf{q}_2-\mathbf{k}}\right]F_{ZA}(\mathbf{q}_1,\mathbf{k}-\mathbf{q}_1)F_{ZA}(\mathbf{q}_2,\mathbf{k}-\mathbf{q}_2)\\ &+\frac{V_f}{4}\int_{\mathbf{q}_1}\int_{\mathbf{q}_2}\mathrm{Re}\left[\delta^L_{\mathbf{q}_1}\delta^L_{\mathbf{k}-\mathbf{q}_1}\delta^L_{-\mathbf{q}_2}\delta^L_{\mathbf{q}_2-\mathbf{k}}\right]\mathbf{q}_1\cdot\mathbf{L}_2(\mathbf{q}_1,\mathbf{k}-\mathbf{q}_1,\mathbf{k})F_{ZA}(\mathbf{q}_2,\mathbf{k}-\mathbf{q}_2)\\ &+\frac{V_f}{4}\int_{\mathbf{q}_1}\int_{\mathbf{q}_2}\mathrm{Re}\left[\delta^L_{\mathbf{q}_1}\delta^L_{\mathbf{k}-\mathbf{q}_1}\delta^L_{-\mathbf{q}_2}\delta^L_{\mathbf{q}_2-\mathbf{k}}\right]\mathbf{q}_2\cdot\mathbf{L}_2(\mathbf{q}_2,\mathbf{k}-\mathbf{q}_2,\mathbf{k})F_{ZA}(\mathbf{q}_1,\mathbf{k}-\mathbf{q}_1)\\ &+\frac{V_f}{4}\int_{\mathbf{q}_1}\int_{\mathbf{q}_2}\mathrm{Re}\left[\delta^L_{\mathbf{q}_1}\delta^L_{\mathbf{k}-\mathbf{q}_1}\delta^L_{-\mathbf{q}_2}\delta^L_{\mathbf{q}_2-\mathbf{k}}\right]\mathbf{q}_1\cdot\mathbf{L}_2(\mathbf{q}_1,\mathbf{k}-\mathbf{q}_1,\mathbf{k})\mathbf{q}_2\cdot\mathbf{L}_2(\mathbf{q}_2,\mathbf{k}-\mathbf{q}_2,\mathbf{k})\end{aligned} \tag{D.4}$$

substituting the definition of the fixed field $\delta(\mathbf{k})$, we can rewrite this as

$$\begin{aligned}P^F_{11}(\mathbf{k}) =& P^L_{\mathbf{k}} + \frac{1}{V_f^{1/2}}\int_{\mathbf{q}_1}\sqrt{P^L_{\mathbf{k}}P^L_{\mathbf{q}_1}P^L_{\mathbf{q}_1-\mathbf{k}}}\cos\left[\theta_{\mathbf{k}}-\theta_{\mathbf{q}_1}-\theta_{\mathbf{q}_1-\mathbf{k}}\right]\mathcal{K}_1(\mathbf{q}_1,\mathbf{k}-\mathbf{q}_1,\mathbf{k})\\ &+\frac{1}{4V_f}\int_{\mathbf{q}_1}\int_{\mathbf{q}_2}\sqrt{P^L_{\mathbf{q}_1}P^L_{\mathbf{k}-\mathbf{q}_1}P^L_{\mathbf{q}_2}P^L_{\mathbf{q}_2-\mathbf{k}}}\cos\left[\theta_{\mathbf{q}_1}+\theta_{\mathbf{k}-\mathbf{q}_1}-\theta_{\mathbf{q}_2}-\theta_{\mathbf{k}-\mathbf{q}_2}\right]\\ &\times\mathcal{K}_1(\mathbf{q}_1,\mathbf{k}-\mathbf{q}_1,\mathbf{k})\mathcal{K}_1(\mathbf{q}_2,\mathbf{k}-\mathbf{q}_2,\mathbf{k}),\end{aligned} \tag{D.5}$$

in which we have defined the following auxiliary kernel, to simplify the notation,

$$\mathcal{K}_1(\mathbf{q}_1,\mathbf{k}-\mathbf{q}_1,\mathbf{k}) = \left[F_{ZA}(\mathbf{q}_1,\mathbf{k}-\mathbf{q}_1)+\mathbf{q}_1\cdot\mathbf{L}_2(\mathbf{q}_1,\mathbf{k}-\mathbf{q}_1,\mathbf{k})\right] \tag{D.6}$$

Before moving to the evaluation of the variance, we make a quick pause to notice that the first term of the expression above, $P^L_{\boldsymbol{k}}$, is the input linear power spectrum, and therefore,

is completely free of any statistical fluctuation; this is already a big difference from a calculation for standard simulations, in which this first term would have a large degree of noise due to the sampling of the amplitudes. Notice as well that the second term contains the cosine of the sum of three phases; therefore, translating all phases by $\pi$, this cosine would become

$$\cos\left[(\theta_{\mathbf{k}}+\pi)-(\theta_{\mathbf{q}_1}+\pi)-(\theta_{\mathbf{k}-\mathbf{q}_1}+\pi)\right]=-\cos\left[\theta_{\mathbf{k}}-\theta_{\mathbf{q}_1}-\theta_{\mathbf{k}-\mathbf{q}_1}\right] \tag{D.7}$$

and when averaging over the two spectra to produce the paired one, this term would cancel, reducing yet another source of noise, and the fixed and paired spectrum is given by

$$\begin{aligned}P_{11}^{F\&P}(\mathbf{k})=&P_{\mathbf{k}}^{L}+\frac{1}{4V_f}\int_{\mathbf{q}_1}\int_{\mathbf{q}_2}\sqrt{P_{\mathbf{q}_1}^{L}P_{\mathbf{k}-\mathbf{q}_1}^{L}P_{\mathbf{q}_2}^{L}P_{\mathbf{q}_2-\mathbf{k}}^{L}}\cos\left[\theta_{\mathbf{q}_1}+\theta_{\mathbf{k}-\mathbf{q}_1}-\theta_{\mathbf{q}_2}-\theta_{\mathbf{k}-\mathbf{q}_2}\right]\\&\times\mathcal{K}_1(\mathbf{q}_1,\mathbf{k}-\mathbf{q}_1,\mathbf{k})\mathcal{K}_1(\mathbf{q}_2,\mathbf{k}-\mathbf{q}_2,\mathbf{k}).\end{aligned} \tag{D.8}$$

With the derivations made above, we are now in position to write an expression for the covariance of the fixed and paired $P_{11}$ spectrum

$$\begin{aligned}\mathrm{Cov}_{11}^{F\&P}(k_i,k_j)=&\frac{1}{16V_f^2V_s(k_i)V_s(k_j)}\int_{\hat{\mathbf{k}}_i}\int_{\hat{\mathbf{k}}'_j}\int_{\mathbf{q}_1}\int_{\mathbf{q}_2}\int_{\mathbf{p}_1}\int_{\mathbf{p}_2}\sqrt{P_{\mathbf{q}_1}^{L}P_{\mathbf{k}-\mathbf{q}_1}^{L}P_{\mathbf{q}_2}^{L}P_{\mathbf{k}-\mathbf{q}_2}^{L}P_{\mathbf{p}_1}^{L}P_{\mathbf{k}'-\mathbf{p}_1}^{L}P_{\mathbf{p}_2}^{L}P_{\mathbf{k}'-\mathbf{p}_2}^{L}}\\&\times\mathcal{K}_1(\mathbf{q}_1,\mathbf{k}-\mathbf{q}_1,\mathbf{k})\mathcal{K}_1(\mathbf{q}_2,\mathbf{k}-\mathbf{q}_2,\mathbf{k})\mathcal{K}_1(\mathbf{p}_1,\mathbf{k}'-\mathbf{p}_1,\mathbf{k}')\mathcal{K}_1(\mathbf{p}_2,\mathbf{k}'-\mathbf{p}_2,\mathbf{k}')\\&\times\Big\langle\cos\left[\theta_{\mathbf{q}_1}+\theta_{\mathbf{k}-\mathbf{q}_1}-\theta_{\mathbf{q}_2}-\theta_{\mathbf{k}-\mathbf{q}_2}\right]\cos\left[\theta_{\mathbf{p}_1}+\theta_{\mathbf{k}'-\mathbf{p}_1}-\theta_{\mathbf{p}_2}-\theta_{\mathbf{k}'-\mathbf{p}_2}\right]\Big\rangle\\&-\Big\langle\cdots\Big\rangle\Big\langle\cdots\Big\rangle.\end{aligned} \tag{D.9}$$

At first, we are interested in the diagonal part of this covariance, and therefore impose $i=j$. Furthermore, we will make the simplifying assumption that we are still in a range of scales at which structures are growing linearly, and different modes are uncorrelated;

this translates into imposing the condition that $\boldsymbol{k} = \boldsymbol{k}'$, resulting in a simpler expression

$$\begin{aligned}\sigma^2_{11}(k_i) =& \frac{1}{16 V_f V_s^2(k_i)} \int_{\hat{\mathbf{k}}_i} \int_{\mathbf{q}_1} \int_{\mathbf{q}_2} \int_{\mathbf{p}_1} \int_{\mathbf{p}_2} \sqrt{P_{\mathbf{q}_1} P_{\mathbf{k}-\mathbf{q}_1} P_{\mathbf{q}_2} P_{\mathbf{k}-\mathbf{q}_2} P_{\mathbf{p}_1} P_{\mathbf{k}-\mathbf{p}_1} P_{\mathbf{p}_2} P_{\mathbf{k}-\mathbf{p}_2}} \\ & \times \mathcal{K}_1(\mathbf{q}_1, \mathbf{k}-\mathbf{q}_1, \mathbf{k}) \mathcal{K}_1(\mathbf{q}_2, \mathbf{k}-\mathbf{q}_2, \mathbf{k}) \mathcal{K}_1(\mathbf{p}_1, \mathbf{k}-\mathbf{p}_1, \mathbf{k}) \mathcal{K}_1(\mathbf{p}_2, \mathbf{k}-\mathbf{p}_2, \mathbf{k}) \\ & \times \Big\langle \cos\left[\theta_{\mathbf{q}_1} + \theta_{\mathbf{k}-\mathbf{q}_1} - \theta_{\mathbf{q}_2} - \theta_{\mathbf{k}-\mathbf{q}_2}\right] \cos\left[\theta_{\mathbf{p}_1} + \theta_{\mathbf{k}-\mathbf{p}_1} - \theta_{\mathbf{p}_2} - \theta_{\mathbf{k}-\mathbf{p}_2}\right] \Big\rangle \\ & - \Big\langle \cdots \Big\rangle \Big\langle \cdots \Big\rangle \end{aligned} \tag{D.10}$$

and we notice that the only piece of this expression which contains random variables is the cosine, and therefore it suffices to compute the variance of this term and plug it into the original expression. The variance of the cosine reads

$$\Big\langle \cos\left[\theta_{\mathbf{q}_1} + \theta_{\mathbf{k}-\mathbf{q}_1} - \theta_{\mathbf{q}_2} - \theta_{\mathbf{k}-\mathbf{q}_2}\right] \cos\left[\theta_{\mathbf{p}_1} + \theta_{\mathbf{k}-\mathbf{p}_1} - \theta_{\mathbf{p}_2} - \theta_{\mathbf{k}-\mathbf{p}_2}\right] \Big\rangle - \Big\langle \cdots \Big\rangle \Big\langle \cdots \Big\rangle. \tag{D.11}$$

We argue that, unless the argument of the multiplied cosines is exactly the same, we can consider them to be independent random variables, and therefore, can split the first part of this expression as the product of the expected values; since the expected value of the cosine of a random variable uniformly distributed between $[0, 2\pi]$ is zero, this does not contribute to the variance. The non-zero contributions will appear when we have one of the following conditions satisfied

$$\begin{cases} \mathbf{q}_1 = \mathbf{p}_1 & \text{and } \mathbf{q}_2 = \mathbf{p}_2, \\ \mathbf{q}_1 = \mathbf{p}_2 & \text{and } \mathbf{q}_2 = \mathbf{p}_1, \\ \mathbf{q}_1 = \mathbf{k} - \mathbf{p}_1 & \text{and } \mathbf{q}_2 = \mathbf{k} - \mathbf{p}_2, \\ \mathbf{q}_1 = \mathbf{k} - \mathbf{p}_2 & \text{and } \mathbf{q}_2 = \mathbf{k} - \mathbf{p}_1, \\ \mathbf{q}_1 = \mathbf{p}_1 & \text{and } \mathbf{q}_2 = \mathbf{k} - \mathbf{p}_2, \\ \mathbf{q}_1 = \mathbf{k} - \mathbf{p}_1 & \text{and } \mathbf{q}_2 = \mathbf{p}_2, \\ \mathbf{q}_1 = \mathbf{p}_2 & \text{and } \mathbf{q}_2 = \mathbf{k} - \mathbf{p}_1, \\ \mathbf{q}_1 = \mathbf{k} - \mathbf{p}_2 & \text{and } \mathbf{q}_2 = \mathbf{p}_1. \end{cases} \tag{D.12}$$

If one of this conditions verifies, arguments of the cosines will be exactly the same, and we have to compute the much simpler term

$$\left\langle \cos^2[\underbrace{\theta_{\mathbf{q}_1} + \theta_{\mathbf{k}-\mathbf{q}_1} - \theta_{\mathbf{q}_2} - \theta_{\mathbf{k}-\mathbf{q}_2}}_{\text{Uniformly distributed between } [0,2\pi]}] \right\rangle = \frac{1}{2}. \tag{D.13}$$

We substitute the variance of the cosine for this value wherever it appears, and enforce one of the conditions listed above by inserting factors such as

$$V_f^2 \delta_D(\mathbf{q}_1 - \mathbf{p}_1)\delta_D(\mathbf{q}_2 - \mathbf{p}_2), \tag{D.14}$$

corresponding to the factor necessary to enforce the first case. The computations then simplifies a lot, resulting in the expression

$$\begin{aligned}\sigma_{11}^2(k_i) =& \frac{V_f}{4V_s^2(k_i)} \int_{\hat{\mathbf{k}}_i} \left[ \int_{\mathbf{q}} P(\mathbf{q}) P(\mathbf{k}-\mathbf{q}) \mathcal{K}_1^2(\mathbf{k},\mathbf{q},\mathbf{k}) \right]^2 \\ =& \frac{1}{4N_{k_i}} \left[ \int \frac{d^3\mathbf{q}}{(2\pi)^3} P(q) P(|\mathbf{k}-\mathbf{q}|) \mathcal{K}_1^2(\mathbf{k},\mathbf{q},\mathbf{k}) \right]_{\Theta_{k_i}}^2 ,\end{aligned} \tag{D.15}$$

in which $N_k = \frac{1}{2}\frac{4\pi k^3 (d\ln k) L^3}{(2\pi)^3}$.

## D.2 $P_{1\delta^2}$

The $\delta_{\delta^2}$ field in Eulerian space is given by

$$\delta_{\delta^2}(\mathbf{k}) = \int_{\mathbf{q}_1} \delta^L_{\mathbf{q}_1} \delta^L_{\mathbf{k}-\mathbf{q}_1} + \int_{\mathbf{q}_1}\int_{\mathbf{q}_2} \frac{\mathbf{k}\cdot(\mathbf{k}-\mathbf{q}_{12})}{|\mathbf{k}-\mathbf{q}_{12}|^2} \delta^L_{\mathbf{q}_1}\delta^L_{\mathbf{q}_2}\delta^L_{\mathbf{k}-\mathbf{q}_{12}} + \mathcal{O}(\delta^4) \tag{D.16}$$

combining this with equation (C.4), we obtain the following expression for $P_{1\delta^2}(\mathbf{k})$

$$\begin{aligned}P^F_{1\delta^2}(\mathbf{k}) =& V_f \int_{\mathbf{q}_1} \mathrm{Re}\left[\delta^L_{\mathbf{k}}\delta^L_{-\mathbf{q}_1}\delta^L_{\mathbf{q}_1-\mathbf{k}}\right] + V_f \int_{\mathbf{q}_1}\int_{\mathbf{q}_2} \frac{\mathbf{k}\cdot(\mathbf{k}-\mathbf{q}_{12})}{|\mathbf{k}-\mathbf{q}_{12}|^2} \mathrm{Re}\left[\delta^L_{\mathbf{k}}\delta^L_{-\mathbf{q}_1}\delta^L_{-\mathbf{q}_2}\delta^L_{\mathbf{q}_{12}-\mathbf{k}}\right] \\ &+ \frac{V_f}{2}\int_{\mathbf{q}_1}\int_{\mathbf{q}_2} \mathcal{K}_1(\mathbf{q}_1, \mathbf{k}-\mathbf{q}_1)\, \mathrm{Re}\left[\delta^L_{\mathbf{q}_1}\delta^L_{\mathbf{k}-\mathbf{q}_1}\delta^L_{-\mathbf{q}_2}\delta^L_{\mathbf{q}_2-\mathbf{k}}\right]\end{aligned} \tag{D.17}$$

Looking at this expression we notice that its leading order term contains an odd number of $\delta^L$, and therefore will be cancelled when applying the pairing procedure to this spectrum, so that the expression for the fixed and paired spectrum will be

$$\begin{aligned} P^{F\&P}_{1\delta^2}(\mathbf{k}) =& V_f \int_{\mathbf{q}_1}\int_{\mathbf{q}_2} \frac{\mathbf{k}\cdot(\mathbf{k}-\mathbf{q}_{12})}{|\mathbf{k}-\mathbf{q}_{12}|^2} \operatorname{Re}\left[\delta^L_{\mathbf{k}}\delta^L_{-\mathbf{q}_1}\delta^L_{-\mathbf{q_2}}\delta^L_{\mathbf{q}_{12}-\mathbf{k}}\right] \\ &+ \frac{V_f}{2}\int_{\mathbf{q}_1}\int_{\mathbf{q}_2} \mathcal{K}_1(\mathbf{q}_1,\mathbf{k}-\mathbf{q}_1) \operatorname{Re}\left[\delta^L_{\mathbf{q}_1}\delta^L_{\mathbf{k}-\mathbf{q}_1}\delta^L_{-\mathbf{q}_2}\delta^L_{\mathbf{q}_2-\mathbf{k}}\right]. \end{aligned} \tag{D.18}$$

Substituting the definition for the fixed field $\delta^L(\mathbf{k})$ one can rewrite the former expression as

$$\begin{aligned} P^{F\&P}_{1\delta^2}(\mathbf{k}) =& \frac{1}{V_f}\int_{\mathbf{q}_1}\int_{\mathbf{q}_2} \frac{\mathbf{k}\cdot(\mathbf{k}-\mathbf{q}_{12})}{|\mathbf{k}-\mathbf{q}_{12}|^2} \sqrt{P^L_{\mathbf{k}}P^L_{-\mathbf{q}_1}P^L_{-\mathbf{q_2}}P^L_{\mathbf{q}_{12}-\mathbf{k}}}\cos\left[\theta_{\mathbf{k}}-\theta_{\mathbf{q}_1}-\theta_{\mathbf{q}_2}-\theta_{\mathbf{k}-\mathbf{q}_{12}}\right] \\ &+ \frac{1}{2V_f}\int_{\mathbf{q}_1}\int_{\mathbf{q}_2} \mathcal{K}_1(\mathbf{q}_1,\mathbf{k}-\mathbf{q}_1) \sqrt{P^L_{\mathbf{q}_1}P^L_{\mathbf{k}-\mathbf{q}_1}P^L_{-\mathbf{q}_2}P^L_{\mathbf{q}_2-\mathbf{k}}}\cos\left[\theta_{\mathbf{q}_1}+\theta_{\mathbf{k}-\mathbf{q}_1}-\theta_{\mathbf{q}_2}-\theta_{\mathbf{k}-\mathbf{q}_2}\right]. \end{aligned} \tag{D.19}$$

Now in possession of this result, we can write an expression for the covariance matrix of this spectrum; to avoid having too large an expression, we will divide this spectrum into two terms, $T_1$ and $T_2$, labeled in the order as they appear in equation (D.19), and will compute their contributions to the covariance matrix separately; the cross-correlations between these terms will not contribute to the diagonal of this matrix, and thus we neglect them.

Beginning with $T_1$, we have the following expression for its covariance

$$\begin{aligned} \mathrm{Cov}^{T_1}_{1\delta^2}(k_i,k_j) =& \frac{1}{16V_f^2V_s(k_i)V_s(k_j)}\int_{\hat{\mathbf{k}}_i}\int_{\hat{\mathbf{k}}'_j}\int_{\mathbf{q}_1}\int_{\mathbf{q}_2}\int_{\mathbf{p}_1}\int_{\mathbf{p}_2} \sqrt{P^L_{\mathbf{k}}P^L_{-\mathbf{q}_1}P^L_{-\mathbf{q}_2}P^L_{\mathbf{q}_{12}-\mathbf{k}}P^L_{\mathbf{k}'}P^L_{-\mathbf{p}_1}P^L_{-\mathbf{p}_2}P^L_{\mathbf{p}_{12}-\mathbf{k}'}} \\ &\times \frac{\mathbf{k}\cdot(\mathbf{k}-\mathbf{q}_{12})}{|\mathbf{k}-\mathbf{q}_{12}|^2}\frac{\mathbf{k}'\cdot(\mathbf{k}'-\mathbf{p}_{12})}{|\mathbf{k}'-\mathbf{p}_{12}|^2} \\ &\times \Big\langle \cos\left[\theta_{\mathbf{k}}-\theta_{\mathbf{q}_1}-\theta_{\mathbf{q}_2}-\theta_{\mathbf{k}-\mathbf{q}_{12}}\right]\cos\left[\theta_{\mathbf{k}'}-\theta_{\mathbf{p}_1}-\theta_{\mathbf{p}_2}-\theta_{\mathbf{k}'-\mathbf{p}_{12}}\right]\Big\rangle \\ &- \Big\langle\cdots\Big\rangle\Big\langle\cdots\Big\rangle, \end{aligned} \tag{D.20}$$

again restricting to the diagonal of this matrix, and making the assumption that we are

still in the linear regime of the growth of structures, we obtain

$$\begin{aligned}\left[\sigma^{T_1}_{1\delta^2}\right]^2(k_i) =& \frac{1}{16V_f V_s^2(k_i)}\int_{\hat{\mathbf{k}}_i}\int_{\mathbf{q}_1}\int_{\mathbf{q}_2}\int_{\mathbf{p}_1}\int_{\mathbf{p}_2}\sqrt{P^L_{\mathbf{k}}P^L_{-\mathbf{q}_1}P^L_{-\mathbf{q}_2}P^L_{\mathbf{q}_{12}-\mathbf{k}}P^L_{\mathbf{k}}P^L_{-\mathbf{p}_1}P^L_{-\mathbf{p}_2}P^L_{\mathbf{p}_{12}-\mathbf{k}}} \\ &\times \frac{\mathbf{k}\cdot(\mathbf{k}-\mathbf{q}_{12})}{|\mathbf{k}-\mathbf{q}_{12}|^2}\frac{\mathbf{k}\cdot(\mathbf{k}-\mathbf{p}_{12})}{|\mathbf{k}-\mathbf{p}_{12}|^2} \\ &\times \Big\langle \cos\left[\theta_{\mathbf{k}}-\theta_{\mathbf{q}_1}-\theta_{\mathbf{q}_2}-\theta_{\mathbf{k}-\mathbf{q}_{12}}\right]\cos\left[\theta_{\mathbf{k}}-\theta_{\mathbf{p}_1}-\theta_{\mathbf{p}_2}-\theta_{\mathbf{k}-\mathbf{p}_{12}}\right]\Big\rangle \\ &- \Big\langle\cdots\Big\rangle\Big\langle\cdots\Big\rangle.\end{aligned} \tag{D.21}$$

We must now compute the variance of the cosine term, in order to plug it back into this expression; once again we use the argument that these cosines will be uncorrelated unless their arguments are precisely the same. Therefore, we will have non-zero contributions only from terms satisfying the following relations

$$\begin{cases} \boldsymbol{q}_1 = \boldsymbol{p}_1, & \boldsymbol{q}_2 = \boldsymbol{p}_2 \\ \boldsymbol{q}_1 = \boldsymbol{p}_2, & \boldsymbol{q}_2 = \boldsymbol{p}_1 \\ \boldsymbol{q}_1 = \boldsymbol{k}-\boldsymbol{p}_{12}, & \boldsymbol{q}_2 = \boldsymbol{p}_1 \\ \boldsymbol{q}_1 = \boldsymbol{k}-\boldsymbol{p}_{12}, & \boldsymbol{q}_2 = \boldsymbol{p}_2 \\ \boldsymbol{q}_1 = \boldsymbol{p}_1, & \boldsymbol{q}_2 = \boldsymbol{k}-\boldsymbol{p}_{12} \\ \boldsymbol{q}_1 = \boldsymbol{p}_2, & \boldsymbol{q}_2 = \boldsymbol{k}-\boldsymbol{p}_{12}, \end{cases} \tag{D.22}$$

and we now have to analyze carefully what will each of these conditions give as contribution to the variance; the first two cases will give a combined contribution of

$$2\times\frac{1}{2}\times P^L_{\boldsymbol{k}}\int_{\mathbf{q}_1}\int_{\mathbf{q}_2}\left(\frac{\boldsymbol{k}\cdot(\boldsymbol{k}-\boldsymbol{q}_{12})}{|\boldsymbol{k}-\boldsymbol{q}_{12}|^2}\right)^2 P^L_{\boldsymbol{q}_1}P^L_{\boldsymbol{q}_2}P^L_{\boldsymbol{k}-\boldsymbol{q}_{12}} \tag{D.23}$$

and the last four will give the following contribution

$$4\times\frac{1}{2}\times P^L_{\boldsymbol{k}}\int_{\mathbf{q}_1}\int_{\mathbf{q}_2}\left(\frac{\boldsymbol{k}\cdot(\boldsymbol{k}-\boldsymbol{q}_{12})}{|\boldsymbol{k}-\boldsymbol{q}_{12}|^2}\frac{\boldsymbol{k}\cdot\boldsymbol{q}_1}{|\boldsymbol{k}-\boldsymbol{q}_1|^2}\right) P^L_{\boldsymbol{q}_1}P^L_{\boldsymbol{q}_2}P^L_{\boldsymbol{k}-\boldsymbol{q}_{12}}. \tag{D.24}$$

Now let us look at the second term in equation (D.19), which we will call $T_2$; once

again, the term which we must first compute is the one involving the cosines, which is given by

$$\Big\langle \cos\left[\theta_{\mathbf{q}_1} + \theta_{\mathbf{k}-\mathbf{q}_1} - \theta_{\mathbf{q}_2} - \theta_{\mathbf{k}-\mathbf{q}_2}\right] \cos\left[\theta_{\mathbf{p}_1} + \theta_{\mathbf{k}-\mathbf{p}_1} - \theta_{\mathbf{p}_2} - \theta_{\mathbf{k}-\mathbf{p}_2}\right] \Big\rangle - \Big\langle \cdots \Big\rangle \Big\langle \cdots \Big\rangle. \tag{D.25}$$

This was precisely the same term which we computed in evaluating the variance of $P_{11}$, and the cases for which we will obtain non-zero contributions are precisely those in equation (D.12). One has to be a bit careful in evaluating what will be these contributions; the first four terms will give us

$$4 \times \frac{1}{2} \times \frac{1}{4} \int_{\mathbf{q}_1} P^L_{\boldsymbol{q}_1} P^L_{\boldsymbol{k}-\boldsymbol{q}_1} \mathcal{K}^2_1(\boldsymbol{q}_1, \boldsymbol{k}-\boldsymbol{q}_1) \int_{\mathbf{q}_2} P^L_{\boldsymbol{q}_2} P^L_{\boldsymbol{k}-\boldsymbol{q}_2}, \tag{D.26}$$

and the last four will give a slightly different contribution

$$4 \times \frac{1}{2} \times \frac{1}{4} \left[ \int_{\mathbf{q}_1} P^L_{\boldsymbol{q}_1} P^L_{\boldsymbol{k}-\boldsymbol{q}_1} \mathcal{K}_1(\boldsymbol{q}_1, \boldsymbol{k}-\boldsymbol{q}_1) \right]^2. \tag{D.27}$$

Collecting all of these terms in a final expression, we have

$$\begin{aligned} \sigma^2_{1\delta^2}(k_i) = & \frac{1}{16 N_{k_i}} \left[ P^L_{\boldsymbol{k}} \int_{\mathbf{q}_1} \int_{\mathbf{q}_2} \left[ \left( \frac{\boldsymbol{k}\cdot(\boldsymbol{k}-\boldsymbol{q}_{12})}{|\boldsymbol{k}-\boldsymbol{q}_{12}|^2} \right)^2 + 2 \left( \frac{\boldsymbol{k}\cdot(\boldsymbol{k}-\boldsymbol{q}_{12})}{|\boldsymbol{k}-\boldsymbol{q}_{12}|^2} \frac{\boldsymbol{k}\cdot\boldsymbol{q}_1}{|\boldsymbol{k}-\boldsymbol{q}_1|^2} \right) \right] P^L_{\boldsymbol{q}_1} P^L_{\boldsymbol{q}_2} P^L_{\boldsymbol{k}-\boldsymbol{q}_{12}} \\ & + \frac{1}{2} \int_{\mathbf{q}_1} P^L_{\boldsymbol{q}_1} P^L_{\boldsymbol{k}-\boldsymbol{q}_1} \mathcal{K}^2_1(\boldsymbol{q}_1, \boldsymbol{k}-\boldsymbol{q}_1) \int_{\mathbf{q}_2} P^L_{\boldsymbol{q}_2} P^L_{\boldsymbol{k}-\boldsymbol{q}_2} + \frac{1}{2} \left[ \int_{\mathbf{q}_1} P^L_{\boldsymbol{q}_1} P^L_{\boldsymbol{k}-\boldsymbol{q}_1} \mathcal{K}_1(\boldsymbol{q}_1, \boldsymbol{k}-\boldsymbol{q}_1) \right]^2 \Bigg]_{\Theta(k_i)}. \end{aligned} \tag{D.28}$$

## D.3 $P_{\delta^2\delta^2}$

From the previous section we have the expression for the $\delta_{\delta^2}$ field in Eulerian space

$$\delta_{\delta^2}(\mathbf{k}) = \int_{\mathbf{q}_1} \delta^L_{\mathbf{q}_1} \delta^L_{\mathbf{k}-\mathbf{q}_1} + \int_{\mathbf{q}_1} \int_{\mathbf{q}_2} \frac{\mathbf{k}\cdot(\mathbf{k}-\mathbf{q}_{12})}{|\mathbf{k}-\mathbf{q}_{12}|^2} \delta^L_{\mathbf{q}_1} \delta^L_{\mathbf{q}_2} \delta^L_{\mathbf{k}-\mathbf{q}_{12}} + \mathcal{O}(\delta^4). \tag{D.29}$$

Combining this to form $P_{\delta^2\delta^2}$, and keeping only terms up to fourth order in $\delta^L$ we write

$$P_{\delta^2\delta^2} = V_f \int_{\mathbf{q}_1} \int_{\mathbf{q}_2} \delta^L_{\mathbf{q}_1} \delta^L_{\mathbf{k}-\mathbf{q}_1} \delta^L_{-\mathbf{q}_2} \delta^L_{\mathbf{q}_2-\mathbf{k}}, \tag{D.30}$$

and substituting the expression for $\delta^L$ in the fixed case we obtain

$$P^{F\&P}_{\delta^2\delta^2} = \frac{1}{V_f}\int_{\mathbf{q}_1}\int_{\mathbf{q}_2}\sqrt{P^L_{\mathbf{q}_1}P^L_{\mathbf{k}-\mathbf{q}_1}P^L_{\mathbf{q}_2}P^L_{\mathbf{k}-\mathbf{q}_2}}\cos\left[\theta_{\mathbf{q}_1}+\theta_{\mathbf{k}-\mathbf{q}_1}-\theta_{\mathbf{q}_2}-\theta_{\mathbf{k}-\mathbf{q}_2}\right]. \tag{D.31}$$

Notice how the cosine term is exactly the same as that of the computation of $P_{11}$, and that pairing does not affect this spectrum at all because the terms which we consider are all even in number of factors of $\delta^L$. One can readily write an expression for the covariance of this spectrum

$$\begin{aligned}\mathrm{Cov}^{F\&P}_{\delta^2\delta^2}(k_i,k_j) =& \frac{1}{V_f^2 V_s(k_i)V_s(k_j)}\int_{\hat{\mathbf{k}}_i}\int_{\hat{\mathbf{k}}'_j}\int_{\mathbf{q}_1}\int_{\mathbf{q}_2}\int_{\mathbf{p}_1}\int_{\mathbf{p}_2}\sqrt{P^L_{\mathbf{q}_1}P^L_{\mathbf{k}-\mathbf{q}_1}P^L_{\mathbf{q}_2}P^L_{\mathbf{k}-\mathbf{q}_2}P^L_{\mathbf{p}_1}P^L_{\mathbf{k}'-\mathbf{p}_1}P^L_{\mathbf{p}_2}P^L_{\mathbf{k}'-\mathbf{p}_2}}\\ &\times\left\langle\cos\left[\theta_{\mathbf{q}_1}+\theta_{\mathbf{k}-\mathbf{q}_1}-\theta_{\mathbf{q}_2}-\theta_{\mathbf{k}-\mathbf{q}_2}\right]\cos\left[\theta_{\mathbf{p}_1}+\theta_{\mathbf{k}'-\mathbf{p}_1}-\theta_{\mathbf{p}_2}-\theta_{\mathbf{k}'-\mathbf{p}_2}\right]\right\rangle\\ &-\left\langle\cdots\right\rangle\left\langle\cdots\right\rangle,\end{aligned} \tag{D.32}$$

and then restricting ourselves to the diagonal of this matrix and to the linear regime of scales, we can write a simpler expression

$$\begin{aligned}\sigma^2_{\delta^2\delta^2}(k_i) =& \frac{1}{V_f V_s^2(k_i)}\int_{\hat{\mathbf{k}}_i}\int_{\mathbf{q}_1}\int_{\mathbf{q}_2}\int_{\mathbf{p}_1}\int_{\mathbf{p}_2}\sqrt{P_{\mathbf{q}_1}P_{\mathbf{k}-\mathbf{q}_1}P_{\mathbf{q}_2}P_{\mathbf{k}-\mathbf{q}_2}P_{\mathbf{p}_1}P_{\mathbf{k}-\mathbf{p}_1}P_{\mathbf{p}_2}P_{\mathbf{k}-\mathbf{p}_2}}\\ &\times\left\langle\cos\left[\theta_{\mathbf{q}_1}+\theta_{\mathbf{k}-\mathbf{q}_1}-\theta_{\mathbf{q}_2}-\theta_{\mathbf{k}-\mathbf{q}_2}\right]\cos\left[\theta_{\mathbf{p}_1}+\theta_{\mathbf{k}-\mathbf{p}_1}-\theta_{\mathbf{p}_2}-\theta_{\mathbf{k}-\mathbf{p}_2}\right]\right\rangle\\ &-\left\langle\cdots\right\rangle\left\langle\cdots\right\rangle,\end{aligned} \tag{D.33}$$

and using the same arguments as those presented in the derivation of $\sigma_{11}$ we can compute the expected value of the product of the cosines, giving the expression

$$\begin{aligned}\sigma^2_{\delta^2\delta^2}(k_i) =& \frac{4V_f}{V_s^2(k_i)}\int_{\hat{\mathbf{k}}_i}\left[\int_{\mathbf{q}}P(\mathbf{q})P(\mathbf{k}-\mathbf{q})\right]^2\\ =& \frac{4}{N_{k_i}}\left[\int\frac{d^3\mathbf{q}}{(2\pi)^3}P(q)P(|\mathbf{k}-\mathbf{q}|)\right]^2_{\Theta_{k_i}},\end{aligned} \tag{D.34}$$